University of Kerbala
College of Science
Chemistry Department

Synthesis and Photodecolarization Activity of Nickel and Zinc Ferrite Nanocompesites and their Blood Hemolysis Test

A Thesis

Submitted to the Council of the College of Science/ University of Kerbala

In a Partial Fulfillment of the Requirements for the Degree of Master of Science in Chemistry

By

Ali Ameer Abed Zied

Supervised by

Prof. Dr. Luma M. Ahmed **Asst. Prof. Dr. Rajaa K. Mohammed**

2023 AD **1444 AH**

بِسْمِ ٱللَّهِ ٱلرَّحْمَٰنِ ٱلرَّحِيمِ

﴿شَهِدَ اللَّهُ أَنَّهُ لَا إِلَٰهَ إِلَّا هُوَ وَالْمَلَائِكَةُ
وَأُولُوا الْعِلْمِ قَائِمًا بِالْقِسْطِ لَا إِلَٰهَ إِلَّا هُوَ
الْعَزِيزُ الْحَكِيمُ﴾

صدق الله العلي العظيم

سورة آل عمران

الآية (١٨)

Supervisor Certification

We certify that this thesis was prepared by **Ali Ameer Abed Ziad** *my supervision at the Chemistry Department, College of Science, University Karbala, as a partial requirement for the degree of Master of Science in Chemistry.*

Signature:

Name: **Dr. Luma M. Ahmed**

Title: Professor

Date: 2/ 3/ 2023

Signature:

Name: **Dr. Rajaa K. Mohammed**

Title: Asst. Professor

Date: 2/ 3/ 2023

In view of the available recommendations by the supervisor, I forward this thesis for debate by the examining committee.

Signature:

Name: **Dr. Luma M. Ahmed**

Title: Professor

Head of Chemistry, college of Science

Date: 2/ 3/ 2023

Examination Committee Certification

We certify that we have read this thesis entitled " **synthesis and photodecolazation activity of Nickel and Zinc Ferrite nanocompesites and their Blood Hemolysis test** " as the examining committee, examined the student " Safaa Ali Khit" on its contents, and that in our opinion, it is adequate for the partial fulfillment of the requirements for the Degree of Master in Science of chemistry.

Signature:
Name: **Dr.Eman Talib Kareem**
Title: Professor
Address: University of Kerbala, College of Science, Department of Chemistry.
Date: 27/2/2023
(Chairman)

Signature
Name: **Dr. Oraas Adnan Hatem**
Title: Professor
Address: University of Al. Qadisyaa , College of Science, Department of Chemistry .
Date: 26 /2/2023
(Member)

Signature:
Name: **Dr. Ahmed AlYasari**
Title: Assistant Professor
Address: University of Kerbala, College of Science, Department of Chemistry
Date: 26 / 2 /2023
(Member)

Signature:
Name: **Dr. Luma M. Ahmed**
Title: Professor
Address: University of Kerbala, College of Science, Department of Chemistry
Date: 26/ 2 /2023
(Member & Supervisor)

Signature:
Name: **Dr. Rajaa K. Mohammad**
Title: Assistant Professor
Address: University of Kerbala, College of Science, Department of Physics
Date: 26/ 2 /2023
(Member & Supervisor)

Approved by the council of the College of Science

Signature :
Name: **Dr. Jasem Hanoon Hashim Al-Awadi**
Title: Assistant Professor
.Address: **Dean of College of Science, University of Kerbala**
Date: 5/3/2023

Dedication

To my father, may Allah have mercy on him.

To my mother, may Allah protect her

To my beloved wife and children

to all friends

To all science students

I dedicate this study

Ali

Acknowledgments

Praise be to **Allah**, Lord of the worlds, and may Allah's blessings be upon **Mohammad** and his pure family, and praise be to Allah for his countless blessings and gifts.
I would like to extend my sincere thanks, gratitude and appreciation to:
My supervisors are ***Prof. Dr. Lama Majeed Ahmed*** *and* ***Assisted Prof. Dr. Raja Khader Mohammad*** for her continuous support, invaluable suggestions and great contributions since the inception of this work.
I also thank all the faculty members of the Chemistry Department of the College of Science at the University of Karbala for their valuable support for the work.
Finally, I thank my **wife**, who was the main supporter in completing my scientific career, as well as everyone who supported me even with a word.

Abstract

This work includes **four** main parts. **The first part** illustrates the preparation of two spinels as photocatalysts: first spinal $NiFe_2O_4$ and second spinal $ZnFe_2O_4$ in presence of the (hexamine) as a capping agent, using the co-precipitation method. This method was supported using the solvothermal method in ethanol at a temperature 180 °C for 90 min. The composite Zn-$NiFe_2O_4$ was prepared by incorporating the first and second spinel using ultrasound techniuqe as a simple and environmentally friendly method.

The second part included the measurement of the properties of all prepared photocatalysts using the (FTIR, XRD, SEM, EDX) techniques.The FTIR spectra showed the octahedral and tetrahedral locations of metals and iron for all the prepared. Based on XRD analysis, the spinel $NiFe_2O_4$, spinel $ZnFe_2O_4$ and Zn-$NiFe_2O_4$ composite are having nano-sizes of 20.13 nm, 16.98 nm, and 28.82 nm, respectively. The SEM analysis gave an idea of the surface shape of the prepared photocatalysts. The shape of the spinel $NiFe_2O_4$ is like broccoli as well as the composite Zn-$NiFe_2O_4$, and the spinel $ZnFe_2O_4$ is like cauliflower, with particle sizes for the first spinel 30.67 nm, the second spinel 27.78 nm and the composite 40.19 nm, and all the studied samples are considered as nanocrystals. Through the EDX spectra demonstrated that the elements Ni, Zn, Fe and O are found in prepared samples. The Tauc equation was used to find all kinds of band gaps for the studied photocatalysts. The band gaps are indirect for all samples, and the values of the energy gaps were 2.05 eV, 2.15 eV and 1.56 eV for the spinel $NiFe_2O_4$, the spinel $ZnFe_2O_4$ and the composite Zn-$NiFe_2O_4$, respectively.

The third part focused on the ability of prepared photocatalysts to remove alkaline blue 4B dye by paying attention to study the effect of various factors on dye removal. These factors include mass of the catalyst, temperature and the initial pH. The results demonstrated that the highest color removal of the dye is

obtained at doses equal to 0.025 g/100mL, 0.025 g/100mL and 0.015 g/100mL using the photocatalysts $NiFe_2O_4$, $ZnFe_2O_4$ and the composite Zn-$NiFe_2O_4$, respectively. The range of temperatures (15, 20, 25 and 35) ^oC were applied, when the effect of high temperature on the efficiency of the chromatic removal of the dye for the first and second spinel and composite, this proves that the reaction is endothermic and not spontaneous. The value of the activation energy of photoreaction using the spinel $NiFe_2O_4$ is less than the activation energy values of using the composite Zn-$NiFe_2O_4$ and the spinel $ZnFe_2O_4$, which are (10.787, 23.696 and 47.689) kJ mol^{-1}, respectively. It was also found that the best pH to removal of the dye for all photocatalytic samples was at 7.

The fourth part, the prepared spinel samples were applied in the hemolysis test by taking 60 samples from healthy and non-smokers donor using different doses of $NiFe_2O_4$, $ZnFe_2O_4$ and Zn-$NiFe_2O_4$ that equal to 0.025 g/mL, 0.025 g/mL and 0.015 g/mL, respectively.

Table of Contents

List of abbreviations and Symbols

Abbreviation and Symbols	The Meaning
AS	The absorbance of the normal saline
AT	The absorbance of the test solution
A 100%	The absorbance of 100% hemolysis
Bg	Band gap
C_o	The initial concentration of the Dye at the dark reaction
C_t	The initial concentration of the Dye after irradiation
CB	Conduction Band
DFT	Density Functional Theory
Ea	Activation Energy
EDX	Energy dispersive X-rays
E_f	Fermi Level
Eg	Energy gap
eV	Electron Volt
FWHM	Full width half –maximum
h^+	Positive Hole
HOMO	Highest Occupied Molecular Orbital
I_o	Light intensity
JCPDS	Joint Contry of Powder Diffraction Standard
k	Wave factor
k_{app}.	Apparent Rate constant
L	Crystallite Size
LUMO	Lowest Occupied Molecular Orbital
PDE	Photo decolourization efficiency
RBCs	Red blood cells
SEM	Scan electron microscopy
T	Temperature
UV-Vis	Ultra violet light in the range from 315 to 830 nm
VB	Valance Band
XRD	X-Ray diffraction
λ	Wavelength
μ_{eff}	Magnetic Moment

CHAPTER ONE

Introduction

Chapter One
Introduction

1.1 General Introduction

Nanotechnology is defined as the understanding and control of matter at dimensions between 1 and 100 nm where unique phenomena enable novel applications [1]. It is one of the most fascinating areas of research because of its presence in every field, such as chemistry, physics, magnetism, electrochemistry, energy, and material science, etc. During the last few decades, most of the research has been concentrated on the design and development of nanomaterials, for their applications in different fields due to their unique physical, chemical, electrical, and magnetic properties [2]. Nano-materials are including nanotubes, quantum dots, nanowires, nanocolloids, nanoparticles, and nanofilms. The bulk materials are particles with a diameter of greater than 100 nm in all directions. As a comparison, one must realize that a single human hair is 60,000 nm thickness and the DNA double helix has a radius of 1 nm (Figure 1-1)[3].

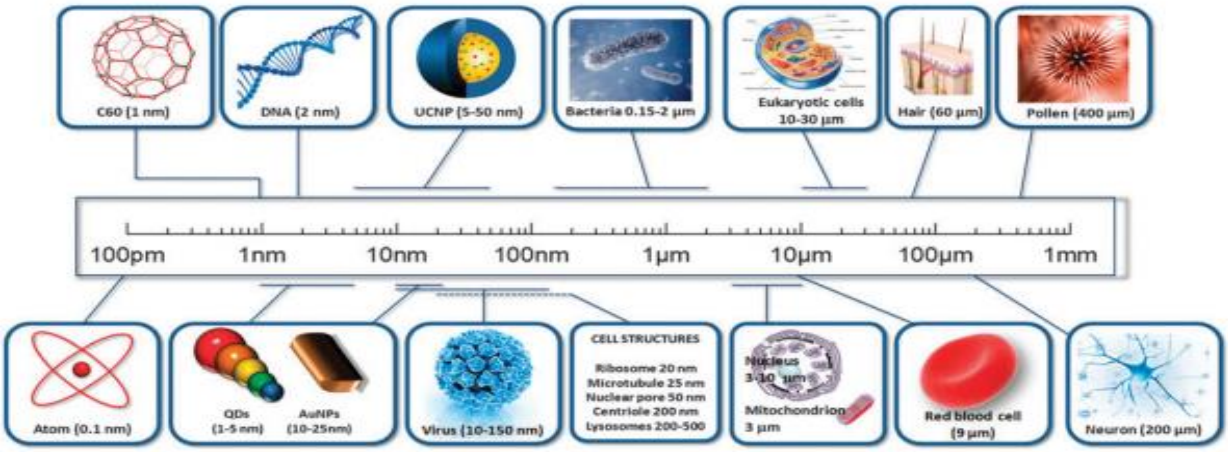

Figure(1-1). A comparison of sizes of nanomaterial and Bulk materials. Reproduced with permission from reference [3].

There is a difference between nanoscience and nanotechnology. Nanoscience is a convergence of physics, materials science and biology, which deal with manipulation of materials at atomic and molecular scales; while nanotechnology is the ability to observe measure, manipulate, assemble, control, and manufacture matter at the nanometer scale.

There are some reports available, which provided the history of nanoscience and nanotechnology, but no report is available which summarize the nanoscience and nanotechnology from the beginning to that era with progressive events. Therefore, it is of the utmost requirements to summarize main events in nanoscience and technology to completely understand their development in this field[4], as illustrated in Figure (1-2).

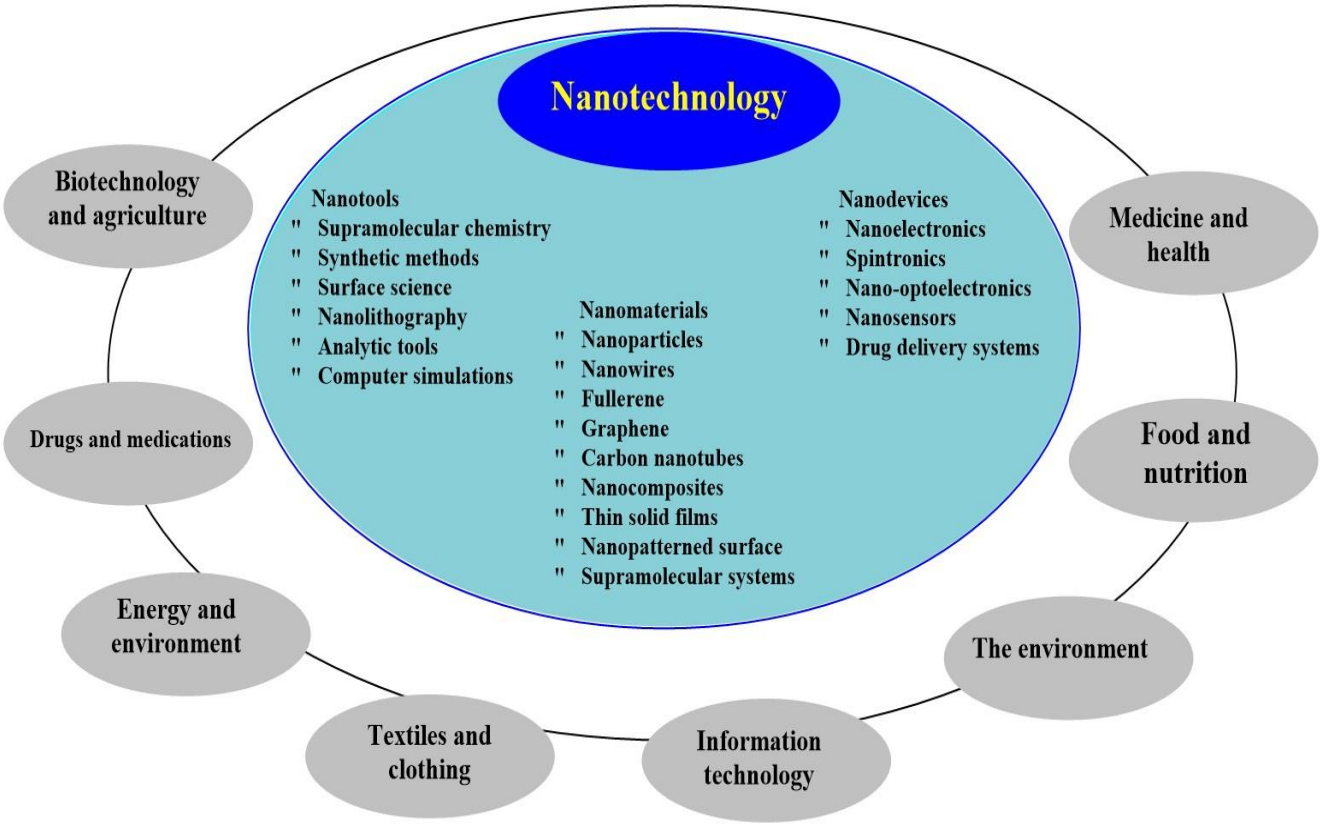

Figure(1-2). Diagram showing nanotechnology and its nanotools, nanomaterials, nanodevices and applications

1.2 Top-down approach and bottom-up approach

The discovery of this new field has attracted the interest of many scientists. They have developed two approaches that describe the different possibilities of nanostructures synthesis. These manufacturing methods fall under two categories: from top to down and from bottom to up, which differ in quality, speed and cost grades as shown in Figure (1-3)[5].

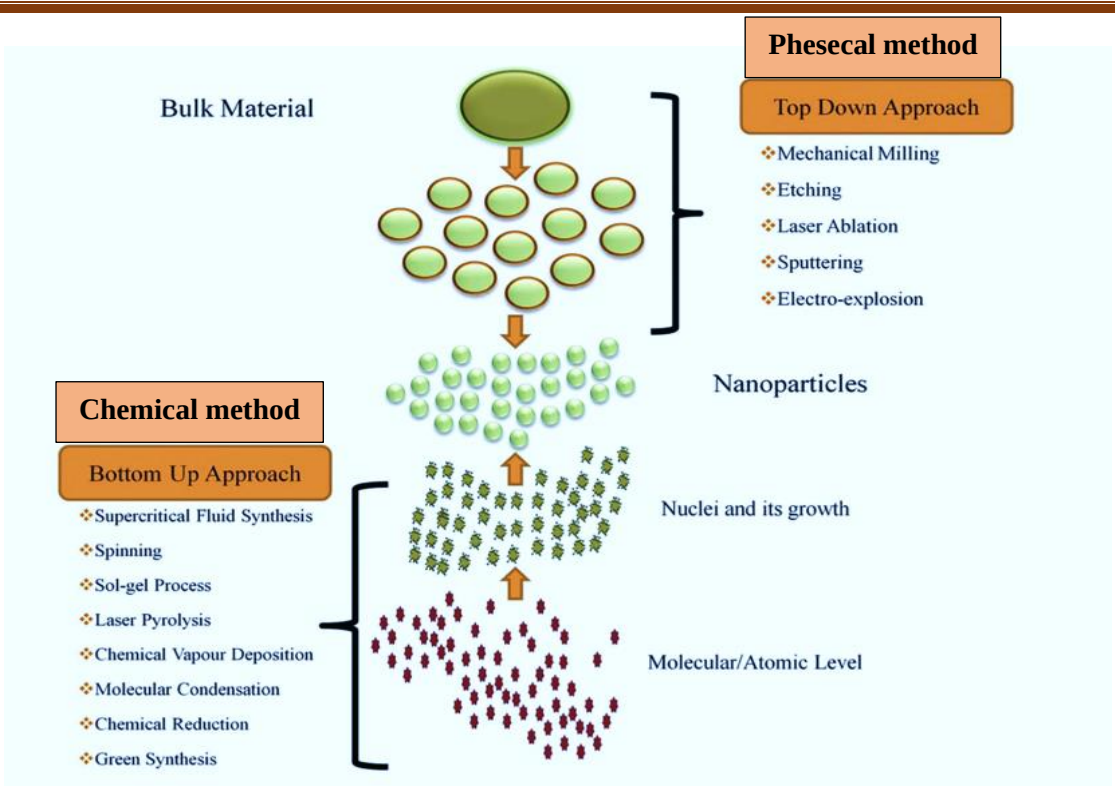

Figure(1-3). The top-down approach and the bottom-up approach [5].

The top-down approach is essentially the breaking down of bulk material to get a nano-sized particles, and can be regarded as a physical method. This can be achieved by using advanced techniques such as precision engineering and lithography which have been developed and optimized by industry during recent decades. Precision engineering supports the majority of the micro-electronics industry during the entire production process, and the high performance can be achieved through the use of a combination of improvements. These include the use of advanced nanostructure based on diamond or cubic boron nitride and sensors for size control, combined with numerical control and advanced servo-drive technologies. Lithography involves the patterning of a surface through exposure to light, ions or electrons, and the deposition of material on to that surface to produce the desired material[6]. Bottom Up approach refers to the build-up of nanostructures from the bottom: atom-by-atom or molecule-by-molecule by physical and chemical methods which are in a nanoscale range (1 nm to 100 nm) using controlled manipulation of self-assembly of atoms and molecules.

Chemical synthesis is a method of producing rough materials which can be used either directly in product in their bulk disordered form, or as the building blocks of more advanced ordered materials. Self-assembly is a bottom-up approach in which atoms or molecules organize themselves into ordered nanostructures by chemical-physical interactions between them. Positional assembly is the only technique in which single atoms, molecules or cluster can be positioned freely one-by-one[7].

1.3 Bulk and Nano material

Bulk materials consist of particles with diameters of greater than 100 nm. Typically, this phrase is used to describe a material that is granular or lumpy and exists in a free-flowing state. Particle size and grain distribution are used to characterize these materials. In addition, the bulk density, moisture content, temperature, etc., may be used to describe their qualities[8]. Nano materials are materials with at least one dimension between 1 and 100 nm. They are also characterized by a single-domain crystalline lattice without the complicating presence of grain boundaries. Interest in nanocrystals has been growing steadily due to their unique position as a bridge between atoms and bulk solids as well as their fascinating properties and potential applications[9]. In table (1-1) and figure (1-4) the comparison of bulk materials and nanomaterial's in terms of style, optical, band gap, the magnetic and mechanistic properties are shown.

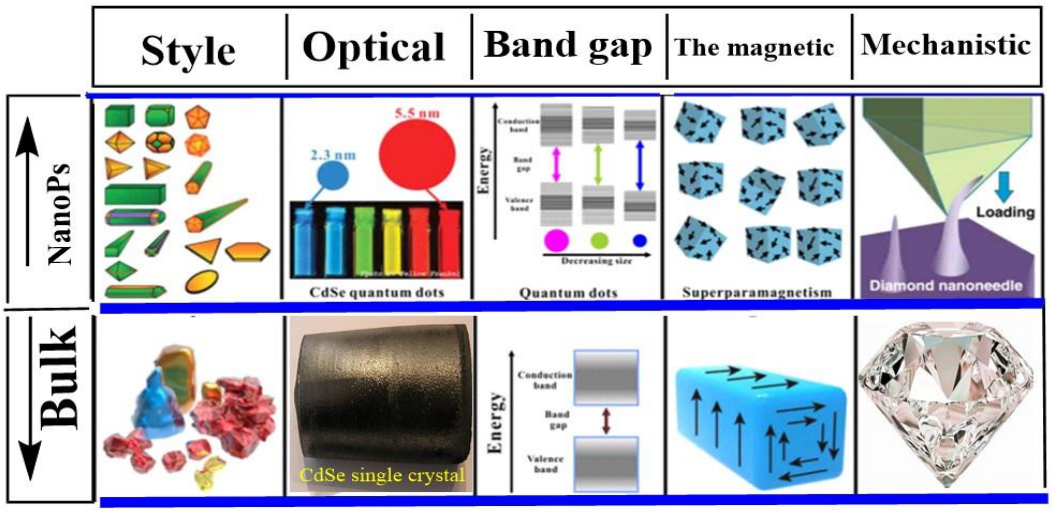

Figure(1-4). The deferent between the bulk and Nano material[17,18]

Table (1-1) different between bulk and Nano material.

	Nanomaterial's	Bulk material's
Style	It have 0D, 1D and 2D this classification includes nanoparticales, (nanotubes ,nanowires) and (thin films, sheets) respectively [10]. 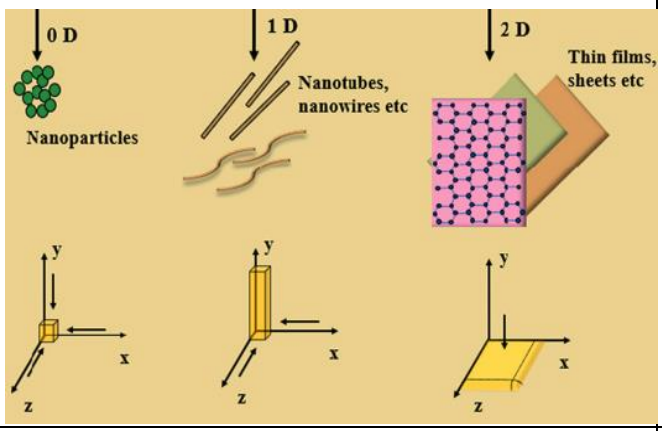	It have 3D Bulk material that are larger than nanoscale (1–100 nm) dimensions are known as 3D [11]. 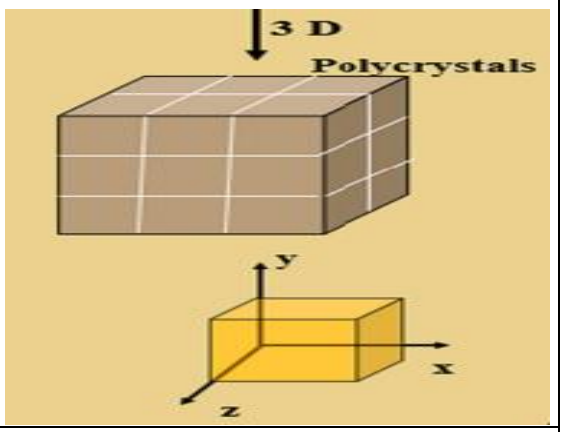
Optical	The luminescence of nanoparticles are well defined with narrow spectral ranges, which depend on particle size. So CdSe Quantum dots has red color at size 5.5 nm but at 2.3 nm it's color was blue[12].	While the optical properties of bulk material's less than nanomaterial's because of the color depends on the size (& shape) of the particle and the dielectric properties of the medium. CdSe single crystal has black color.
Band gap	As particle size approaches the nano scale, where each particle is composed of an extremely small number of atoms or molecules, the number of overlapping orbitals or energy levels drops, and the band width narrows. This will increase the energy gap between the valence and conduction bands[13].	In bulk matter, the bands are actually formed by the merger of lots of adjacent energy levels of a large number of atoms and molecules[14].
Magnetic	Anomalies in the size, shape, and distribution of nanomaterial's relative to their bulk counterparts frequently result in desirable modifications to their physical, chemical, electrical, dielectric, magnetic, and magnetoelectric characteristics[15].	In bulk materials because of Low surface area the magnetic less than Nano.
Mechanistic	Nanomaterial's mechanical strength and modulus rely heavily on their intrinsic mechanical characteristics and are altered by the inner structure, particularly the pattern of interfacial contacts together with the resulting interfacial interactions[15].	In contrast to nanomaterial's, bulk materials are more rigid because of their dense structure. Adding nanomaterials to bulk materials can improve the mechanical properties of nanomaterials[16].

1.4 Semiconductors

Semiconductors are solid-state materials, depending on the band gap value, have an intermediate value between an insulator and a metal (Eg). In metals, the separation between the valence band (VB) and the conducting band (CB) allows electron-charge carriers to pass readily from VB to CB without activation energy, resulting in excellent electric conductivity. In contrast to insulators, the energy gap (Eg) is enormous (Eg > 5 eV), hence electrical conductivity is fully suppressed. Pertaining to semiconductors Eg ranged 1.1-5.0 eV, as shown in Figure (1-5) [27]. External thermal activation energy or light absorption (hv) is necessary for the excitation and transport of electrons from VB to CB [19].

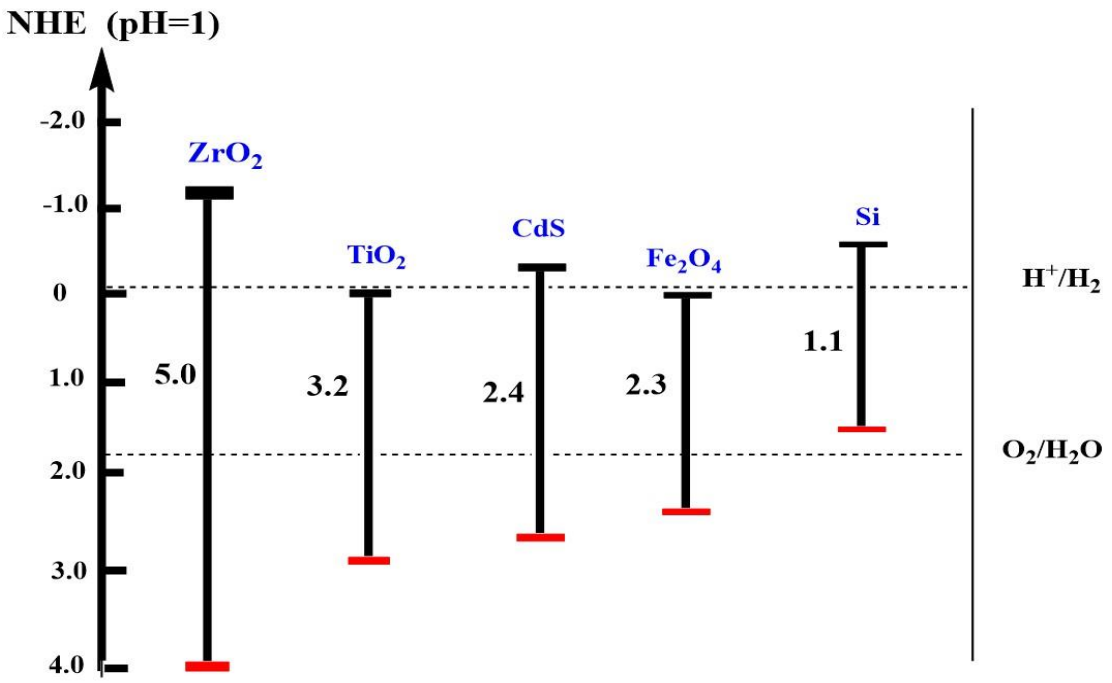

Figure(1-5). The range of band gap of photo semiconductor [27]

1.5 Type of Semiconductors

The semiconductors can be classified as Fermi level and structure of material that manufactured up.

A- As position of Fermi level

According to the position of fermi level, Semiconductors are classified to two type : n-type of semiconductor and p-type of semiconductor as seen in table (1-2).

Table (1-2): Main comparison between p-type and n-type semiconductors [20 ,21]

p-type	n-type
The Fermi level of p-type semiconductor mainly lies among the valence band.	The Fermi level of n-type semiconductors mainly lies among the conduction band.
The conductivity of p-type is because of the presence of majority charge carriers like holes	The conductivity of n-type is because of the presence of majority charge carriers like electrons.
It is called the acceptor of the energy level	It is called the donor of the energy level
When the concentration of holes is high, then this semiconductor carries the +Ve charge	This semiconductor preferably carries a -Ve charge.
Such NiO	Such TiO_2
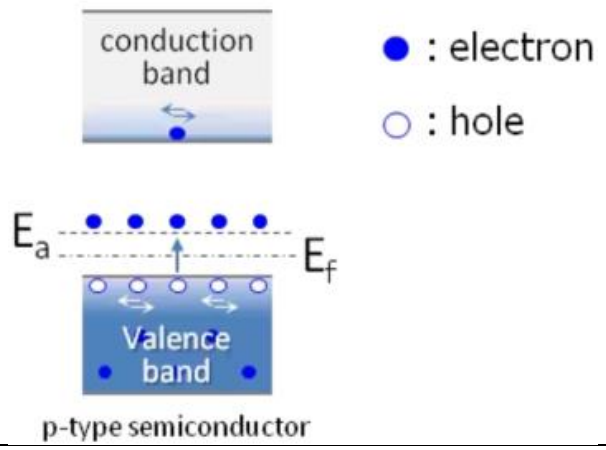	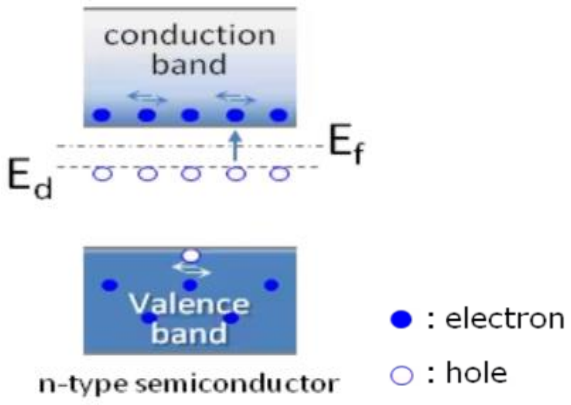

B- Structure of material

Semiconductors can be classified according to their structures [22,23], as shown in the following Figure (1-6).

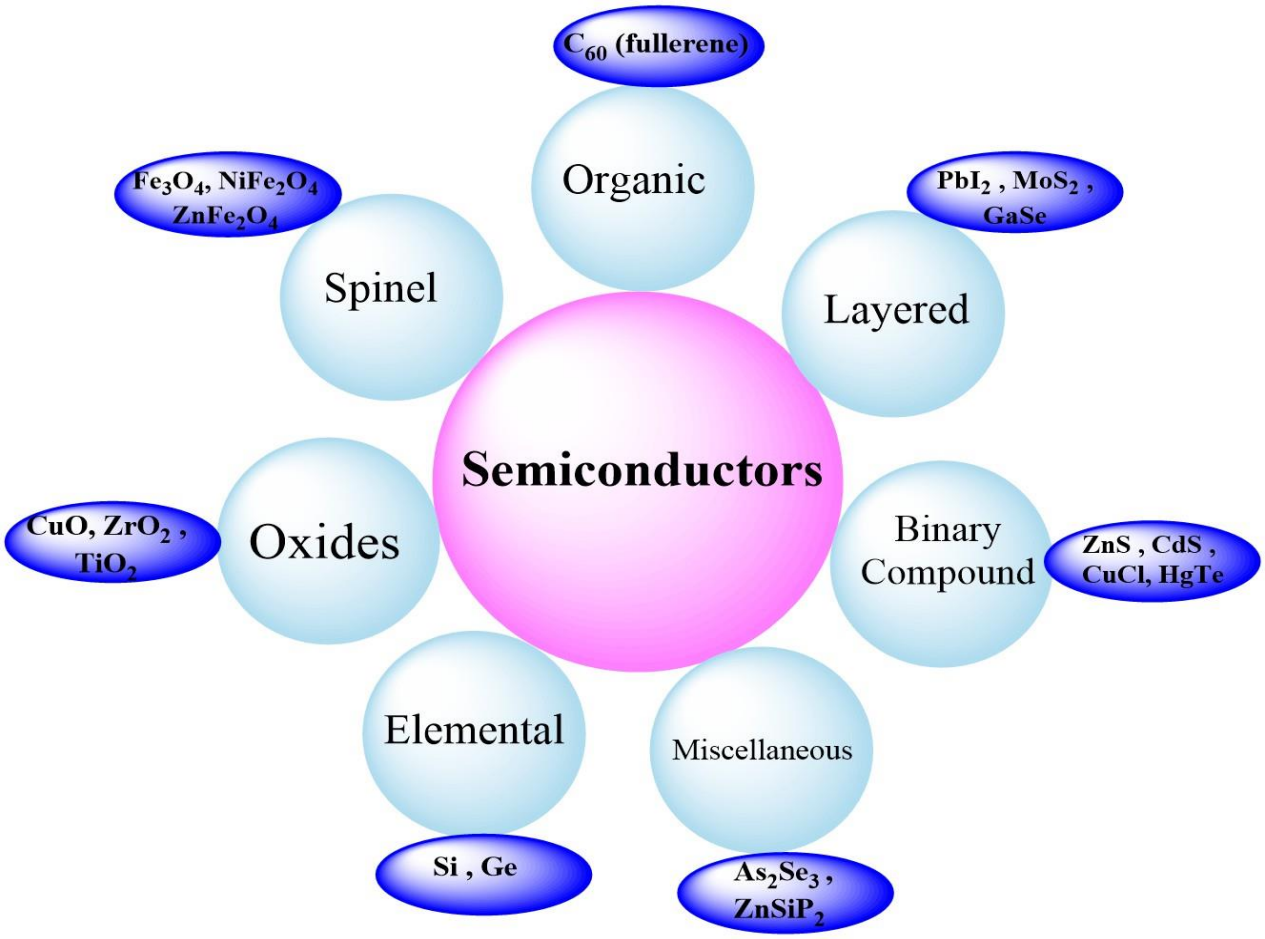

Figure(1-6). The type of semiconductor according to their structure

1.6 Photo semiconductor

Photo Semiconductors are known as the most important photocatalyst materials which possess a valence band (with full electron) and a conduction band (with higher energy and no electron) with definite band gap. The basic mechanism of the photocatalytic process is the absorption of the light photons by semiconductor and formation of electron (e^-) holes (h^+) in the valence band. The electron is excited from the valence band (V_B) to the conduction band (C_B), forming an electron-hole pair (Eq. (1-1). The excited electrons can react with electron acceptors such as O_2 existed on the catalyst surface or dissolved in water and reduce it to form superoxide radical anion $O_2^{\bullet -}$ Eq. (1-2) [24,25]. The holes can scavenge H_2O and OH molecules on the surface of the nanoparticle to generate $\dot{O}H$ radicals Eqs. (1-3) and (1-4). The free hydroxyl radicals are one of the most powerful oxidizing agents with oxidation potential of 2.80 V [26], which are excited and can effectively

mineralize any organic compounds adsorbed onto the particle surface to form water and carbon dioxide Eq. (1-5).

$$\textbf{Semiconductor} + \textbf{hν} \rightarrow e^{-}_{CB} + h^{+}_{VB} \qquad (1-1)$$

$$e^{-}_{CB} + O_2 \rightarrow O^{\cdot -}_2 \qquad (1-2)$$

$$h^{+}_{vB} + OH^{-} \rightarrow OH^{\cdot} \qquad (1-3)$$

$$h^{+}_{vB} + H_2O \rightarrow OH^{\cdot} + H^{+} \qquad (1-4)$$

$$R - H + OH^{\cdot} \rightarrow RCOO^{\cdot} \rightarrow CO_2 + H_2O + inorganicions \qquad (1-5)$$

In actuality, there are two types of band gaps for every photocatalyst: direct and indirect band gaps, which are dependent on the symmetry of the crystal lattice band structure and are shown in table (1-3) [28].

Table 1-3. the different between direct and indirect band gaps

Direct band gaps	Indirect band gaps
From the valence band to the conductance band, the electron is excited perpendicularly.	There is no perpendicular transition of the electron from the valence band to the conductivity band.
The change in wave factor is equal to zero ($\Delta k = 0$).	The change in wave factor is not equal to zero ($\Delta k \neq 0$).
The transitions of an electron are allowed, thereby the energy and electron momentum must be conserved.	The transitions of an electron are forbidden therefore the momentums can't be conserved.
The transition of an electron performs directly via photon.	The transition of an electron performs indirectly via phonon.
Such as ZnS, CdS and ZnO .	Such as TiO_2, GaP
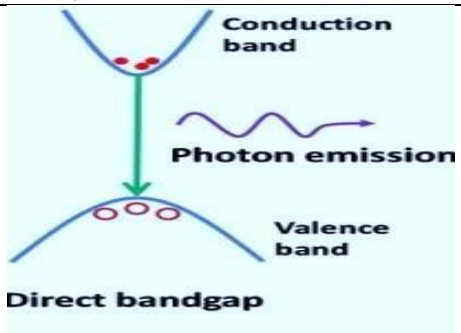	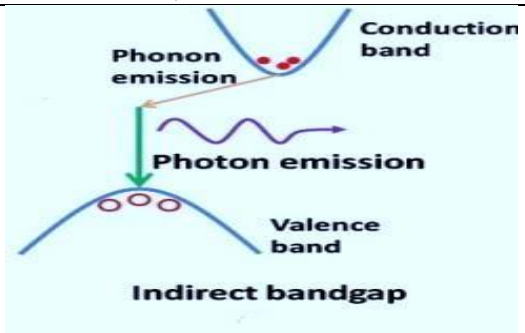

Therefore, direct-gap semiconductors are far more efficient in producing light. Electrons migrate between the smallest conductive band known as the lower occupied molecular orbital (LUMO) and the biggest valence band in most semiconductors, which is known as the high molecular orbital occupied (HOMO)[29].

Recombination, which occurs when electrons return from the conductive band to the valence band and lose energy as heat, might lower the photocatalyst's efficiency.

The common recombination is divided to four kinds [30, 31]

1. **Direct recombination (band-to- band recombination):**

   They become associated when a free photo electron in CB falls directly into an unoccupied state (free photo hole) in the VB. This transition typically occurs as a radiative transition in direct band gap semiconductors and generates a photon.

2. **Volume recombination (centers recombination or Trapassisted recombination):**

   The recombination centers lie at lattice sites of transition within the bulk of the crystal. This type occurs when semiconductor defects caused by impurities create new levels of traps for photoelectrons and photoholes. This case leads to heat being liberated as a phonon in an indirect band gap semiconductor. This process is also called trap-assisted recombination.

3. **Surface recombination (recombination of an exciton):**

   The surface species absorb photogenerated charge carriers (photo electron- hole as exciton). It occurs when traps form at or near the surface or interface of a semiconductor at low temperature as a result of dangling bonds induced by the abrupt cessation of the crystal just below the band gap value. It is used in solar cells and light-emitting diode (LED) devices with a low amount of energy.

4. **Auger recombination :**

   It involves three carriers. When free photo electrons and free photo holes recombine, the third carrier emits energy as heat or as a photon (a non-radiative process). In this process, the transition of energy occurs as intra-band transitions, which result when either an electron elevates into higher levels of the conduction band or a hole deeper pushes into the valence band. Moreover, this process can be obtained in heavy doping defects in direct-gap semiconductors under current

sunlight. Auger recombination has a short lifetime when highly doped materials are used. Figure (1-7) shown the common recombination [30, 31]

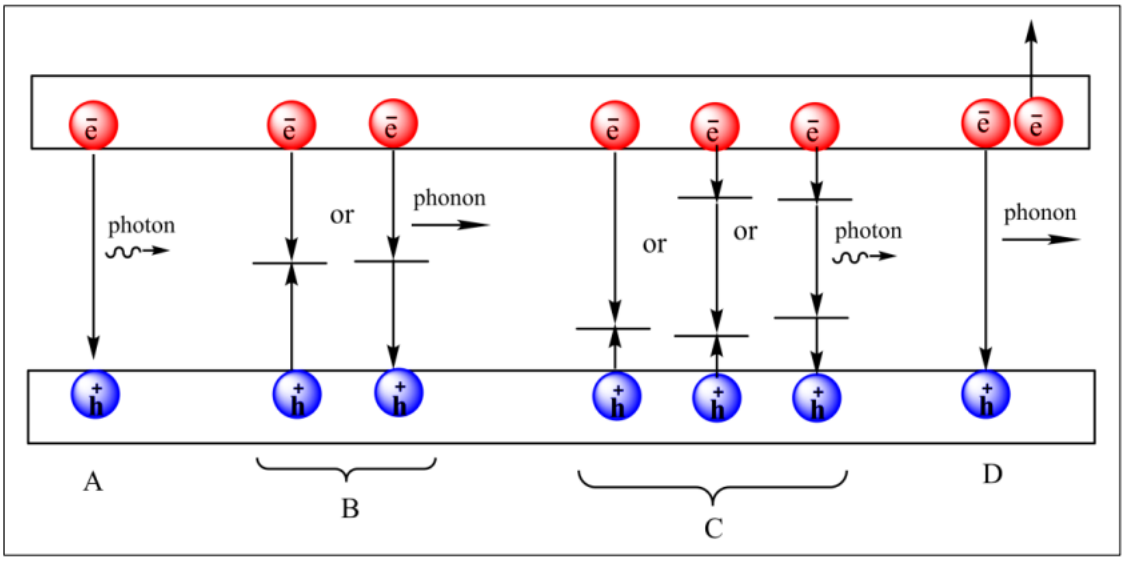

Figure(1-7). The schematic diagram for the common recombination kinds[30, 31]

To recover from the recombination issue, the surface of the photo semiconductor must be modified, as shown in Figure (1-8) [32-36].

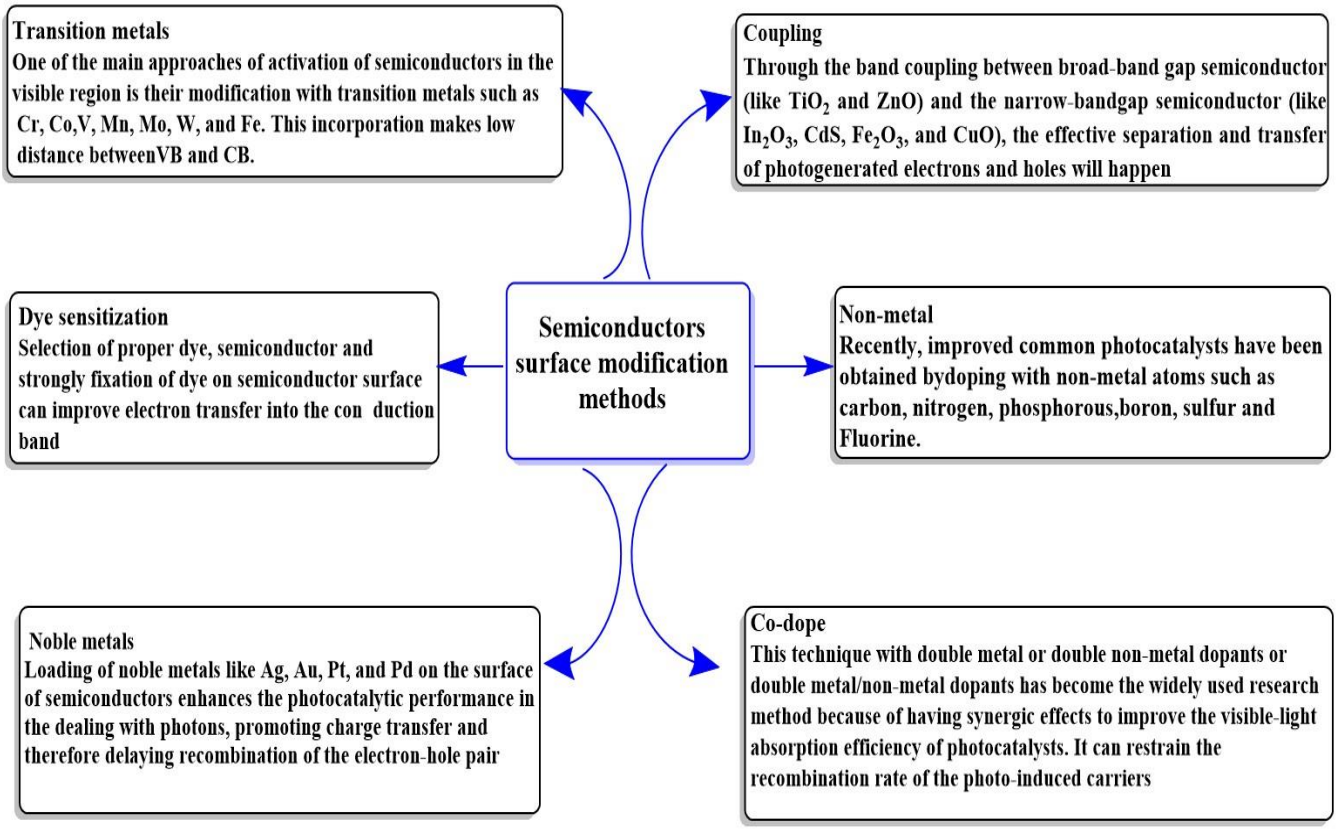

Figure(1-8). Commonly prosses that used to surface modification

1.7 Spinel semiconductor

Spinel is a mixed oxide with the general formula AB_2O_4 which is a chemically and thermally stable material suitable for several applications, including catalysis. The ideal stoichiometric spinel structure is assumed by oxides with an average cation charge of 2.33, for instance, magnetite Fe_3O_4, with one divalent and two trivalent Fe cations. The presence of cations with different charges is at the basis of most catalytic properties of spinels, allowing internal redox reactions that make easier reduction–reoxidation cycles of the catalyst. In the spinel structure,the oxygen anions are distributed in an approximate cubic close-packing and the cations are distributed in the interstices between the oxygen anions. Only a fraction of the interstices are occupied by cations, namely eight tetrahedral interstices (A sites) and 16 octahedral interstices (B sites) in a cell containing 32 oxygen anions, each anion being located at the corner between two octahedra and one tetrahedron. The occupied cation sites form rows of octahedra joined edge-to-edge and connected by tetrahedra[37]. There are two types of spinel, the first is the normal spinel that carries the formula $[A_{Td}^{2+}]\ [B_{Oh}^{3+}]_2[O^{2-}]4$ the tetrahedral sites (Td) are occupied by of the cations A^{2+}, on the other side the B^{3+} are in of the octahedral sites (Oh) like (Mn_3O_4, $ZnFe_2O_4$, $FeCr_2O_4$). In another hand the inverse spinel structure is generated when cations A^{2+} are replaced by half of B^{3+} cations that have been observed experimentally. The general formula of inverse spinel can be written as $[B_{Td}^{3+}]\ [A_{Oh}^{2+}B_{Oh}^{3+}]\ [O^{2-}]_4$ like (Fe_3O_4 , $CoFe_2O_4$, $NiFe_2O_4$)[38].

According of semiconductor type the spinel can be classified into three types

1- **N-type spinel semiconductor**

The charge carrier transport in n-type spinel ferrites is provided by hopping type conductivity of e^- between iron cations located in octahedral sites. A greater Fe^{2+} concentration increases e− conductivity ($Fe^{3+} + e^- \leftrightarrow Fe^{2+}$). After chemisorption of oxygen on the n-type spinel ferrite, Fe^{3+} is redused to Fe^{2+}. When the oxygen react with dye, the e^- is released back to the material and Fe^{3+} is reduced to Fe^{2+}, thus increasing the amount of Fe^{3+} and Fe^{2+}

pairs and overall electrical conductivity. The oxidation–reduction reaction on the surface of n-type spinel ferrite surface is reversible as demonstrated by others. Most popular examples of n-type spinel ferrite are $ZnFe_2O_4$, $CdFe_2O_4$ and $MgFe_2O_4$ [39].

2- p-type spinel semiconductor

P-type spinel ferrites are usually inverse spinel structure ferrites with transition M^{2+} cations in octahedral alongside besides Fe^{3+}. A common p-type spinel ferrite is $NiFe_2O_4$. The p-type conductivity arises from hole (h^+) hopping between Ni^{2+} and Ni^{3+} in octahedral sites ($Ni^{2+} + h^+ \leftrightarrow Ni^{3+}$). The Ni^{3+} in $NiFe_2O_4$ is from the cation vacancy. Cation vacancies in nickel ferrite form due to the tendency of nickel to attract excess oxygen during synthesis. To maintain electrical neutrality in the lattice Ni^{2+} oxidizes to Ni^{+3}[40].

3- Mixed-Type spinel semiconductor

The mixed-type semiconductor generally includes more than two kinds of cations, such as Ni-Zn ferrites (chemical formula: $Ni_{1-x}Zn_xFe_2O_4$) and Co-Ni ferries ($Co_{1-x}Ni_xFe_2O_4$). In the synthesis of nickel-zinc ferrite, zinc ions prefer tetrahedral positions over iron ions, and the Fe^{3+} ions are replaced from tetrahedral to octahedral positions, resulting in a mixed-typed spinel material with divalent and trivalent ions distributed uniformly in the tetrahedron and octahedron positions. The properties of the mixed-type material often depend on the operating temperature. For example, the $Ni_{0.5}Zn_{0.5}Fe_2O_4$ will show the characteristics of the n-type material when the temperature is lower than 225 ^oC, while it will show characteristics of the p-type structure material when it is higher than 225 ^oC[40].

1.8 Dyes

A dye is generally described as substances capable of imparting color through physical/chemical binding on a substrate to which it is applied. The presence of chromophores in dye accounts for the development of color, which auxochromes are attached [41]. These dyes exhibit aromatic molecular structures originating from hydrocarbons, such as benzene, toluene, naphthalene, anthracene, and xylene[42]. Dyes are mainly derived from two significant sources, including natural and anthropogenic. The natural sources include plants, different insects, animals, and minerals, whereas synthetic dyes are man-made or manufactured using various organic molecules[43]. They can be classified considering their chemical structure, physicochemical attributes, origin, and applications. This classification also considers the extremely hazardous/toxic industrial effluents that are carcinogenic to human health and the environment[44]. There are several diverse families of dyes, like: anthraquinone, azo, triphenylmethane, indigo, triarylmethane have recently been studied and proved they are optically nonlinear under continuous and pulsed wave regime.

Triarylmethane is an important kind of synthetic dye and widely used in antimicrobial, antifungal, and antitubercular activities[45]. Triarylmethane dyes are widely utilized in the textile and dying industries due to their vivid color and inexpensive cost. The primary structure of triarylmethane dyes is obtained from the existence of monomethine with three terminal aryl groups as chromophores and functionalization by hydroxyl, amino, or dimethyl amino auxochromic groups[46]. One of type Triarylmethane dye is Akali blue 4B (acid blue 110)[47]. Due to the toxicity and hazard of dyes, there are a variety of ways to eliminate them in wastewater adsorption, photocatalysis, photodegradation, membrane filtration, oxidation, and irradiation [48].

1.9 Application of spinel Nickel and Zinc nano Ferrite in the field of biology and medicine

The current scientific decade is more inclined towards the application of these Nano scaled materials in biomedical and health care sectors. Nano scale is the favorable scale for biomedical applications as most of the biology occurs at this scale. The other key attributes of the Nano-scaled materials are superiority over bulk form, emergence of quantum effects, elevated surface to volume ratio and properties can be tuned effortlessly. Nano-scaled materials with these attributes are primarily implementable in both the 'in-vitro' and 'in-vivo' bio-applications such as biological imaging (as contrast enhancer)[49]. Spinel ferrite nanoparticles (SFNPs) have received a considerable amount of attention due to their wide applications in various fields, which ranges from industrial to biomedical. In biomedical areas, SFNPs are very useful for magnetic resonance imaging (MRI) contrast enhancement, bio-magnetic separation, tumour treatment by hyperthermia, drug delivery and release. They are also valuable for the preparation of modern sensors and biosensors, which are applicable in both industrial and biomedical areas. In addition, spinel ferrite based NPs have strong antimicrobial activity against some pathogenic microorganisms[50]. Researches have shown that the nanoparticles (NPs) ferrites have antibacterial activity against both gram-negative and gram-positive bacteria. Some nanoparticles ferrites was show inhibitory effect on the bacterial growth activity when they are doped with other nano-powders. Some studies even noted that Zn^{2+} and Ni^{2+} cations are non-toxic on human cells and very essential for human health also, they present a good antibacterial truly effects. The antibacterial activities of these cations are highly significant as they stick on to the cell walls of bacteria and result destruction of DNA along with protein inhibition that further leads to cytolysis of bacterial cells. Regarding the

antibacterial activity, earlier studies have established that fairly ultrafine magnetic nanoparticles can easily penetrate intracellular into the bacterial cell, interact with cell membrane, produce oxidative stress and result in destruction of DNA[51]

1.10 Hemolysis assay

Hemolysis is damage, either short-term or long-term, that causes hemoglobin to leak out of red cells. Blood-contacting devices are susceptible to damage from mechanical, thermal, chemical, and biological causes. Mechanical damage may be further classified based on surface contacts, such as cells crushed between the walls of a roller pump or the mass of wood. While each of these damage factors may be significant for certain patients and applications, foam-induced hemolysis has been shown to be a persistent problem across a broad spectrum of medical devices. Red blood cells (RBCs) traversing the circulatory system and prosthetic devices are subjected to a variety of stresses throughout a range of exposure durations. Under typical circumstances in the natural circulation, these stressors are, for the most part, below the hemolytic damage threshold for RBCs[52]. The membrane mechanical stability of red blood cells (RBCs) is a good indicator for estimating *in vitro* cytotoxicity as cells with cytotoxic compounds. Lyses can have a variety of health consequences and cause a variety of disorders. Hemolysis has been observed in transferable diseases as a result of microbe action. Phenolic compounds, flavonols, and glycosides have numerous biological activities that may be important in antioxidant and cytotoxic activity [53]. It is important to study the actual interaction of intravenously injected nanoparticles and blood. Such interactions may prove pivotal in improving the transport and targeting ability of the nanoparticles besides reducing the biotoxicity. Nanoparticles when entered into the body, formation of protein corona takes place due to the adsorption of blood protein on the surface of nanoparticles. This results into the change in size and surface charge of the

nanoparticles causing the unexpected alteration in cellular interaction, biodistribution, and cellular uptake. Also, intravenous administration of the nanoparticles can results into producing high local concentration in the circulating blood, which makes it mandatory to evaluate its biological safety. Several hemolytic studies were carried out on the impact of nanoparticles (silica nanoparticles, carbon nanotubes, silver nanoparticles, iron oxide and Au nanoparticles) on erythrocytes in the blood. It is also known that hemolytic activity differs for bare and coated nanoparticles as its interaction depends on surface, size or nature of the particles too[54]. Nanoparticles can affect human erythrocytes in different ways. The most common are hemolysis (rupture of the erythrocyte membrane) and/or induction of free radicals. They can also lead to eryptosis or erythrocyte apoptosis. Other side effects affecting human and animal erythrocytes include morphological changes, induction of oxidative stress, and alteration of enzymatic activities[55]. The toxicity of different nanoparticles in RBCs has been recently evaluated. Iron oxide nanoparticles do not produce hemolysis neither in Albino rats nor in humans. However, some studies have shown that IONPs (iron oxide nanoparticles) produce lipid peroxidation and a decrease in hemoglobin, glutathione, catalase and superoxide dismutase in Wistar rats erythrocytes. IONPs may produce eryptosis, oxidative stress and hemolysis in human erythrocytes. In a similar way, it has been shown that nickel-zinc ferrite decrease the amount of erythrocytes in rats[56,57]. There are several characteristics of nanomaterials affecting their toxicity which are sometimes dose independent. It is well known that size has a strong effect on cells, both in vitro and in vivo. In general, the smaller nanoparticles are the most toxic because they are more likely to be internalized within the cells [58]. Other properties that affect nanoparticles' toxicity and tissue impairment are their structure, solubility, shape, charge, density, surface area, high reactivity, and the agglomerative tendency of nanoparticles in the medium [59]. Other features, such as changes in the metal composition of multimetal iron oxide NPs, also

affect their toxicity. In this work, we evaluated the toxicity of three different ferrite NPs, which vary in their metal composition, both in RBCs and PBMCs. Cells were treated with different concentrations of nickel ferrite, zinc ferrite, and nickelzinc ferrite NPs by hemolysis tests[60].

1.11 Literature review

There are many literature reviews for the Synthesis of Spinel $ZnFe_2O_4$, $NiFe_2O_4$ and Zn-$NiFe_2O_4$ nanocomposite. In 2018 Patil S.B and co-workers [61] synthesized the Zinc Ferrite NPs by combustion method (sugar cane juice as a fuel), with crystallite sizes 84.18 nm at below 600 ^oC. The photocatalytic activity was carried out by the degradation of mixed organic dyes (Methylene Blue and Rose bengal). Later in next year M. Madhukara Naik and co-workers [62] reported the Zinc Ferrite ($ZnFe_2O_4$) nanoparticles were prepared by a green method using Limonia acidissima with spherical shaped particles and the average crystallite size is 20 nm.This prepared nanoparticle uses as antibacterial active by agar well diffusion method against both gram-positive and gram-negative bacterial strains and showed effective photodegradation for Evans blue and Methylene blue under visible light irradiation. In same year Qiushan Yu and co-workers [63] synthesized nickel-zinc ferrite using co-precipitation method and the powder treatment at range of temperature equal to 500-800 ^oC. The average crystal grain size in the samples ranged from 10.6 nm to 58.6 nm. As the temperature rose during treatment, the crystal increased progressively. Treatment must be conducted at a lower temperature to get a smaller crystal grain size. In this research, a study was conducted Magnetic analysis and Analysis of microwave absorbing properties. After that in 2020 Mohammad Bagher Askari and co-workers [64] synthesized nickel ferrite nanoparticles ($NiFe_2O_4$) and hybrid of $NiFe_2O_4$/rGO using hydrothermal method. The average crystalline diameter for $NiFe_2O_4$ was 20nm. The synthesized compound $NiFe_2O_4$/rGO electrode presents a higher rate capability and cycling stability than $NiFe_2O_4$ in this work. Wihle in this year Farzana Majid and co-workers [65] illustrated the synthesis of $NiFe_2O_4$ using hydrothermal and sol–gel routes. The average crystalline size was 29.39 nm for hydrothermal method, whereas using solgel route furnished 52.16 nm crystalline size.

They studied the magnetic and insulating properties of the backbone by the synthesis method separately, and they found that the properties depend on the method of synthesis. Recently Samson O. Aisida and co-workers [66] used sol gel approach and A biogenic protocol to prepare the Zinc Ferrite ($ZnFe_2O_4$) nanoparticles using an aqueous extract without and with Allium cepa (AC) as a reducing agent. The average crystallite size for Zinc Ferrite was 33.4 nm and for Zinc Ferrite with (A C) was 40.6 – 54.4. This study is a new attempt to improve the magnetic and photocatalytic properties. After that Waheed Ali Khoso and co-workers [67] used co-precipitation method for preparing the nickel ferrite nanoparticle . The average crystalline diameter for $NiFe_2O_4$ was found to be 30.25 nm, in this study Nickel Ferrite using to removal heavy metal, such as Cr(VI), Pb(II) and Cd(II), from aqueous solutions. Later Atiya Rabbani and co-workers [68] synthesized and a modified the nickel ferrite and zinc/nickel ferrite NPs using co-precipitation method. The average particles size of nickel ferrite and zinc/nickel ferrite were 25 and 54 nm, respectively. The prepared NPs were compatible with human dermal and blood cells, which suggested that these can be potential candidates for biomedical applications nickel ferrite and zinc/nickel ferrite NPs can act as potent antimicrobial nano-drugs against infectious organisms and may also be used in wound healing formulations. More recente V. Yu. Buz'ko and co-workers [69], prepared the zinc/nickel ferrite NPs by a pyrochemical nitrate–urea process and a sol–gel nitrate–citrate process that have been shown to differ in microstructural, electronic, and electromagnetic characteristics. The average particles size was 33nm for using pyrochemical nitrate–urea process, and with an average nanoparticle size of 46 nm, which prepared by the sol–gel process. This work shows that the properties of the material prepared by a pyrochemical nitrate–urea method have better properties and properties than the method the sol–gel.

1.12 The Aim of the Study

This work aimes to:

1- Prepare spinel **Nickel** ferrite nanostructure.

2- Prepare spinel **Zinc** ferrite nanostructure.

3- Prepare spinel **Nickel** ferrite- spinel **Zinc** ferrite as a Nanocomposite.

4- Study the properties of the as-prepared nanostructure using spectral identification by (Infrared spectroscopy (FT-IR), X-ray diffraction (XRD), scan electronic Microscope (SEM), Energy Dispersive X-Rays (EDX), magnetic sensitivity and band gap (Bg)).

5- Study the photoactivity for the prepared nanocatalysts.

6- Study the blood hemolysis test for using the prepared nanostructures.

CHAPTER TWO

Experimental

Chapter Two

Experimental

2.1 Chemicals

In this job work, the chemicals used as tabulated in Table (2-1), were used without purification.

Table (2-1): Used chemicals

No.	Chemicals	Company supplied	Purities and percentage %
1.	1,10- Phenanthroline ($C_{12}H_8N_2$)	Riedel-De-Haen AG, Seelze, Hannover, Germany.	(99.98) %
2.	Absolute ethanol (C_2H_5OH)	Carlo erba, France..	(99.9) %
3.	Alkali blue 4B	Merck, Switzerland	99%
4.	Ammonia solution (NH_4OH)	CDH, India	99%
5.	Ferric nitrate $Fe(NO_3)_3.9H_2O$	Sigma cheml co. USA.	99%
6.	Hexamethylenetetramine $C_6H_{12}N_4$	Interchimiques SA	99%
7.	Iron (III)sulfate hydrate ($Fe_2(SO_4)_3.H_2O$)	Evans, Mf-Dica, England.	(99.98) %
8.	Nickel nitrate $Ni(NO_3)_{2.}9H_2O$	Sigma cheml co. USA.	99%
9.	Normal saline N.S.	Pioneer , Iraq	99%
10.	Potassium oxalate ($K_2C_2O_4.H_2O$)	Riedel-De-Haen AG, Seelze, Hannover, Germany	(99.98) %
11.	Sulphuric acid (H_2SO_4)	CDH, India	(97.98) %
12.	Triton X -100	Himedia, USA	99%
13.	Zinc nitrate $Zn(NO_3)_2.9H_2O$	Sigma cheml co. USA.	99%

2.2 Instruments

Table (2-2) describes the employed instruments in this study with their companies and places.

Table (2-2): Employed instruments.

No.	Instruments	Companies	Location
1.	UV. Vis. spectroscopy	FAITHFUL-721 China.	University of Kerbala, Science college
2.	Centrifuge	Hettich- Universal IIGermany	University of Kerbala, Science college
3.	Digital pH meter	OAICTON-2100, Singapore	University of Kerbala, Science college
4.	FT-IR Spectrometers	Shimadzu,8400S Japan	University of Kerbala, Science college
5.	High-Pressure Mercury Lamp -UV (A) (400W).	Rudium, China.	University of Kerbala, Science college
6.	Hotplate Magnetic Stirrer	Heido-MrHei-Standard, Germany	University of Kerbala, Science college
7.	Magnetic Measurements	Magnetic susceptibility Balance	Department of Chemistry - College of Science - AlNahrain University
8.	Oven	Memmert, Germany.	University of Kerbala, Science college
9.	Scanning Electron Microscopy (SEM) (EDAX)	(kyky EM) 320., USA.	Isfahan University, Iranian Islamic Republic
10.	Ultrasonic bath high-frequency ≥ 100kHz	DAIHAN Scientific, Korea.	University of Kerbala, Science college
11.	Ultrasonic bath low-frequency = 46 kHz	EASY HOME, turkey	University of Kerbala, Science college
12.	X-Ray Diffraction Spectroscopy	Lab X- XRD 6000, Shimadzu, Japan	Isfahan University, Iranian Islamic Republic

2.3 Preparation of semiconductor

2.3.1 Preparation of Nickel Ferrite semiconductor

1. Solution 1: 0.2 M of Ferric nitrate $Fe(NO_3)_3.9H_2O$ solution was prepared from dissolved 4.04 g in 50 mL D.W under ultrasonic waves(46 kHz) for 10 min.
2. Solution 2: 0.1 M of Nickel nitrate $Ni(NO_3)_3.6H_2O$ solution was prepared from dissolved 1.45 g in 50 mL D.W under ultrasonic waves low-frequency(46 kHz) for 10 min.
3. In ultrasonic bath, solution 2 was added step by step to solution 1 and mixed for 10min.
4. The pH of solution was about 3, after that, 0.5 g of non-ionic surfactant (Hexamethylenetetramine) was added as capping agent with continuous mixed using a magnetic stirrer at 60 ^{o}C for 10 min.
5. The (5 mL) of conc. ammonia solution was drop-wise added to the last solution until the pH was reached between 9.5 to 10 under Heating and stirring continued for 30 min.
6. The dark brown solution was produced; this solution was filtered and washed with D.W.
7. The brown precipitate was dispersived in 50 mL from Ethanol, then transported to Teflon cup with sealed in an autoclave of hydrothermal instrument and heated in oven at 180 ^{o}C for 90 min.
8. After cooling the steles steal autoclave in air, the solution was filtered and washed by 50mL D.W, then 30 mL of ethanol (to ensure all surfactant is removed, and removed all humidity.

$$Ni(NO_3)_2.\ 6H2O + 2Fe\ (NO_3)_3.\ 9H_2O + 8NH_4OH \rightarrow Ni(OH)_2.\ Fe_2(OH)_6 + 8NH_4NO_3 + 24H_2O \quad \ldots(2\text{-}1)$$

$$Ni(OH)_2.\ Fe_2(OH)_6 \rightarrow NiO.\ Fe_2O_3 + 4H_2O \quad \ldots(2\text{-}2)$$

All of steps for preparation Nickel Ferrite shown in figure (2-1).

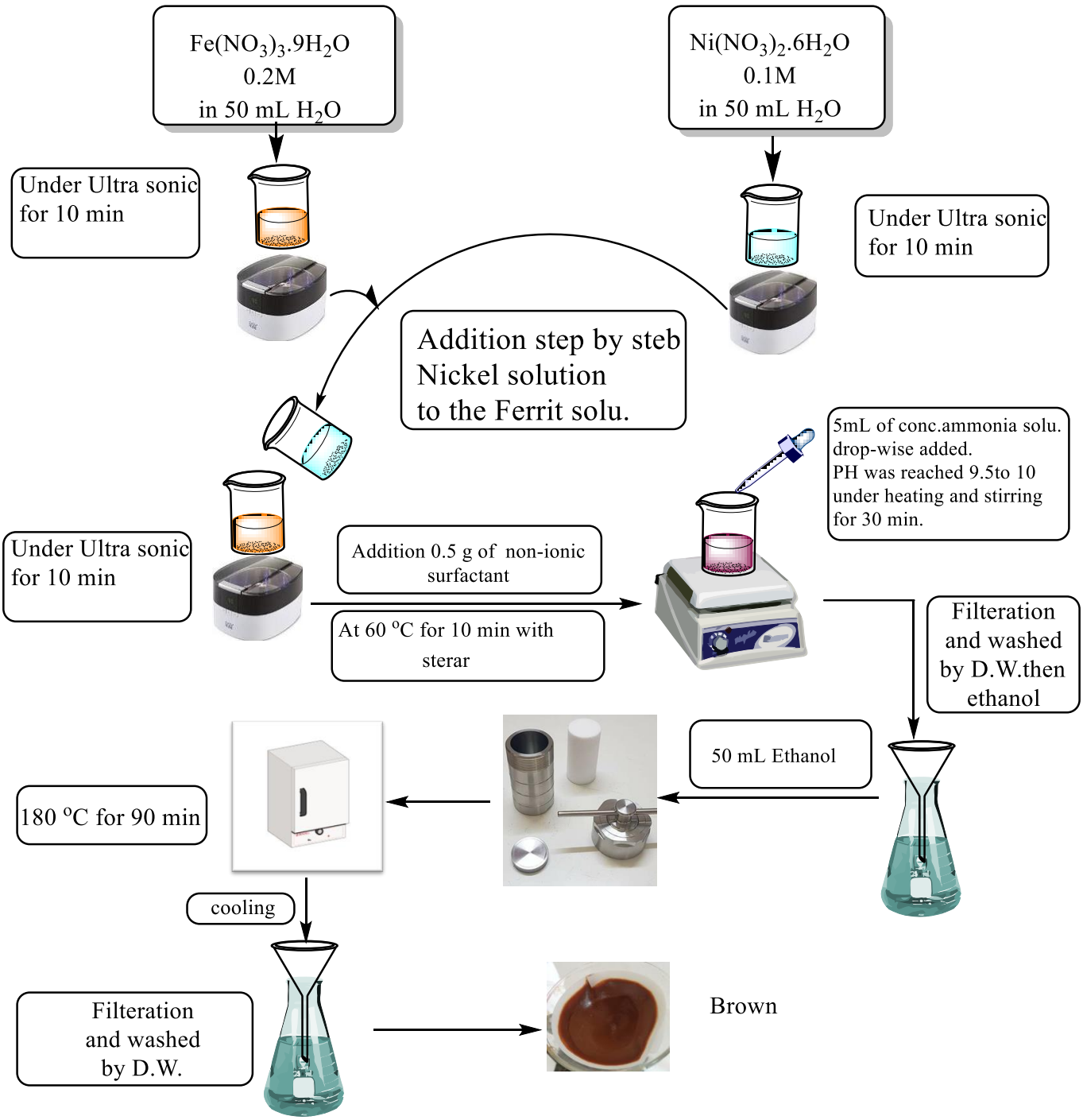

Figure (2-1). The schematic diagram of the steps of Nickel Ferrite nanoparticle preparation

2.3.2 Preparation of Zinc Ferrite semiconductor

1. Solution 1: 0.2 M of Ferric nitrate $Fe(NO_3)_3.9H_2O$ solution was prepared from dissolved 4.04 g in 50 mL D.W under ultrasonic waves for 10 min.
2. Solution 2: 0.1 M of Zinc nitrate $Zn(NO_3)_3.6H_2O$ solution was prepared from dissolved 1.45 g in 50 mL D.W under ultrasonic waves low-frequency(46 kHz) for 10 min.
3. In ultrasonic bath, solution 2 was added step by step to solution 1 and mixed for 10min.
4. The pH of solution was about 3, after that, 0.5 g of non-ionic surfactant (Hexamethylenetetramine) was added as capping agent with continuous mixed using a magnetic stirrer at 60 ^oC for 10 min.
5. The (5 mL) of conc. ammonia solution was drop-wise added to the last solution until the pH was reached between 9.5 to 10 under Heating and stirring continued for 30 min.
6. The dark brown solution was produced; this solution was filtered and washed with D.W.
7. The brown precipitate was dispersive in 50 mL from Ethanol, then transported to Teflon cup with sealed in an autoclave of hydrothermal instrument and heated in oven at 180 ^oC for 90 min.
8. After cooling the steles steal autoclave in air, the solution was filtered and washed by 50mL D.W, then 30 mL of ethanol (to ensure all surfactant is removed, and removed all humidity.

$$\mathbf{Zn(NO_3)_2.\ 6H_2O + 2Fe(NO_3)_3.\ 9H_2O + 8NH_4OH \rightarrow Zn(OH)_2.\ Fe_2(OH)_6 + 8NH_4NO_3 + 24H_2O} \quad \ldots(2\text{-}3)$$

$$\mathbf{Zn(OH)_2.Fe_2(OH)_6 \rightarrow ZnOFe_2O_3 + 4H_2O} \quad \ldots(2\text{-}4)$$

All of steps for preparation Nickel Ferrite shown in figure (2-2).

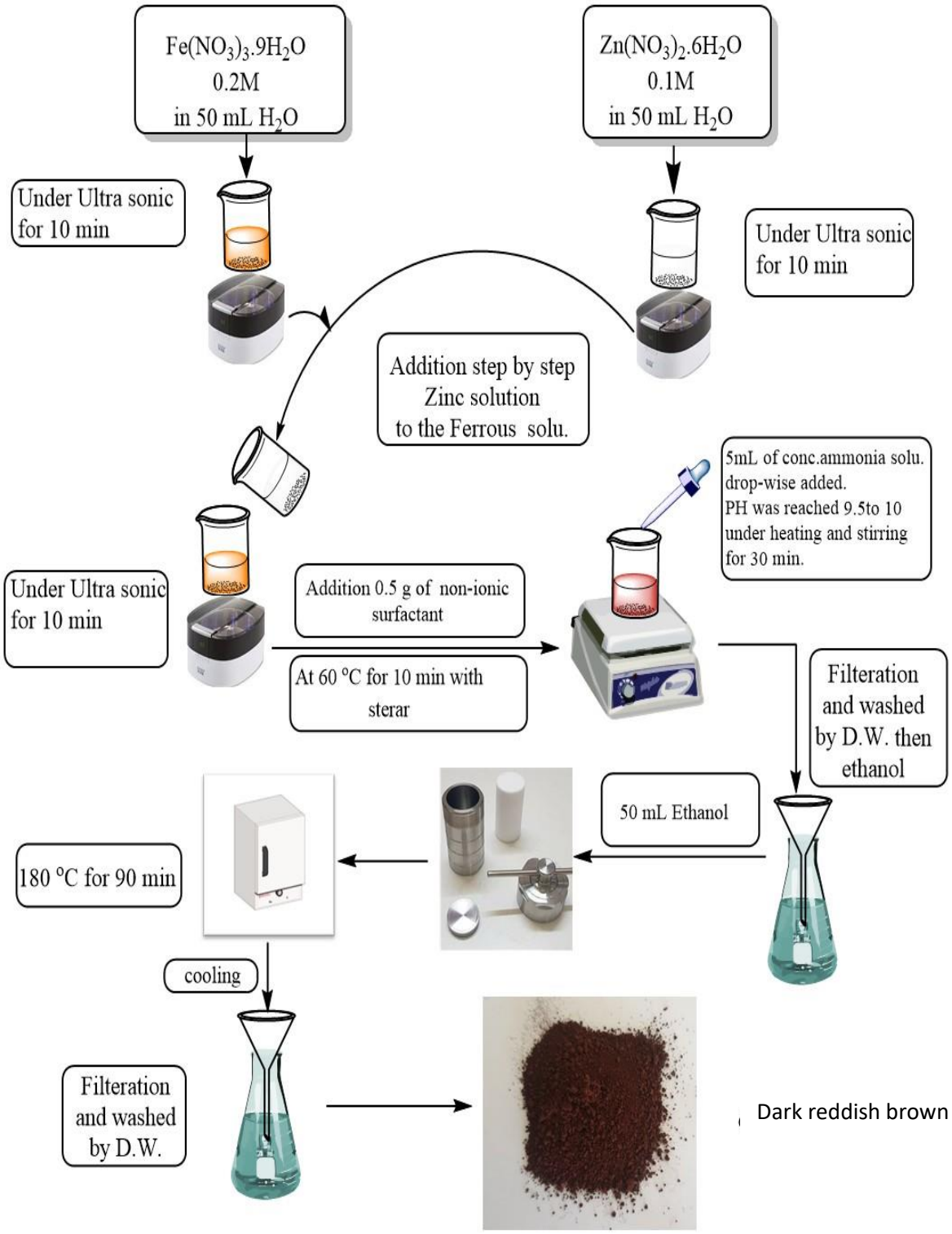

Figure (2-2). The schematic diagram of the steps of Zinc Ferrite nanoparticle preparation

2.3.3 Preparation of Zinc-Nickel Ferrite semiconductor

1. Solution 1: Nickel ferrite NPs solution was prepared from dissolved 1.00 g in 50 mL ethanol under ultrasonic waves high-frequency ≥ 100kHz for 60 min at 70 ^{o}C .
2. Solution 2: Zinc ferrite NPs solution was prepared from dissolved 1 g in 50 mL ethanol under ultrasonic waves high-frequency ≥ 100kHz for 60 min at 70 ^{o}C.
3. In ultrasonic bath high-frequency ≥ 100kHz, solution 2 was added step by step to solution 1 and mixed for 90 min at 70 ^{o}C.
4. Heating and stirring continued The mixture at 80 ^{o}C to remove all the ethanol
5. Collect the deposit

   All of steps for preparation Zinc-Nickel Ferrite shown in figure (2-3).

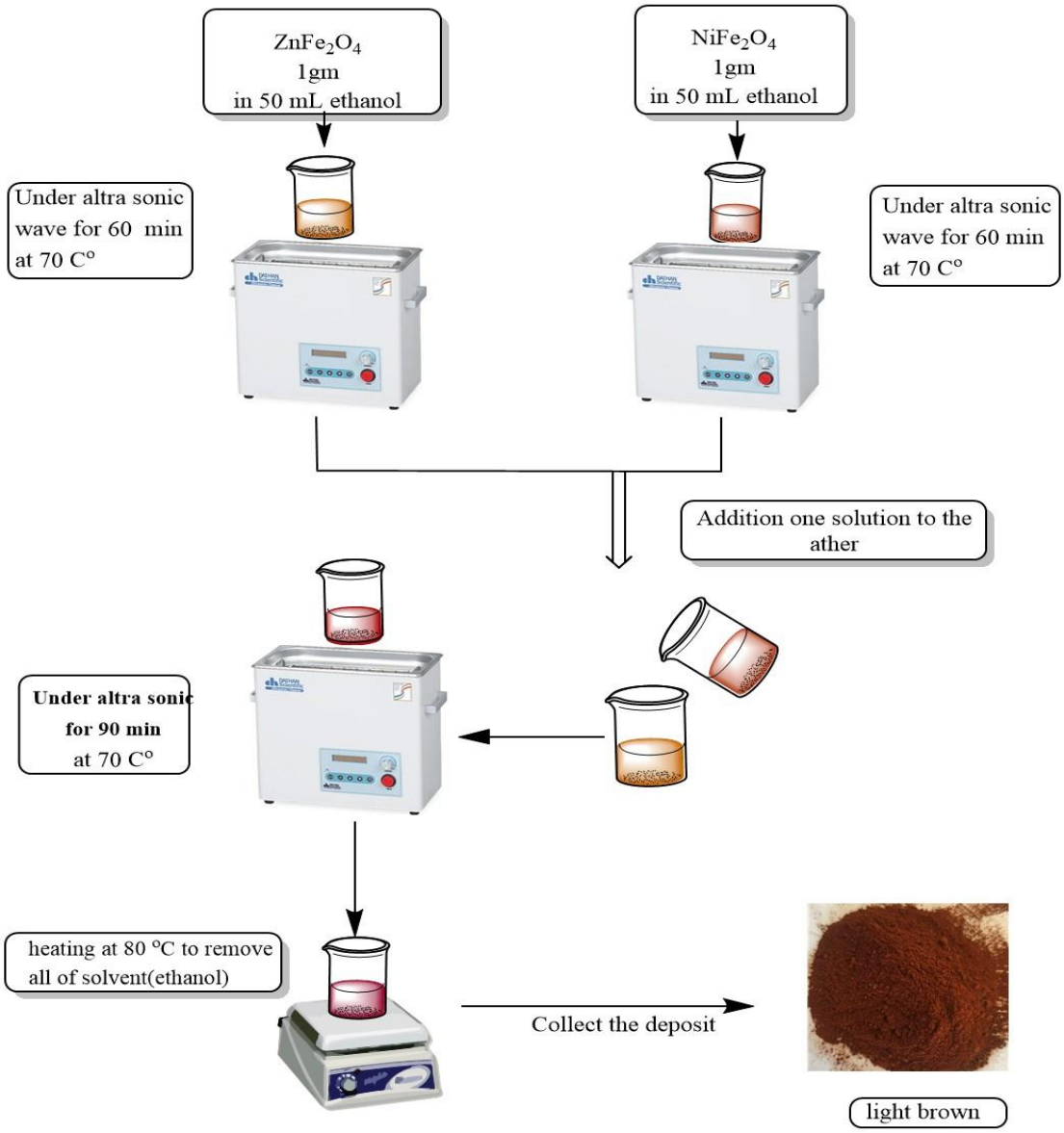

Figure (2-3). The schematic diagram of the steps of Zinc Ferrite nanoparticle preparation

2.4 Characterization of semiconductors

2.4.1 FT-IR Spectra

The FT-IR spectra of the semiconductors were obtained using CsI powder in the range (250-4000) cm^{-1} using (FT-IR Spectroscopy, Shimadzu).

2.4.2 X-Ray Diffraction Spectroscopy (XRD)

The mean Crystal sizes (L) of all samples were calculated by Scherrer's equation eq. 2-6 [70,71]. XRD data were analyzed by Shimadzu, Lab X XRD 6000 instrument. This instrument is used Cu as a target source with wavelength 1.54060 Å, voltage 40.0 kV and current 30 mA, speed is equal to 12.0000 (deg/min) and angle (2θ) range between (20 – 80) deg.

$$\boldsymbol{L = \frac{K.\lambda}{\beta.Cos\theta}} \qquad \ldots (\mathbf{2-6})$$

Here: k is the Scherer's constant which depending on the dimensionless shape (used 0.94 spherical and 0.9 semi spherical), λ is the wavelength (used 0.15406 nm for Cu kα), θ is a Bragg diffraction angle and β is (FWHM) the full width halfmaximum that measured in degrees.

2.4.3 Scan Electron Microscopy (SEM)

The scanning electron microscopy image was measured for all samples (Nickel Ferrite , Zinc Ferrite and there Composite) using SEM analysis (FESEM FEI Nova Nano SEM 450).USA.

2.4.4 Energy Dispersive X-Rays (EDX)Analysis

The EDX spectra for all samples were performed via using SEM instruments to validate the sample's components as a percentage of atoms in samples.

2.4.5 Bandgap Energy Measurements

The optical energy bandgaps Eg in eV were determined for all photocatalyst samples using the Tauc equation[72,73] , as seen in equations 2-7 and 2-8.

$$\alpha h\nu = k(h\nu - Eg)^m \quad \ldots (2\text{-}7)$$

$$\alpha = (2.3026\ A)/t \quad \ldots (2\text{-}8)$$

Where α , h, ν, k, t, A, and m are absorption coefficient, Plank's constant the light, frequency, optical constant, thickness, the absorbance and constant value equal to ½ or 2 for direct and indirect transitions, respectively.

2.4.6 Magnetic Susceptibility

The magnetic susceptibility measurements of the complex were conducted at laboratory temperature using the Faraday method by suspending the model whose gram-magnet sensitivity was to be measured from the cuff of a sensitive scale placed between the poles of a powerful electromagnet in order to obtain the gram sensitivity value (Xg). To the molar sensitivity (XM) and then to the atomic sensitivity (XA) after extracting the value of the correction factor (D) from tables of Pascal constants, and then calculating the values of the effective magnetic moment ($\mu_{ef\,f}$) according to the following law:

$$\mu_{ef\,f} = 2.828\sqrt{X_A T}\ B.M \quad \ldots\ldots\ldots\ldots (2\text{-}9)$$

Here: (XA) = atomic sensitivity, T= absolute temperature B.M = Bohr magneton is a unit of magnetic moment measurement.

2.5 Photocatalytic Decolorization Reaction dye

The Photocatalytic Decolorization Reaction removal of dyes was applied by photocatalysts of nickel and zinc ferrite and their composite. A homemade photo reactor was used to carry out the photoreaction in Figure (2-4). This photoreactor is equipped with a 400-watt UV light that is put inside a wooden box as a reactor's body to prevent the UV-A light risk. The light source was positioned directly above the Pyrex glass beaker (500 mL) to ensure a good focusing of it.

Moreover, a magnetic stirrer, a Teflon bar, and used two different fans to fix and eliminate the generated heat from the lamp [74]. First, without using the lamp for 15 minutes, the dark reaction was done. Following the adsorption stage, the suspension was exposed to UV light, and about 5 mL of aliquots were collected at intervals time started from 5 minutes until 35 minutes. The collected suspensions were centrifuged twice at 6000 rpm for 20 minutes. The absorbance of the resulting filters was measured at 593 nm using a UV-Vis spectrophotometer. The apparent rate constant for the first order equation and the % efficiency of dye photo-decolourization [75] were calculated using Eq 2-10 and 2-11.

$$\ln\left[\frac{C_o}{C_t}\right] = K_{app} \cdot t \qquad \text{.....} \qquad (2\text{-}10)$$

$$E\% = \left[\frac{C_o - C_t}{C_o}\right] \cdot 100 \qquad \text{.....} \qquad (2\text{-}11)$$

Here: C_o and C_t are the initial concentration of the Dye at the dark reaction (without radiation) and after irradiation, respectively.

Figure (2-4). Diagrammatic representation of a Homemade Photocatalytic Reactor Unit.

2.6 Calibration Curve of Alkali Blue 4B dye

In all kinetic experiments, the residue concentrations of Alkali Blue 4B dye before irradiation (Co) and after irradiation (Ct) were determined by using a calibration curve. The series of Alkali Blue 4B dye concentrations were prepared in ranged (1-20) ppm, which obeys Beer's law, as shown in table (2-3) and figure (2-5).

Table (2-3): Calibration Curve Data of Alkali Blue dye Concentrations.

C/ppm.	Abs.
1	0.092
2.5	0.205
5	0.28
7.5	0.328
10	0.415
15	0.552
20	0.718

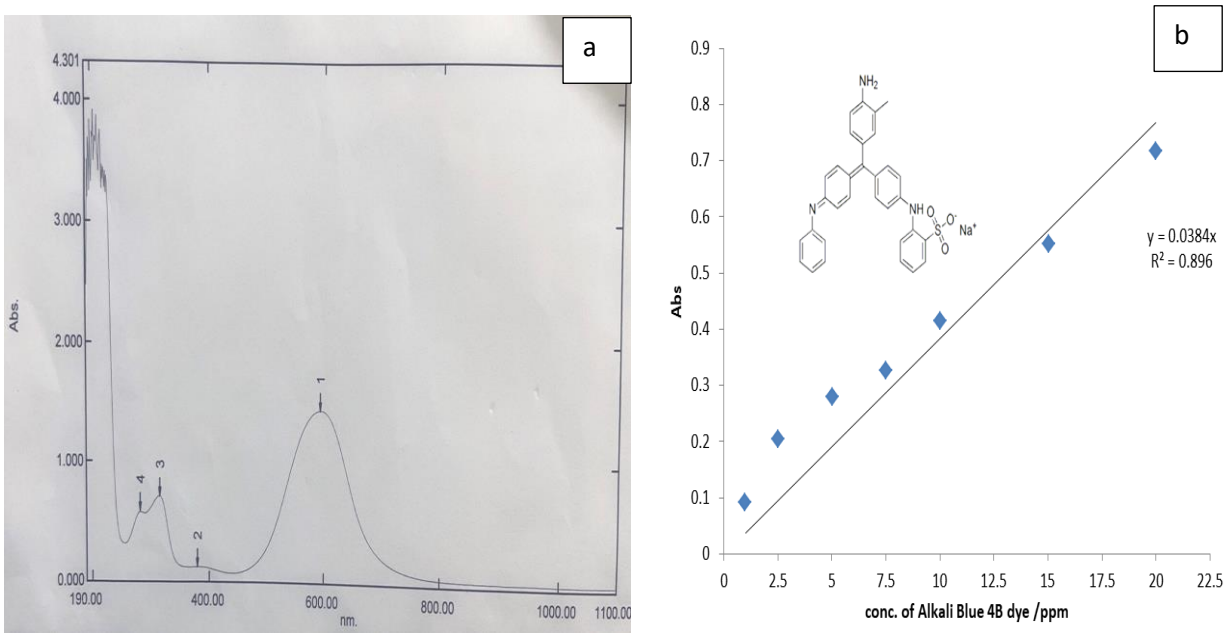

Figure (2-5): (a) UV-Visible absorpation spectrum for Alkali Blue dye solution (b) Calibration curve at different concentrations of Alkali Blue dye in aqueous solution at 593nm wavelength.

2.7 Light Intensity Measurements

The light intensity for the UV-A light source which used in this work was determined using the chemical actinometric method [76]. An exact 100 mL of actinometric solution was exposed to UV-A light of photoreactor. The actinometric solution has been prepared by mixing from 40 mL of 0.15 M $Fe_2(SO_4)_3.H_2O$ with 50 mL of 0.45 M $K_2C_2O_4.H_2O$ and 10 mL of 0.05 M H_2SO_4 with the presence of atmospheric oxygen under irradiated UV-A lamp's light. The yellowish-green solution was produced; from the last solution, approximately 2 mL of irradiated solution with regular periods at (5, 10, and 15) min was taken and centrifuged at 4000 rpm with 10 min. 0.5 mL of filtered was added to 2.5 mL from 1% from 1,10 – phenonethroline as a reagent, that will produce reddish-orange complex as ferroxalate complex ($[Fe^{2+} (C_2O_4)_2]^{2-}$), as noted in equations from (2-15) to (2-18), which absorbed at 510 nm.

$$[Fe^{3+} (C_2O_4)_3]^{3-} + hv \longrightarrow [Fe^{2+} (C_2O_4)_2]^{2-} + C_2O_4^{\cdot -} \qquad (2\text{-}12)$$

$$[Fe^{3+} (C_2O_4)_3]_{3-} + hv \longrightarrow Fe^{2+} + 2(C_2O_4)^{2-} + C_2O_4^{\cdot -} \qquad (2\text{-}13)$$

$$[Fe^{3+} (C_2O_4)_3]^{3-} + C_2O_4^{\cdot -} \longrightarrow [Fe^{2+} (C_2O_4)_2]^{2-} + C_2O_4^{\cdot -} + 2CO_2 \qquad (2\text{-}14)$$

$$2[Fe^{3+} (C_2O_4)_3]^{3-} \longrightarrow 2[Fe^{2+} (C_2O_4)_2]^{2-} + C_2O_4^{2-} + 2CO_2 \qquad (2\text{-}15)$$

The following equations were measured the light intensity (I_o): [77]

$$\text{Moles of } Fe^{2+} = \frac{V1 \times V3 \times A_{(510\ nm)}}{V2 \times l \times \varepsilon_{(510\ nm)} \times 10^3} \qquad (2\text{-}16)$$

$$I_o = \frac{\text{moles of } Fe^{2+}}{\Phi_\lambda \times t} \qquad (2\text{-}17)$$

$$I_o = 3.189\times10^{-7} \text{ Enestine } s^{-1}$$

Here: (V_1 = 100 cm^3) is the total volume of irradiation chemical-actinometric solution, (V_3 = 3 cm^3) is the volume of irradiation solution that added to the reagent 1,10-phenonethroline solution, (V_2 = 0.5 cm^3) is the volume of filtered irradiation solution, the length of the optical path 1.2 is the quantity yield [78].

A_{510} is the average absorption of ferrioxalate solution after various internal irradiation times, which is mixed with 1,10-phenonethroline, molar absorption (ε = 1.045 x 10^4 L mol^{-1} cm^{-1}) and (t) the average irradiation time (10 min).

2.8 Activation Energy

The apparent activation energy (Ea) of photocatalytic decolorization of the complex solution has been determined using the Arrhenius equation. Using the graph's linear relationship to the Arrhenius equation, the dye's photo-decolorization reaction's apparent activation energy was found [79].

$$\ln k_{app} = \frac{-E_a}{RT} + \ln A \qquad \text{...(2-18)}$$

Here. kapp is an apparent constant rate, T is the reaction temperature, R is a constant gas (8.314 J mol^{-1} K^{-1}) and A is a frequency constant.

2.9 Thermodynamic Parameters

The thermodynamic parameters are calculated from Ering-Pollani equation plot (2-19), to determine the type and direction of this photo-reaction and Gibbs equation (equation 2-20), which used to calculate the enthalpy change ($\Delta H^{\#}$), the entropy change ($\Delta S^{\#}$) values and the free energy($\Delta G^{\#}$) respectively [80].

$$\ln\left(\frac{k_{app}}{T}\right) = \frac{-\Delta H^{\#}}{RT} + \left(\ln\left(\frac{k_B}{h}\right) + \frac{\Delta S^{\#}}{R}\right) \qquad \text{...(2-19)}$$

$$\Delta G^{\#} = \Delta H^{\#} - T\Delta S^{\#} \qquad \text{...(2-20)}$$

Where :k_B is Boltzman constant (1.380649×10^{-23} m^2 kg s^{-2} K^{-1}) and h is Planck constant (6.626×10^{-34} Js), A is frequency factor.

2.10 Hemolysis assay

This test used the blood hemolysis method, which is an in vitro disruption of human red blood cells (RBCs) by Nickel and Zinc Ferrite and their composite, as well as the blood sample of sixty healthy, nonsmoking donors [81]. Typically, 15µL of two spinal solutions were added to 0.1 mL of blood at the concentrations of (25×10^3 µg/mL) and 15 µL of composite was added to 0.1 mL of blood at the concentrations of (15×10^3 µg/mL), and the mixture was well mixed for 5 seconds.

To avoid excess hemolysis, 10 mL of normal saline was addtion to the mixture. The mixture was centrifuged at 3000 rpm for 10 minutes. Then the absorbance of all samples was measured at the wavelength 540 nm. In addition, the purpose of this test is to measure the percentage of hemolysis caused by Ni and Zn Ferrite NPs and their compounds up to 100 percent. As a result, diluting blood with 100 times as much distilled water resulted in 100 percent total hemolysis. After evaluating the absorption using Triton X-100 as the positive control, the hemolysis percentage was calculated as the following equation[82]:

$$\textbf{\% Hemolysis} = \frac{(\mathbf{AT}-\mathbf{AS})}{(\mathbf{A100\%}-\mathbf{AS})} \times \mathbf{100\%} \qquad \textbf{.....(2-21)}$$

Where, AT is the absorbance of the test solution, AS is absorbance of the normal saline, and A 100% is the absorbance of 100% hemolysis.

CHAPTER THREE

Results & Discussion

Chapter Three

Results and Discussion

3.1 Characterization of photocatalysts

In this project, FTIR, XRD, SEM, and Bandgap (Bg) measurements were utilized to evaluate the characterizations of the studied samples.

3.1.1. FT-IR spectra of photocatalysts

FT-IR spectroscopy was used to investigate the features of using samples as photocatalysts in this work. The FT-IR spectrum of Nickel ferrite shown in figure (3-1), in general, FT-IR spectra of all spinels, and especially ferrites includes two primary wide metal oxygen bands are seen below about 600 cm^{-1} beyond tetrahedral and octahedral sites [83]. Since the bond between the tetrahedral is short, it lives at a place where there is a lot of vibration. Nickel ferrite has an inverse spinel structure group; consequently, the highest-frequency band, found at ν1 = (563.23-651.93) cm^{-1}, is attributed to tetrahedral site vibrations of (Fe-O) tetra, while the lowest-frequency band, found at ν2 = (362.63-428.21) cm^{-1}, is attributed to octahedral site vibrations of (Ni-O) These findings are consistent with those published for metal ferrite[96]. The wide bands at 3456.55 cm^{-1} and 1620 cm^{-1} correspond to the mode of stretching of H_2O and OH molecules and the mode of bending of H_2O molecules, respectively [85].

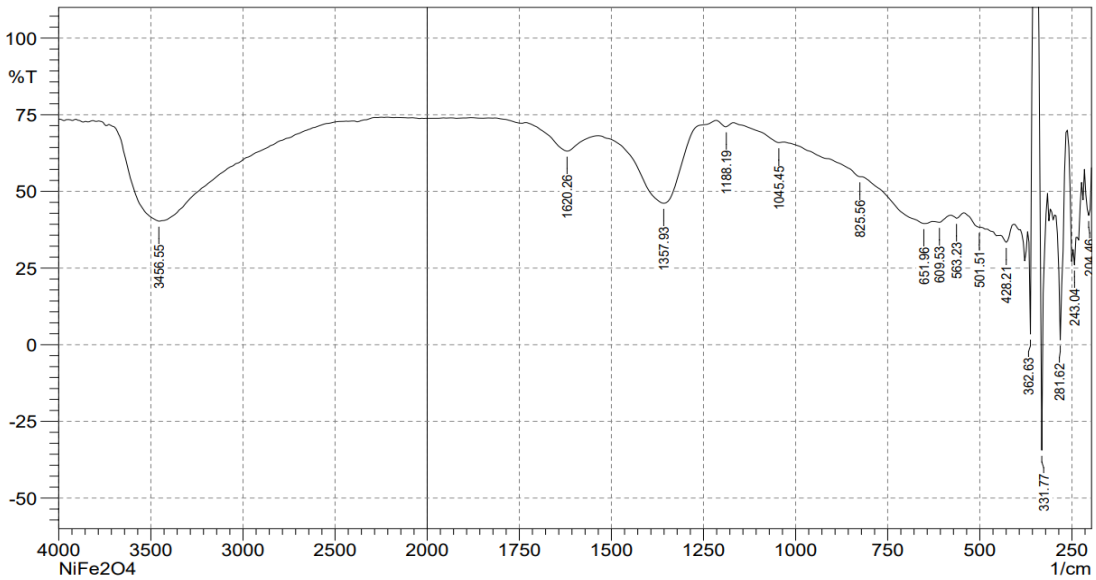

Figure (3-1). FTIR spectrum images of the inverse spinel $NiFe_2O_4$ nanoparticle.

frequency band (559 to 648) cm^{-1} is attributed to the stretching vibration of the chemical bond of (Zn^{2+} –O^{2-}) in the tetrahedral sites. The range of wave numbers for the interaction of metal-oxygen in crystal lattices is found to be (474-636) cm^{-1} and (550-750) cm^{-1} for octahedral and tetrahedral vibration modes, respectively. These results are in agreement with that previously reported [86,87]. Moreover, the peaks at 3448 cm^{-1} and 1612 cm^{-1} are beyond the stretching vibration and bending mode of water molecular [88].

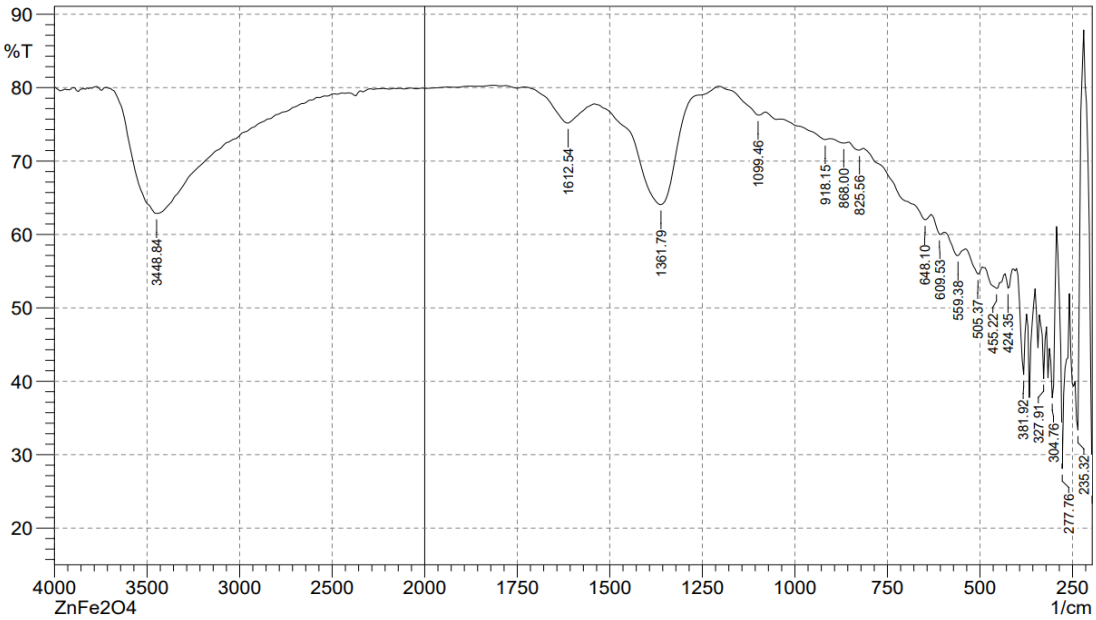

Figure (3-2). FTIR spectrum images of the normal spinel $ZnFe_2O_4$ nanoparticle.

The FT-IR of composite that shown in figure (3-3),two main broad absorption bands are appeared in the range of 381 cm^{-1} to 594 cm^{-1}. This band is made up of the stretching vibrations of the metal ions at the tetrahedral site. It has a wave number of υ1, and can be found in the range of 536 - 594 cm^{-1}. The other band appeared in the range of 381 cm^{-1} to 459 cm^{-1} is labeled as υ2 and corresponds to stretching vibrations in octahedral locations of metal ions. These two bands have been found in previous studies on spinel ferrites. In fact, peaks about 3400 cm^{-1} correspond to the O-H stretching vibrations of water molecules[89]. The slight increase in the wavenumber of the υ1 positions of the zinc ferrite spinel can be observed after the formation of the composite. The reason is attributed to

Zn ferrite has a normal spinel structure where Zn^{2+} cations occupy the tetrahedral sites (A sites) and Fe^{3+} cations occupy the octahedral sites (B sites). On the other hand, Ni ferrites have inverse spinel structure in which octahedral sites are occupied by both Ni^{2+} and Fe^{3+} cations. Accordingly, when Ni^{2+} cations are added in expense of Zn^{2+} cations, they occupy the octahedral sites pushing part of Fe^{3+} cations from the octahedral to the tetrahedral sites. As Fe^{3+} cations are smaller in size and lighter than Zn^{2+} cations, atomic vibration of the tetrahedral sites increases as well giving rise to shift of the absorption band towards higher wavenumbers[90].

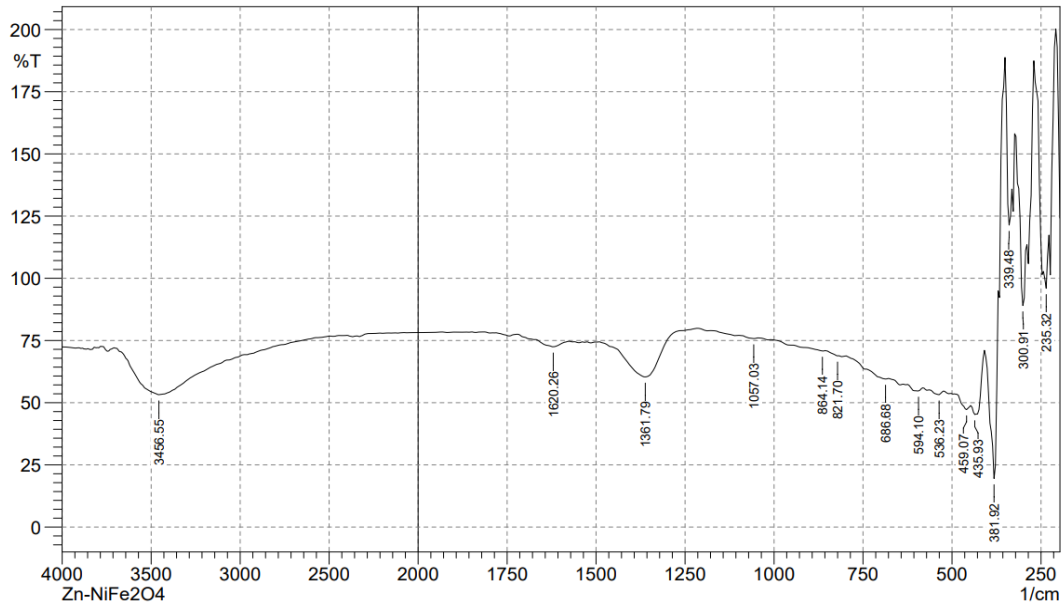

Figure (3-3). FTIR spectrum images of the composite Zn-$NiFe_2O_4$ nanoparticle.

The wavenumber (1361,118,1357) cm^{-1} that seen in all chart refer to the C-H bending vibrations and C-N stretching vibration because of use a hexamine as a non- polar surfactant, a capping agent and stabilizer for Ni-Ferrite and Zn-Ferrite[91].

3.1.2 X-ray Diffraction patterns (XRD)

The XRD is one of the most efficient methods for identifying the crystal's molecular structure. The figure (3-4) shown all synthetic samples of Nickel and Zinc Ferrite and their composite were analyzed by XRD.

The XRD data of $NiFe_3O_4$ powder produced in the laboratory (Card No.: 00-003 0875) revealed diffraction patterns at 2θ = 35.77°, 43.51°, and 63.04° as, which correspond to the (311), (400), and (440) planes, respectively. In contrast to the diffraction patterns of flawless crystals, imperfect crystals exhibit diffraction patterns[92, 93]. These results are in agreement with another study for preparing the $NiFe_2O_4$ nanoparticle before calcinated it [94].The analysis of XRD result of the $ZnFe_2O_4$ peaks were embedded in an amorphous matrix that due to no calcination. The results give low intensities and broad peaks with diffraction patterns at 2θ of 29. 9°, 35.30°, 36.40° 42.78°, 51.8°, 55.05° and 62.2°, that ascribed to the reflection of (220), (311), (222), (400),(331), (422), and (440) planes of the spinel $ZnFe_2O_4$, respectively. These peaks are in agreement with results by litratures [95,96].

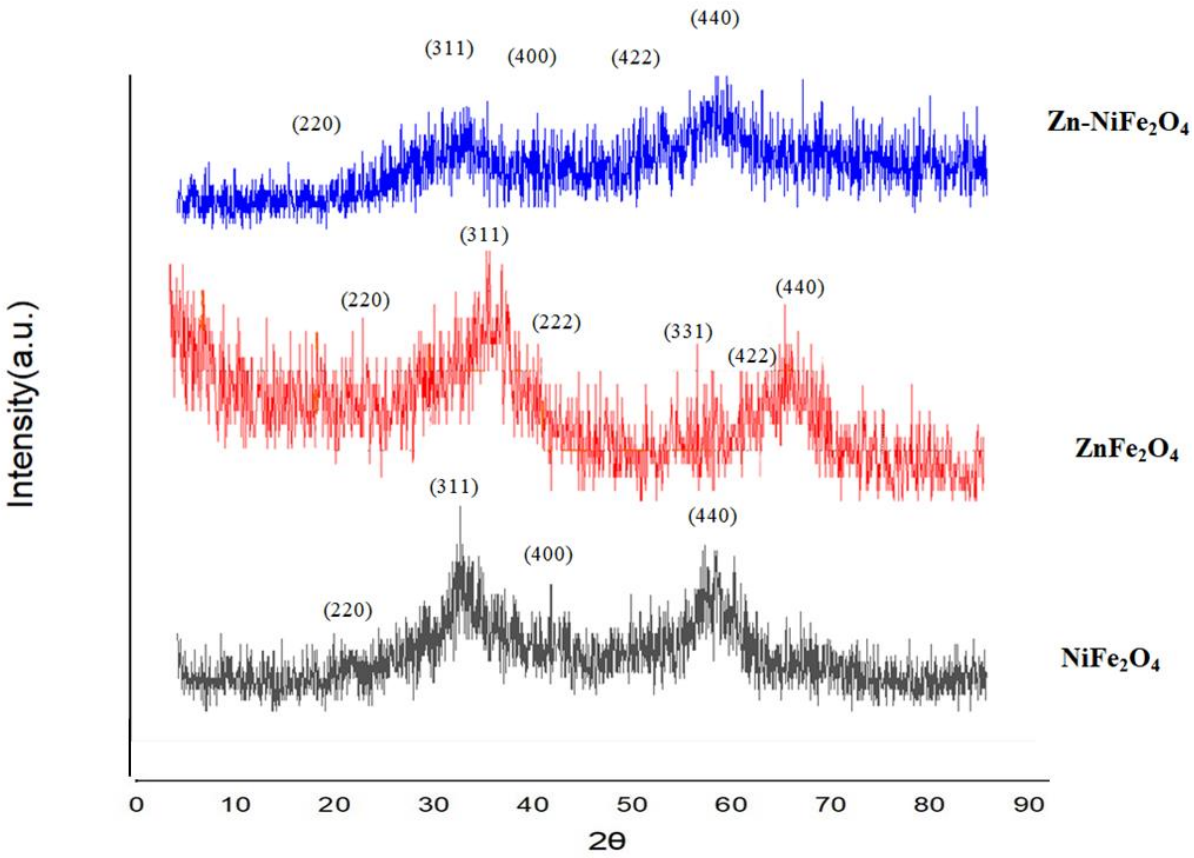

Figure (3-4). The XRD patterns of samples $NiFe_2O_4$, $ZnFe_2O_4$ and there composite

The peak 2θ values of 30.26°, 36.6°,48.61°, 53.19°, and 61.0° are indexed as (220), (311), (400), (440) and (442) planes are in firm agreement with the outcomes of samples through the JCPDS (card no.82-1042) confirming the formation of a cubic phase with a ferrite system structure[97]. Whereas, Ni–Zn ferrites can be crystallized in the mixed spinel phase in which Ni^{2+} and Zn^{2+} occupy the octahedral and tetrahedral site but Fe^{3+} ion shared between two sites[98]. As shown in Figure (3-4) in composite zinc-nickel ferrite, the 2 sites of spinal zinc ferrite suffer from lower angles towards the spinal nickel ferrite sites, which mean that nickel has the largest value in the compound, which is the base as seen later in (EDX).

The mean crystallite size (L) in nm was calculated by using the Scherer's equation(2-6).For inverse spinal $NiFe_2O_4$ powder found to be 20.13 nm**.** This finding improved the bending between Ni^{2+} and Fe^{3+} through the metallic bonds in the crystal lattices of the spinal $NiFe_2O_4$ nanoparticle, which is due to their almost ionic radii of 0.59 Å and 0.609 Å, respectively, and for normal spinal $ZnFe_2O_4$ was found to be equal 16.98 nm, the ionic radii of Zn^{+2} and Fe^{3+} equal to 0.74 Å and 0.609 Å, respectively[99]. The value of mean crystallite size for zinc ferrite proved the prepared spinel is nanomaterial and amorphous [100]. In other hand, the mean crystal size for composite Zn-$NiFe_2O_4$ it was found equal to 28.82 nm, this increasing in crystalline size come from the composite shod be formed and also with further increase in the content of Ni^{2+} ions in the structure. This could be explained by the change of the structure from normal ($ZnFe_2O_4$) to inverse ($NiFe_2O_4$) spinel. The distribution of divalent metal cations at specific tetrahedral and octahedral positions is responsible for the relaxation of the structure[101].

3.1.3 Scan Electron Microscopy (SEM)

The SEM has been the primary instrument for identifying the surface morphology and basic physical characteristics of materials. It is used to determine the form and size distribution of the material's particles. Using SEM spectra of spinel $NiFe_2O_4$, $ZnFe_2O_4$, and their nano composites, the surface morphology of the samples was studied. In (Figure 3-5) the SEM analysis reveals of Nickel ferrite that the sample demonstrates a compacted order of homogeneous nanoparticles with a nearly spherical shape that agglomerated into a broccoli-like nanoparticle shape. The particle size is equal to 30.67 nm that more valuable than the mean crystal size[102,103] because of most particles are assembled as a polycrystalline. This behavior may be attributed to the small dimensions of nanoparticles and has a high density [104]. The $NiFe_2O_4$ nanoparticle pieces of evidence it is a polycrystalline structure.

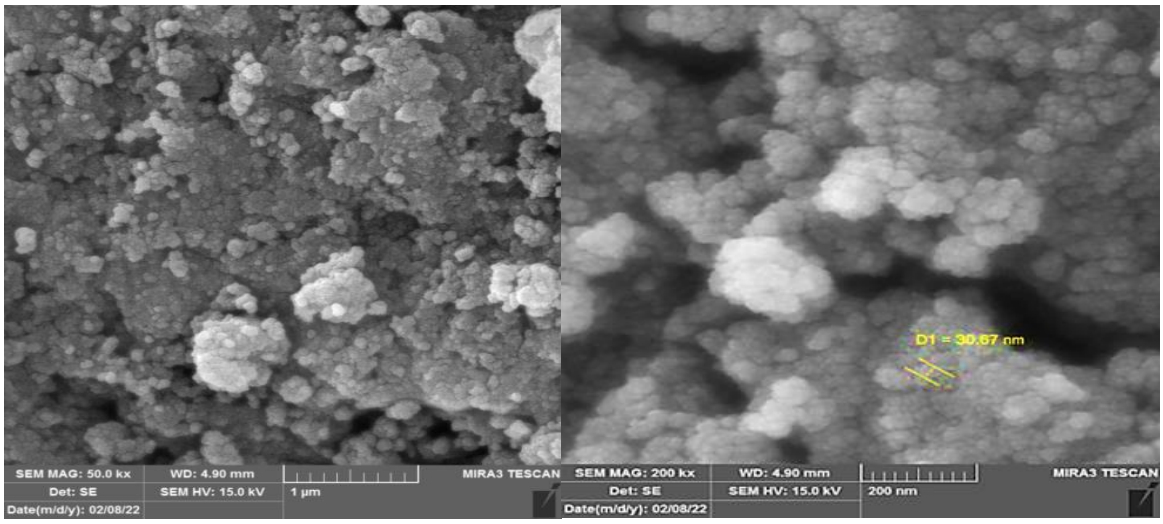

Figure (3-5). The SEM of samples $NiFe_2O_4$ nanoparticles

Figure (3-6) is a SEM picture of a $ZnFe_2O_4$ sample, which demonstrates that the sample has a tight arrangement of approximately spherical nanoparticles. This growth of Zn ferrite nanoparticles is based on the features of the surfactant, which leads to the formation of this optimal shape. Most particles are assembled, hence, the particle size is more than the mean crystal size [105, 106], and equal to 27.78 nm, this behaviour indicates the $ZnFe_2O_4$ nanoparticles are polycrystalline in their structure and found to be as a cauliflower.

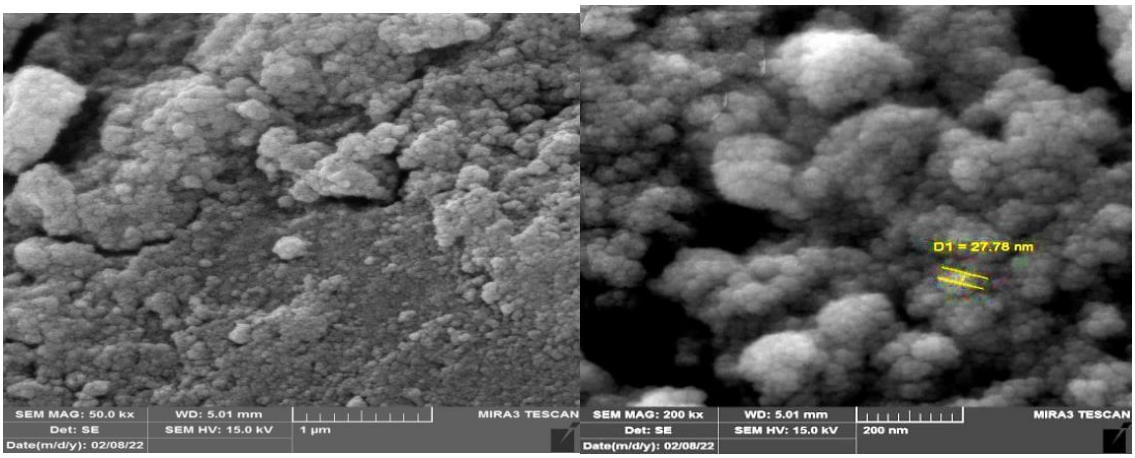

Figure (3-6). The SEM of samples $ZnFe_2O_4$ nanoparticles

The SEM of Zn-Ni Ferrite showed the average particles size of 40.19 nm. The particles were spherical in shape, homogenously distributed with little agglomerates due to their magnetic property as shown in (Figure 3-7). The agglomeration is caused by the nanoparticles' high surface energy, which results from their high surface area to volume ratio. Due to the size of the nanoparticles, the surface area of nanoscale materials rises while the volume stays constant. Therefore, nanoparticles have a naturally high ratio of surface area to volume, which contributes to their high surface energy. Because the particles have so much energy, they stick together to lower their surface energy[107].

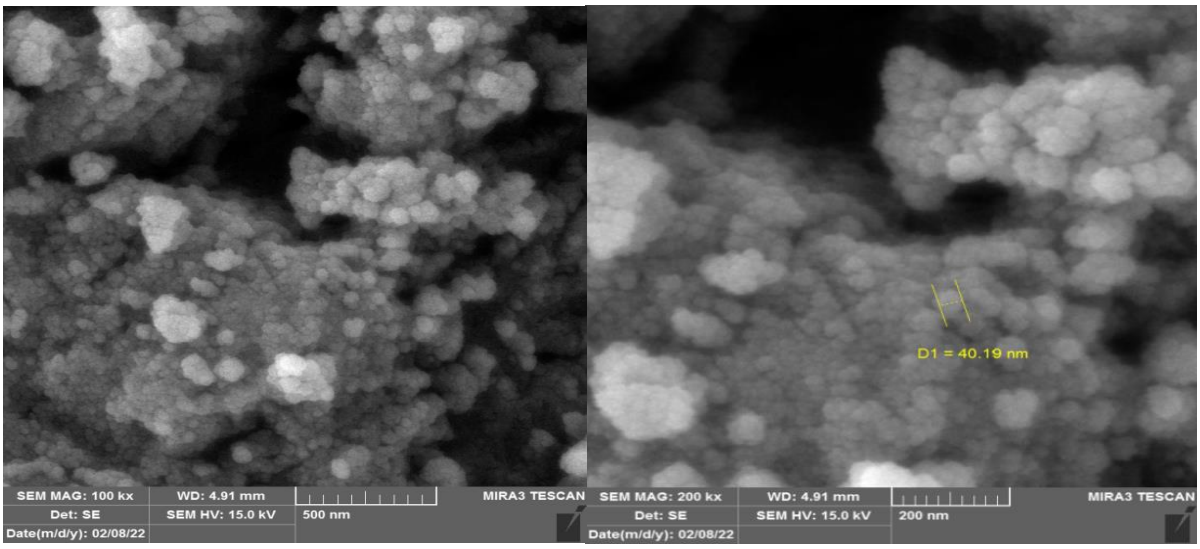

Figure (3-7). The SEM of Zn-$NiFe_2O_4$ Nanocomposite

3.1.4 Energy Dispersive X-Rays (EDX)

The EDX spectra used to validate the sample's components, as seen in Figures (3-8) to (3-10). The spinal nickel ferrite demonstrates the homogeneous distribution of Ni, Fe, and O in the polycrystalline layers, devoid of impurities. Also, the weight percent (wt%) of Fe is found to be twice the weight percent (wt%) of Ni. This is in good agreement with the stoichiometry preparation ratio (2:1) used during the preparation process[108,109].

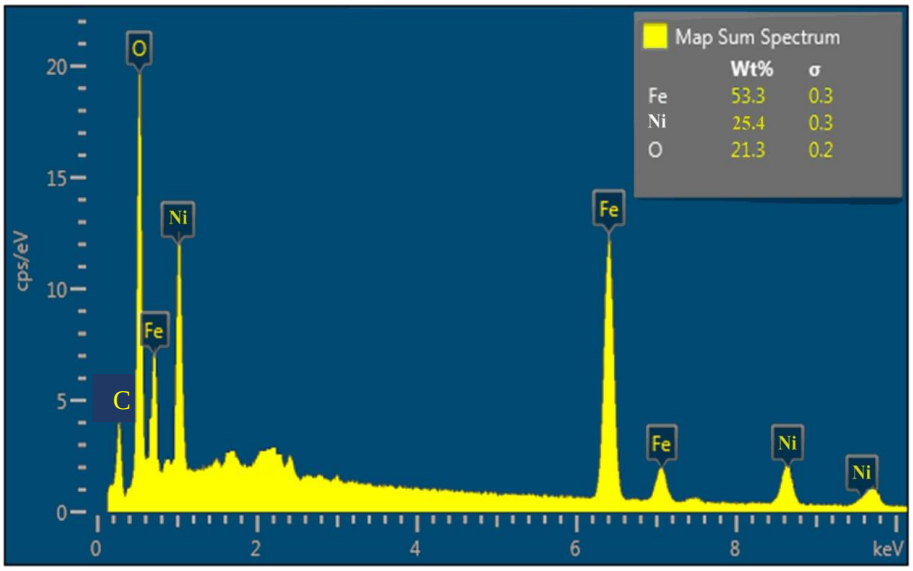

Figure (3-8). EDX spectrum of $NiFe_2O_4$ Nanocomposite

This case likes to spinal Zinc Ferrite catalyst that is made of only Zn, Fe, and O in the same ratio(2:1) of, Fe: Zn. This is in line with what has been written inreferences[110,111].

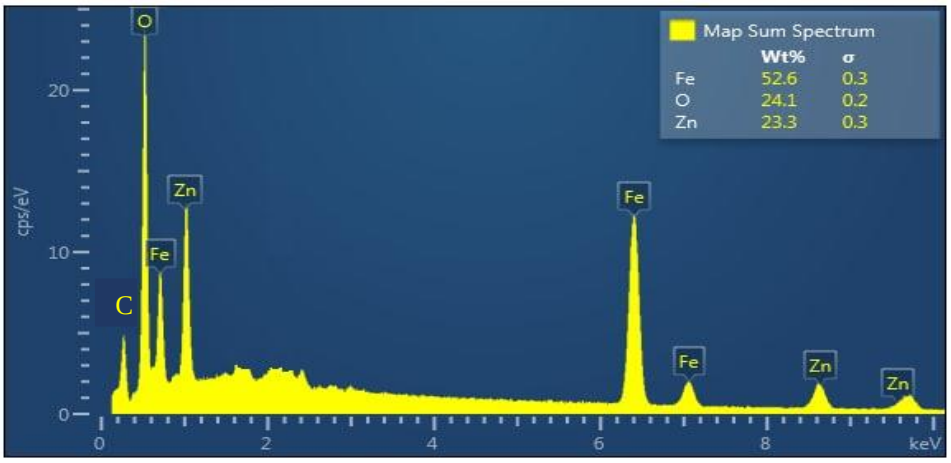

Figure (3-9). EDX spectrum of $ZnFe_2O_4$ Nanocomposite

Using the EDX detector, the elemental composition of $ZnNiFe_2O_4$ was detected. The distribution indicates that the elements (O, Fe, Zn, and Ni) are present in proportion to the ratio of zinc ferrite to nickel ferrite, which is 1:1. This is consistent with the references [112].

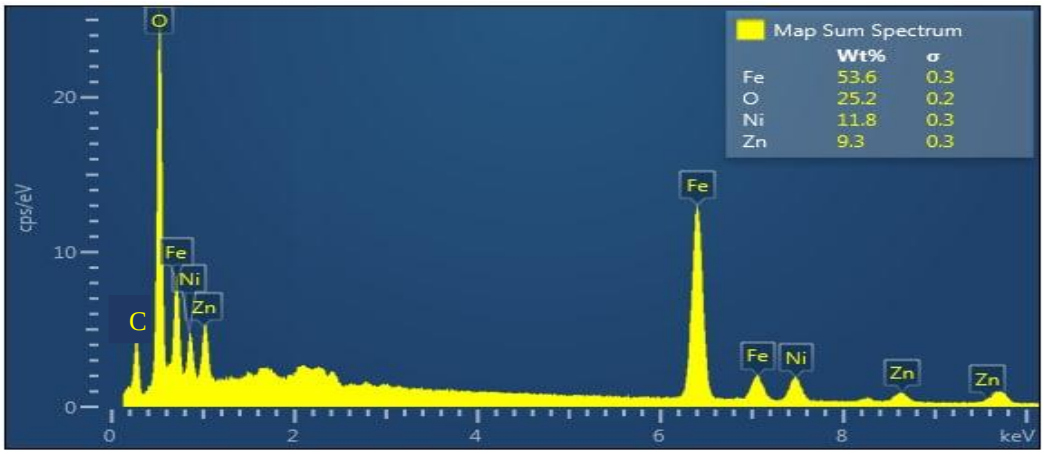

Figure (3-10). EDX spectrum of $ZnNiFe_2O_4$ Nanocomposite

In all specta of EDX that seen the C peak that beyond to use a hexamine as template, which is proved by FT-IR spectra

3.1.5 Band Gap Energy Measurements

On the basis of Tauc equation graphs [113,114], the band gap energies of studied samples were calculated. In Figure(3-11) the indirect band gaps for photocatalyst Nickel ferrite and zinc ferrite were equal to 2.05 eV [127,128] and 2.15 eV[109], respectively. Moreover, the band gap energy of prepared composite was found to be indirect were equal to 1.56eV [117,118]. The composite has a less value for band gap because it has a more mean crystal size and particle size values compared with values of Ni ferrite and Zn ferrite.

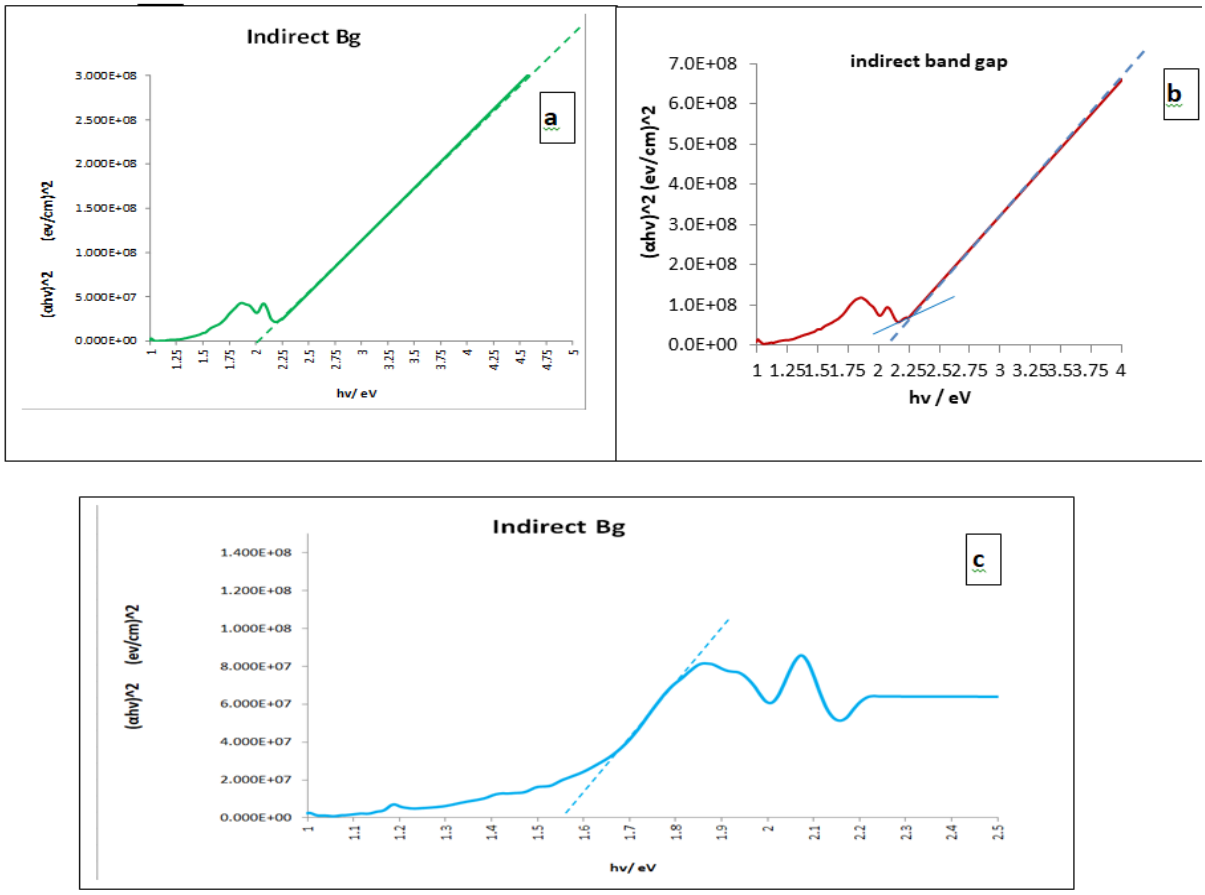

Figure (3-11). Band gap as an indirect of (a) spinal Nickel ferrite , (b) spinal Zinc ferrite and (c) Zn-Ni ferrite composites.

3.1.6 Magnetic Susceptibility

The magnetic sensitivity of the prepared metal complexes was determined at 306 K. Pascal's constants were also used to adjust the magnetic characteristics of atoms in molecules, inorganic radicals, and metal ions. The following formulae were used to obtain the values (2-9) and (1, 2-3) of the magnetic moment (μ_{eff}) practically and the equation (3-4) to calculate it theoretically [119]:

$$\mu_{ef\,f} = 2.828\sqrt{X_A\,T}\ \mathrm{B.M.} \qquad (2-9)$$

$$X_A = X_m - D \qquad (1-3)$$

$$X_m = X_g \times M.wt \qquad (2-3)$$

$$\mu_{ef\,f} = \sqrt{n(n+2)} \qquad (3-3)$$

Where μ_{eff}, denotes the effective magnetic moment, M.wt is molecular weight, B.M is magnetic moment unit (Bohr magneton), D = The sum of the atoms of each element x Pascal modulus x 10^{-6} .

Table 3-1 experimental and theoretical calculations of magnetic susceptibility for Zinc ferrite, Nickel ferrite and zinc-nickel ferrite.

Fe(III)-Complex Theoretical accounts	Zinc Ferrite μ_{eff} calculated	Nickel Ferrite μ_{eff} calculated	Zinc-Nickel Ferrite μ_{eff} calculated
$_{26}Fe\ [Ar]_{18}\ 4s^2\ 3d^6$ $_{26}Fe^{3+}\ [Ar]_{18}\ 4s^0\ 3d^5$ $\mu_{eff} = \sqrt{n(n+2)}$ $\mu_{eff} = \sqrt{5(5+2)}$	Xm = Xg x M.wt = 5.06 x 10^{-5} x 241.52 = 122.21 x10^{-4} XA= Xm - D =122.21 x10^{-4} – (- 53.4 x 10^{-6}) = 122.74 x10^{-4} $\boldsymbol{\mu_{eff} = 2.828\sqrt{X_A T}\ B.M.}$	Xm = Xg x M.wt = 3.69 x 10^{-5} x 234.383 = 69.38 x10^{-4} XA= Xm - D =69.38 x10^{-4} – (- 50.4 x 10^{-6}) = 69.88 x10^{-4} $\mu_{eff} = 2.828\sqrt{X_A T}\ B.M.$	Xm = Xg x M.wt = 1.506 x 10^{-5} x 299.763 = 45.14 x10^{-4} XA= Xm - D =45.14 x10^{-4} – (- 65.4x 10^{-6}) = 45.8 x10^{-4} $\mu_{eff} = 2.828\sqrt{X_A T}\ B.M.$
$\boldsymbol{\mu_{eff} = 5.9\ B.M.}$	**μ_{eff} = 5.48 BM**	**μ_{eff} = 4.14 BM**	**μ_{eff} = 3.35 BM**

By comparing experimental and theoretical calculations of magnetic susceptibility in the table (3-1), the zinc ferrite spinal gave a value that is close to the calculations, because it is a natural spinal, and all Fe^{3+} sites are in an octahedral position, so it is paramagnetic. While in the ferrite nickel spinal, the practically measured value of μ_{eff} has decreased and the reason is because of it's a reverse spinal and Fe^{3+} sites are distributed between the octahedral and tetrahedral sites. As for the composite zinc-nickel ferrite, the decrease in the value of μ_{eff} is attributed to what was previously mentioned: that nickel is the base in this compound, and this control led to the withdrawal of $Fe^{3+}$from the octahedral sites to the tetrahedral sites [120].

3.2 Photocatalytic reaction of Alkali blue 4B dye

After determining the effectiveness of the prepared spinel $NiFe_2O_4$ $ZnFe_2O_4$ nanoparticles and their composite that depended on measuring the optical properties like band gap, these spinels were applied in photo-decolorization of Alkali blue 4B dye. And that is by taking several weights from the photo catalyst and knowing the ideal weight for the removal, then applying the specified weight over a range of temperatures to find the thermodynamics functions, and the initial pH was change for dye to determine its effect on the course of the reaction. All photoreaction experiments were applied at light intensity equal to (3.189×10^{-7} Enstine s^{-1}).

3.2.1 Effect of mass catalyst on dye solution

This effect is necessary to determine the cost-benefit amount before and after the modification of the photocatalyst surface.

The results listed in Tables (3-2) to (3-7) and plotted in figures from (3-12) to (3-14) show the apparent rate constant and efficiency of the reaction increase with increasing the dosage of photocatalyst, because the number of active sites on catalyst surface riase and will increase the interaction between the dye and hydroxyl radicals on the surface of the photocatalyst [113]**.**

The optimum mass of spinals $NiFe_2O_4$, $ZnFe_2O_4$ and Zn-$NiFe_2O_4$ composite are 0.025 g, 0.025 g and 0.015 g with PDE% 95.108, 97.3 and 100 respectively. Due to the screening effect, when the amount of photocatalysts is increased, the rate constant and the efficiency of the reaction go down. This is because the solution becomes more cloudy and less light can pass through it, that called screen effect[121].

A\ Effect of spinal $NiFe_2O_4$ mass

Table (3-2): The change of the Ln (Co/Ct) with irradiation time at the different mass of spinal $NiFe_2O_4$ via photocatalytic decolorization of Alkali blue 4B dye.

Mass (g) / Time (min)	$Ln(C_o/C_t)$			
	0.015	**0.025**	**0.035**	**0.05**
0	0	0	0	0
5	0.3295	0.2669	0.2568	0.2442
10	0.6461	0.5789	0.4814	0.4377
15	0.8002	1.4064	1.1235	0.5572
20	0.9203	2.4925	1.8119	0.6900
25	1.7732	2.6749	3.0414	2.3932
k_{app}/ min^{-1}	0.0697	**0.1054**	0.0983	0.0637

Table (3-3): The change of the PDE % with irradiation time at the different mass of spinal $NiFe_2O_4$ via photocatalytic decolorization of Alkali blue 4B dye.

Mass (g) / Time (min)	PDE %			
	0.015	**0.025**	**0.035**	**0.05**
0	0	0	0	0
5	28.0748	23.4303	22.65023	21.6718
10	47.5935	43.9514	38.21263	35.4489
15	55.0802	75.4977	67.48844	42.7244
20	60.1604	91.7304	83.66718	49.8452
25	83.0213	**95.1087**	93.2234	90.8668

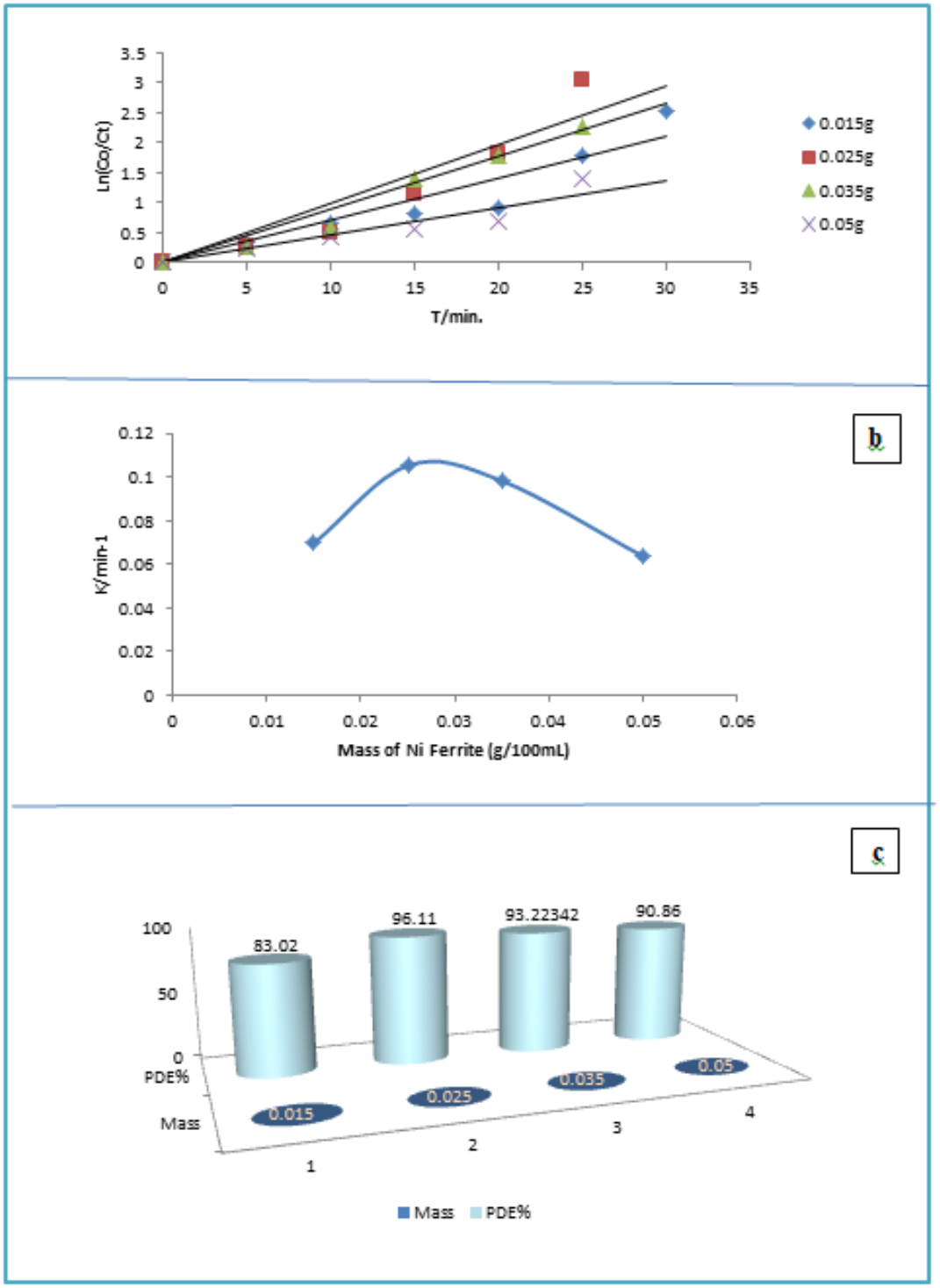

Figure (3-12). (a) The change of the Ln (C_o/Ct) with Irradiation time at a different mass of Ni Ferrite, (b) Relationship between (k app) apparent rate constant and a different mass Ni Ferrite, (c) Effect of a different mass of Ni Ferrite on (PDE%) photodecolorization efficiency.

B\ Effect of spinal $ZnFe_2O_4$ mass

Table (3-4): The change of the Ln (Co/Ct) with irradiation time at the different mass of spinal $ZnFe_2O_4$ via photocatalytic decolorization of Alkali blue 4B dye.

Mass (g) / Time (min)	Ln(C_o/C_t)			
	0.015	**0.025**	**0.035**	**0.05**
0	0	0	0	0
5	0.3152	0.7008	1.1221	0.0096
10	0.4418	1.8718	1.5639	0.0800
15	0.5202	2.1933	1.7263	0.1445
20	0.7563	2.3418	2.3261	0.3265
25	0.8898	2.7880	2.4927	0.6931
k_{app}/ min^{-1}	0.0496	**0.1231**	0.1054	0.0308

Table (3-5): The change of the PDE % with irradiation time at the different mass of spinal $ZnFe_2O_4$ via photocatalytic decolorization of Alkali blue 4B dye.

Mass (g) / Time (min)	PDE %			
	0.015	0.025	0.035	0.05
0	0	0	0	0
5	27.0408	50.3846	67.4418	0.96153
10	35.7142	84.6153	79.0697	7.69230
15	40.5612	88.8461	57.6744	13.4615
20	53.0612	90.3846	90.2325	29.8076
25	58.9285	93.8461	86.5116	50

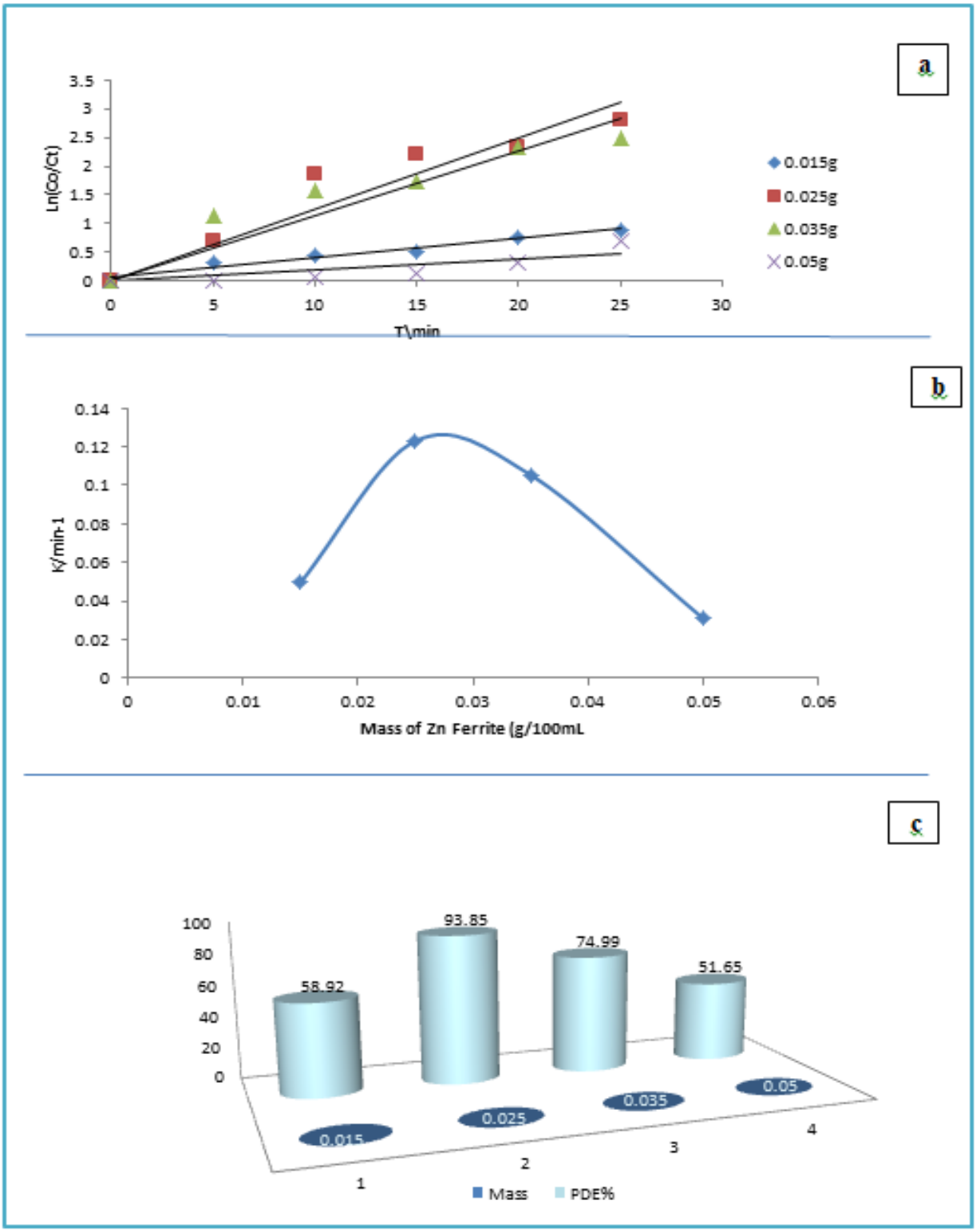

Figure (3-13). (a) The change of the Ln (C_o/Ct) with Irradiation time at a different mass of Zn Ferrite, (b) Relationship between (k app) apparent rate constant and a different mass Zn Ferrite, (c) Effect of a different mass of Zn Ferrite on (PDE%) photodecolorization efficiency.

C\ Effect of composite Zn-$NiFe_2O_4$ mass

Table (3-6): The change of the Ln (Co/Ct) with irradiation time at the different mass of composite Zn-$NiFe_2O_4$ via photocatalytic decolorization of Alkali blue 4B dye.

Mass (g) / Time (min)	Ln(C_o/C_t)			
	0.01	**0.015**	**0.02**	**0.025**
0	0	0	0	0
5	0.54426	0.29403	0.44043	0.26635
10	0.81432	0.5263	0.82642	0.38698
15	0.98535	1.02045	0.97302	0.479
20	1.07756	1.51635	1.12797	0.77071
25	1.38823	2.96636	1.51957	1.49664
k_{app}/ min^{-1}	0.0726	**0.092**	0.0739	0.0537

Table (3-7): The change of the PDE % with irradiation time at the different mass of composite Zn-$NiFe_2O_4$ via photocatalytic decolorization of Alkali blue 4B dye.

Mass (g) / Time (min)	PDE %			
	0.01	**0.015**	**0.02**	**0.025**
0	0	0	0	0
5	41.97292	25.47425	35.62387	23.38308
10	55.706	40.92141	56.2387	32.08955
15	62.66925	63.95664	62.20615	38.0597
20	65.95745	78.04878	67.6311	53.73134
25	75.04836	94.85095	78.11935	77.61194

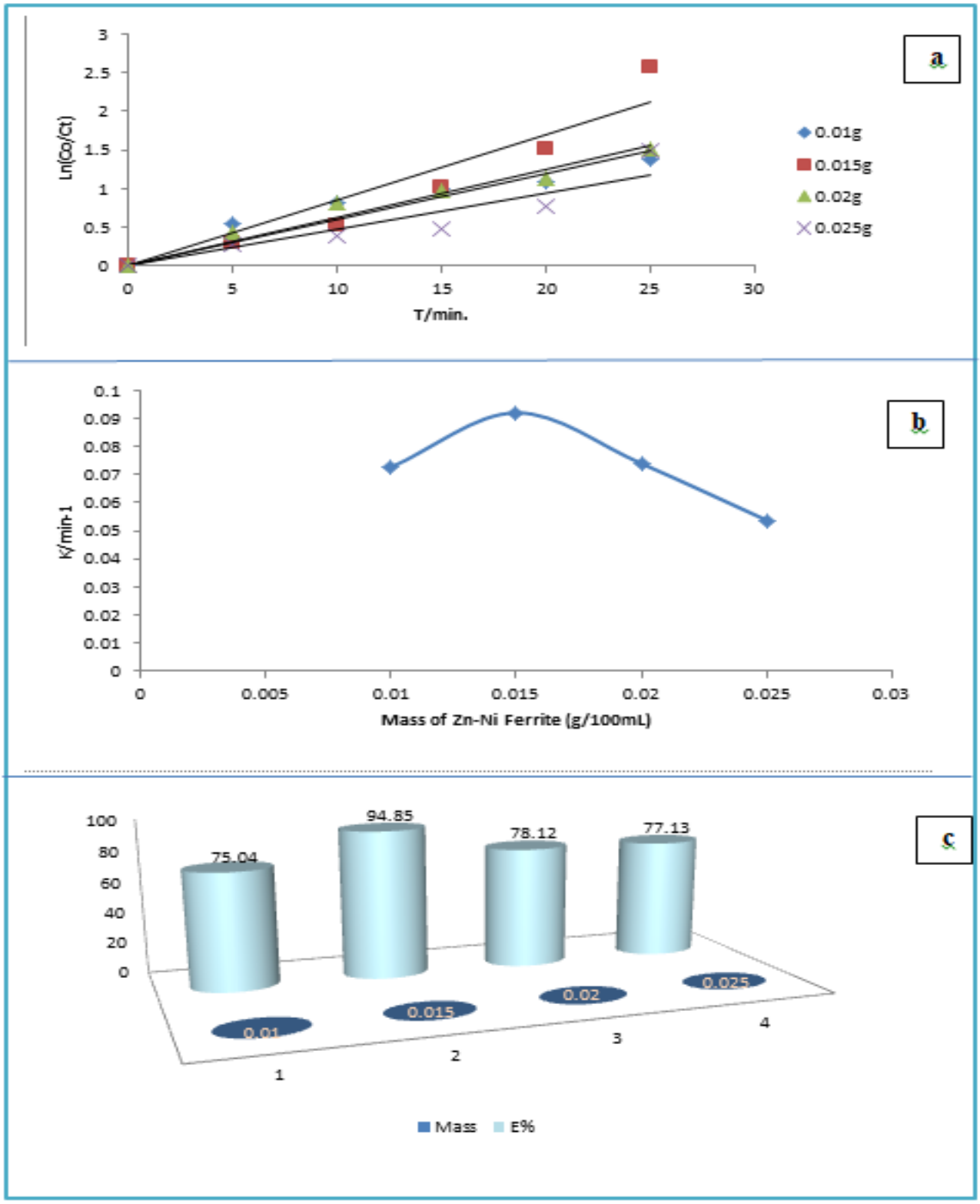

Figure (3-14). (a) The change of the Ln (C_o/Ct) with Irradiation time at a different mass of Zn-Ni Ferrite, (b) Relationship between (k app) apparent rate constant and a different mass Zn-Ni Ferrite, (c) Effect of a different mass of Zn-Ni Ferrite on (PDE%) photodecolorization efficiency.

3.2.2 Effect of Temperature

For the photocatalytic decolorization of Alkali blue 4B dye, a variety of temperature ranges (15 to 35 ^{o}C) were examined for their effects. An ice-filled water bath was used to keep temperatures within the desired range.

Table (3-7). Calculated activation energies and thermodynamic functions for decolorization of Alkali blue 4B dye with using spinal $NiFe_2O_4$, $ZnFe_2O_4$ and composite Zn-$NiFe_2O_4$.

Samples	Ea /kJ mol^{-1}	$\Delta H^{\#}$ /kJ mol^{-1}	$\Delta S^{\#}$ /k J mol^{-1} K^{-1}	$\Delta G^{\#}$ /kJ mol^{-1}
$NiFe_2O_4$	10.787	8.400	-0.240	79.920
$ZnFe_2O_4$	20.70	18.23	-0.205	79.32
Zn-$NiFe_2O_4$	23.969	21.49	-0.1961	79.928

The results expressed are listed in the table (3-7) to (3-13) and Figures from (3-15) to (3-20) explain that the increased of the temperature raised the photocatalytic decolorization of Alkali blue 4B dye. Where it can be seen that the removal rate decreased after a temperature of 25 ^{o}C because the reaction is endothermic that refer positive value of ($\Delta H^{\#}$). Apparently, the activation energies of nickel ferrite changed after combining with zinc ferrite to become 23.969 kJ mol^{-1} for composite. The change in enthalpies ($\Delta H^{\#}$) and change in Gibbs free energy ($\Delta G^{\#}$) are positive, which indicated to increase the solvated intermediate between dye and hydroxide radical $^{\cdot}$OH. The photoreactions for decolorized Alkali blue 4B dye with using the studied photocatalyst are endothermic, less random which that indicated an increase of randomness, while the reaction was non spontaneous, this results are same with the reported in references [122,123]. Moreover, the low values of activation energy ensure this photoreaction is fast, and the photoreaction with using $NiFe_2O_4$ is more fast than using the other prepared photocatalyst with psudo- first order kinetics.

A. Effect of temperature by Using spinal $NiFe_2O_4$

Table (3-8). The change of the Ln (Co/Ct) with irradiation time at different temperatures of spinal $NiFe_2O_4$ via photocatalytic decolorization of Alkali blue 4B dye.

T °C / Time (min)	Ln(C_0/C_t)			
	15	**20**	**25**	**35**
0	0	0	0	0
5	0.21097	0.25236	0.26697	0.22739
10	0.53366	0.54192	0.57894	0.8067
15	0.66474	1.07984	1.4064	1.23457
20	0.80913	1.41889	2.49259	1.60662
25	0.9934	1.98758	2.67491	2.16125
k_{app}/ min^{-1}	0.0439	0.07	**0.1054**	0.061

Table (3-9). The change of the (PDE %) with irradiation time at different temperatures of spinal $NiFe_2O_4$ via photocatalytic decolorization of Alkali blue 4B dye.

T °C / Time (min)	PDE %			
	15	**20**	**25**	**35**
0	0	0	0	0
5	19.02017	22.30321	23.43032	20.33898
10	41.35447	41.83673	43.95134	55.36723
15	48.55908	66.03499	75.49775	70.90395
20	55.4755	75.80175	91.73047	79.9435
25	62.9683	86.29738	95.10873	85.76271
30	71.61383	87.31778	**100**	93.54121

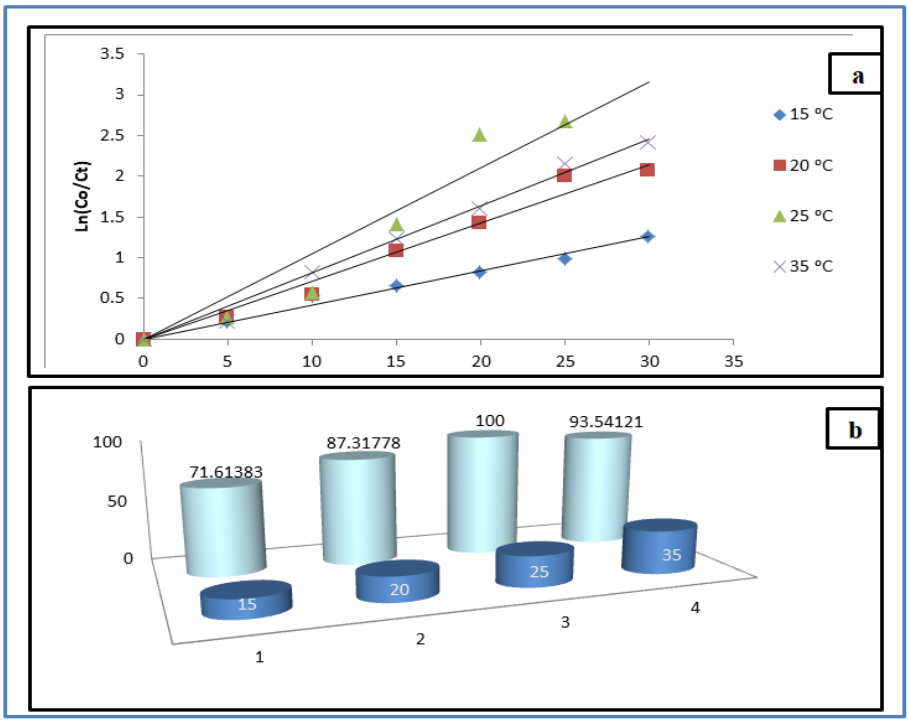

Figure (3-15). (a) The change of the Ln (Co/Ct) with Irradiation time at different temperatures of spinal Ni Ferrite, (b) Effect of the different temperature of spinal Ni Ferrite on (PDE%) photodecolorization efficiency.

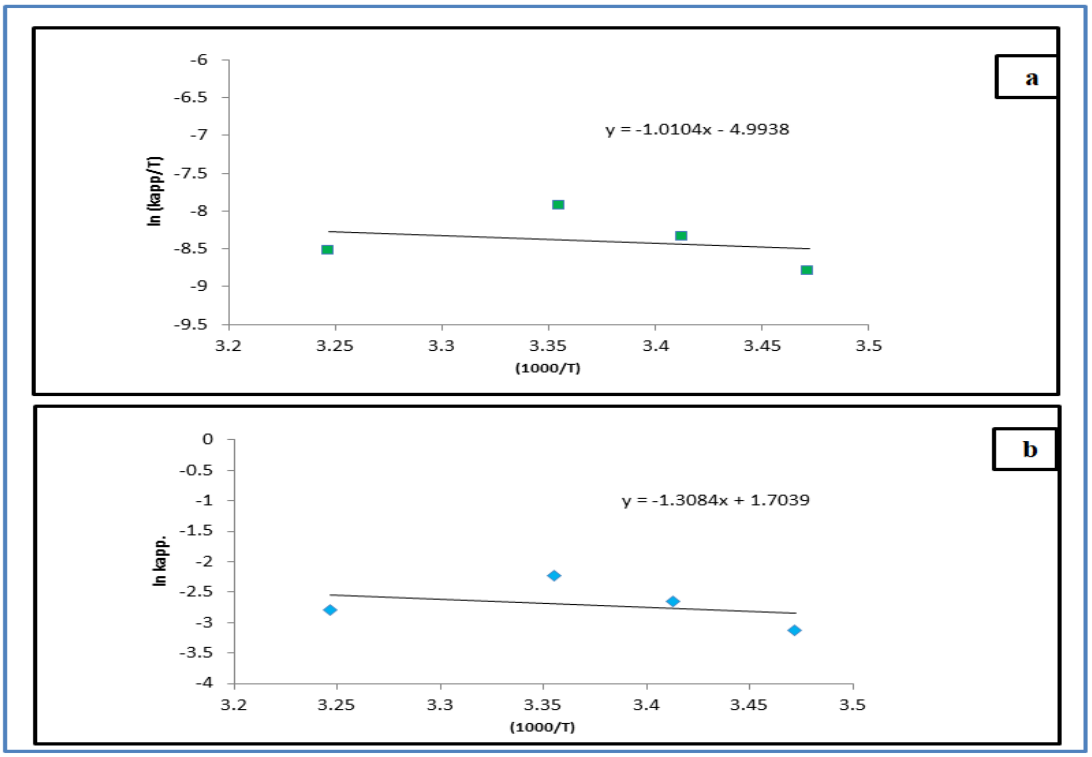

Figure (3-16). (a) Eyring–Polanyi equation plot ln (k app/T) VS. 1000/T (b) Arrhenius equation plot by spinal Ni Ferrite via photocatalytic decolorization of Alkali blue 4B dye

B. Effect of temperature by Using spinal $ZnFe_2O_4$

Table (3-10). The change of the Ln (Co/Ct) with irradiation time at different temperatures of spinal $ZnFe_2O_4$ via photocatalytic decolorization of Alkali blue 4B dye.

T ºC / Time (min)	Ln(C_0/C_t)			
	15	**20**	**25**	**35**
0	0	0	0	0
5	0.28292	0.24784	0.70087	0.47682
10	0.49613	0.48722	1.8718	0.81272
15	0.71927	0.76913	2.19339	1.06346
20	0.86124	0.99722	2.34181	1.24392
25	0.95723	1.18286	2.78809	1.70118
k_{app}/ min^{-1}	0.0331	0.0487	**0.1231**	0.0708

Table (3-11). The change of the (PDE %) with irradiation time at different temperatures of spinal $ZnFe_2O_4$ via photocatalytic decolorization of Alkali blue 4B dye.

T ºC / Time (min)	PDE %			
	15	**20**	**25**	**35**
0	0	0	0	0
5	24.64183	21.95122	50.38462	37.92487
10	39.11175	38.56707	84.61539	55.63506
15	51.2894	53.65854	88.84615	65.47406
20	57.73639	63.10976	90.38462	71.73524
25	61.60458	69.35976	**94.84615**	81.75313

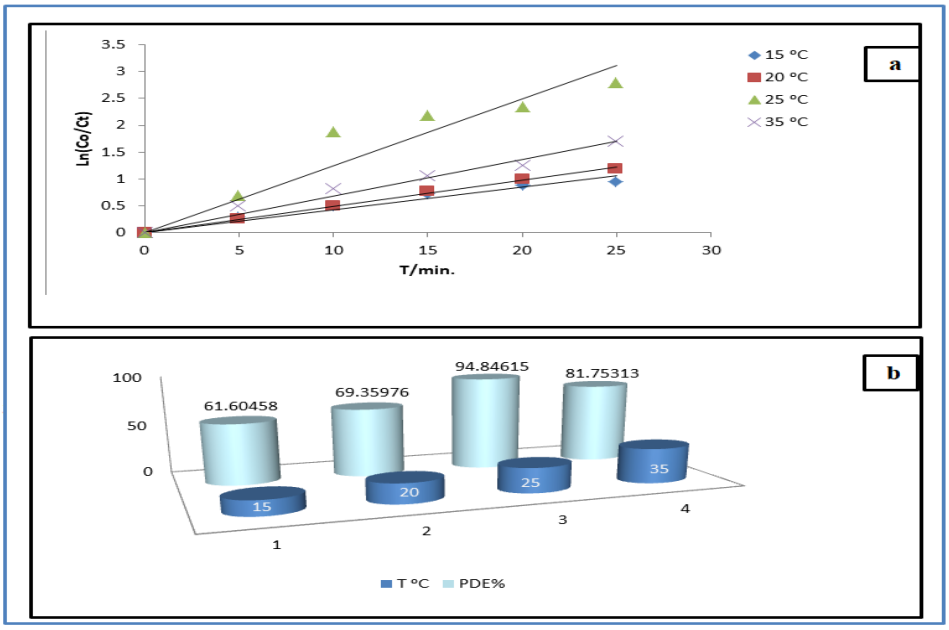

Figure (3-17). (a) The change of the Ln (Co/Ct) with Irradiation time at different temperatures of spinal Zn Ferrite, (b) Effect of the different temperature of spinal Zn Ferrite on (PDE%) photodecolorization efficiency.

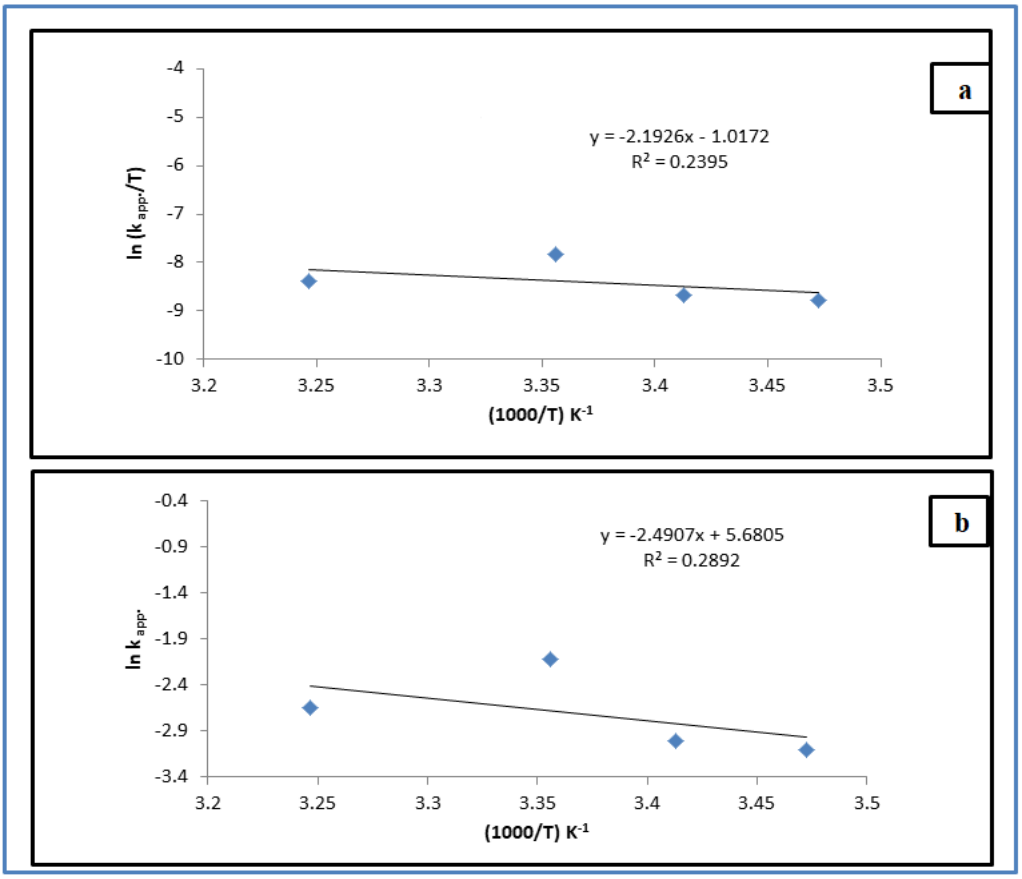

Figure (3-18). (a) Eyring–Polanyi equation plot ln (k app/T) VS. 1000/T (b) Arrhenius equation plot by spinal Zn Ferrite via photocatalytic decolorization of Alkali blue 4B dye.

C. Effect of temperature by Using composite Zn-$NiFe_2O_4$

Table (3-12). The change of the Ln (Co/Ct) with irradiation time at different temperatures of composite Zn-$NiFe_2O_4$ via photocatalytic decolorization of Alkali blue 4B dye.

T °C / Time (min)	Ln(C_o/C_t)			
	15	**20**	**25**	**35**
0	0	0	0	0
5	0.268792	0.23348	0.294026	0.25309063
10	0.459532	0.478782	0.526302	0.57054486
15	0.611873	0.851592	1.020448	0.71195651
20	0.843491	1.227381	1.516347	0.95426998
25	1.275912	2.012336	2.526358	1.49788543
k_{app}/ min^{-1}	0.036	0.051	**0.092**	0.067

Table (3-13). The change of the (PDE %) with irradiation time at different temperatures of composite Zn-$NiFe_2O_4$ via photocatalytic decolorization of Alkali blue 4B dye.

T °C / Time (min)	PDE %			
	15	**20**	**25**	**35**
0	0	0	0	0
5	23.56979	20.82262	25.47425	22.36025
10	36.84211	38.04627	40.92141	43.47826
15	45.76659	57.32648	63.95664	50.93168
20	56.97941	70.69409	78.04878	61.49068
25	72.08238	86.63239	94.85095	77.63975

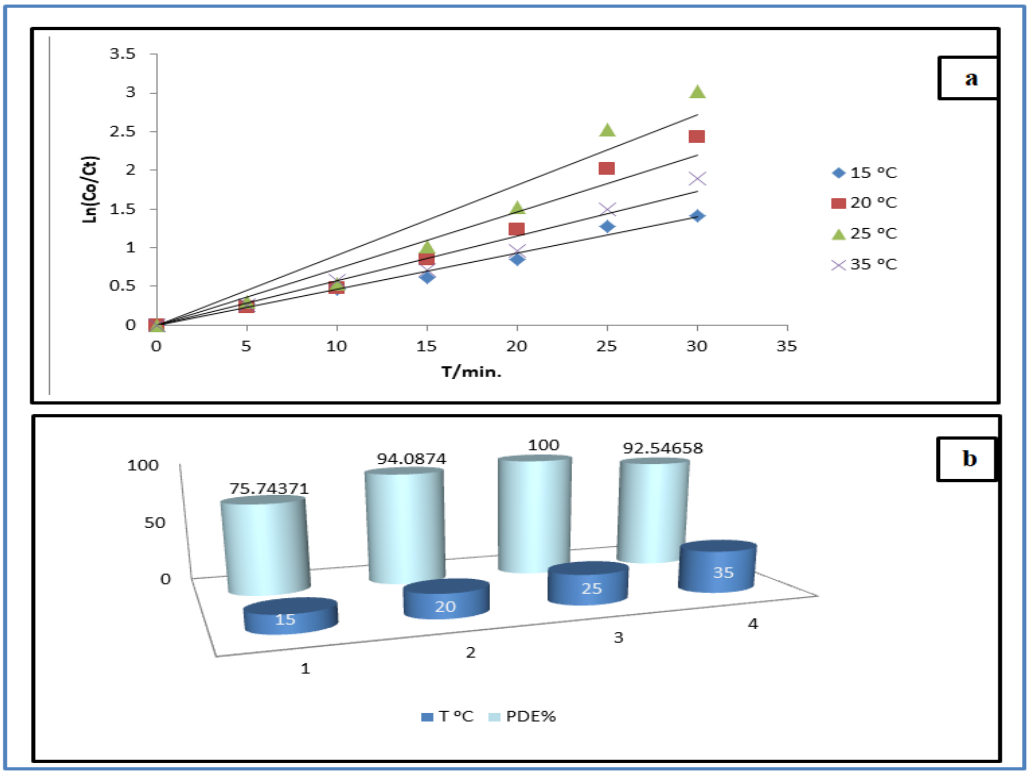

Figure (3-19). (a) The change of the Ln (Co/Ct) with Irradiation time at different temperatures of composite Zn-Ni Ferrite, (b) Effect of the different temperature of composite Zn-Ni Ferrite on (PDE%) photodecolorization efficiency.

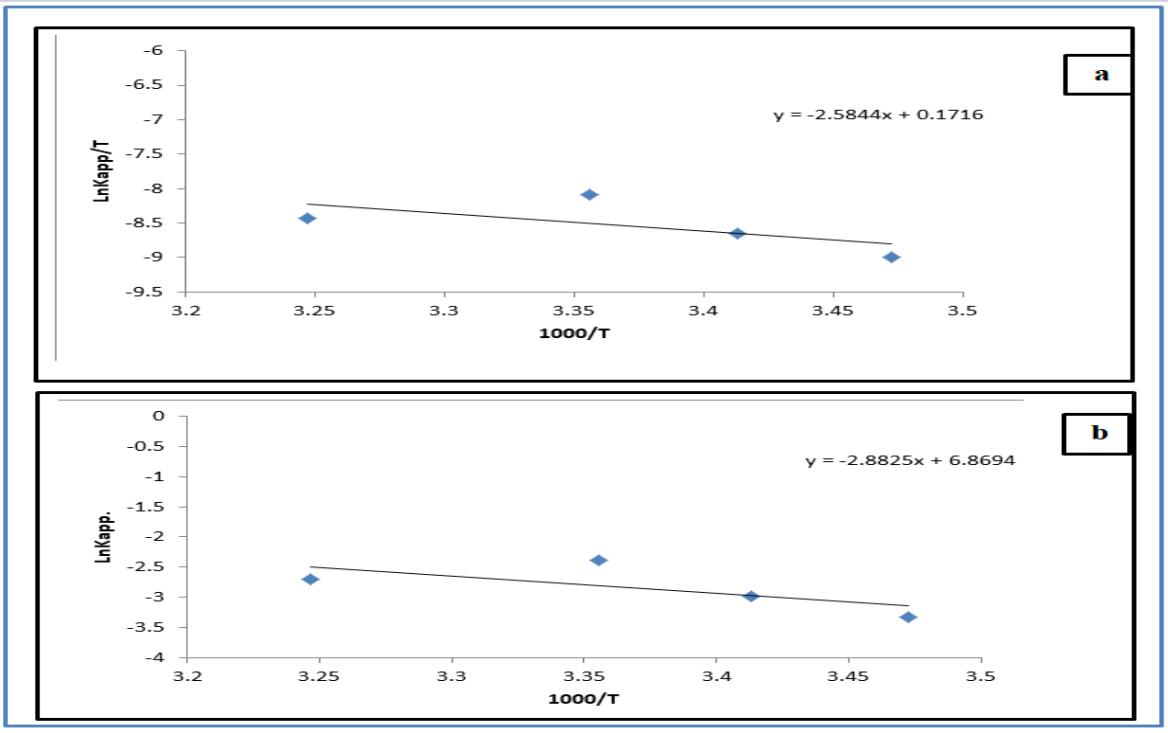

Figure (3-20). (a) Eyring–Polanyi equation plot ln (k app/T) VS. 1000/T (b) Arrhenius equation plot by composite Zn-Ni Ferrite via photocatalytic decolorization of Alkali blue 4B dye.

3.2.3 Effect of initial pH of the solution on dye decolorization.

The influence of initial pH was studied using a pH range of 2.5 to 7 and under the following conditions: 25 ppm dye concentration in 100 mL, 298 K, masses of spinal $NiFe_2O_4$, $ZnFe_2O_4$ and Zn-$NiFe_2O_4$ nanocomposites was 0.025 g ,0.025g and 0.015g, respectively, and the same light intensity.

In the results top mention in tables (3-14) to (3-19) and figures from (3-21) to (3-23), show that the efficiency and the rate constant of these photo reactions increased with increasing the initial pH of alkali blue 4B dye, which was found to be 2.5. That is due to the increase in an attractive force between the dye molecule and catalyst surface because of the dye's acidic nature. Moreover, the percentage of hydroxyl radicals is also increased in the solution; these causes lead to enhanced photocatalytic activity in the decolorization process [124,125].The pH value was not performed with an increase of more than 7 because of the change in color of the dye solution, which referred to the change in dye structure.

A. Effect of initial pH of Alkali blue 4B dye solution by spinal $NiFe_2O_4$.

Table (3-14). The change of the Ln (Co/Ct) with irradiation time at different initial pH of Alkali blue 4B dye by $NiFe_2O_4$.

pH / Time (min)	Ln(C_o/C_t)			
	2.5	**4**	**5.5**	**7**
0	0	0	0	0
5	0.26697	0.279005	0.222038	0.362766
10	0.57894	0.632907	0.311564	0.655821
15	1.4064	1.467972	1.150838	1.014962
20	2.49259	1.707202	2.530163	1.507439
25	2.67491	3.851783	4.034241	5.409411
k_{app}/ min^{-1}	0.1054	0.1165	0.1258	**0.1374**

Table (3-15). The change of the (PDE %) with irradiation time at different initial pH of Alkali blue 4B dye by $NiFe_2O_4$.

Time (min) \ pH	PDE %			
	2.5	**4**	**5.5**	**7**
0	0	0	0	0
5	23.43032	24.34641	19.9115	30.42506
10	43.95143	46.89542	26.76991	48.09843
15	75.49775	76.96078	68.36283	63.75839
20	91.73047	81.86275	92.0354	77.85235
25	95.10873	97.87582	98.23009	**99.55257**

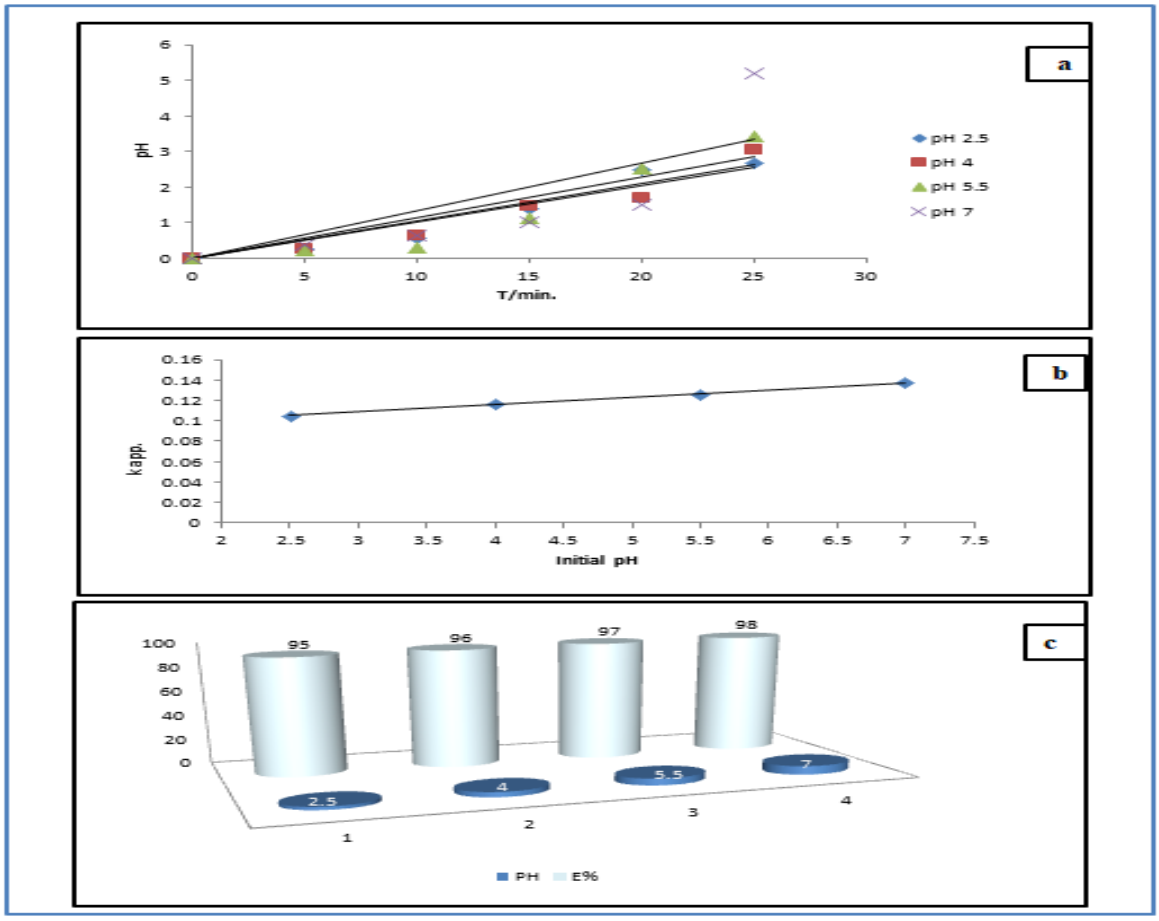

Figure (3-21). (a) The change of the Ln (C_o/Ct) with Irradiation time at a different pH solution of spinal $NiFe_2O_4$, (b) Relationship between the (k app) apparent rate constant and the different pH solution of spinal $NiFe_2O_4$, (c) Effect the different pH solution of spinal $NiFe_2O_4$ on (PDE%) photodecolorization efficiency.

B. Effect of initial pH of Alkali blue 4B dye solution by spinal $ZnFe_2O_4$

Table (3-16). The change of the Ln (Co/Ct) with irradiation time at different initial pH of Alkali blue 4B dye by $ZnFe_2O_4$.

pH / Time (min)	Ln(C_o/C_t)			
	2.5	**4**	**5.5**	**7**
0	0	0	0	0
5	0.7008	0.2769	0.5661	0.1367
10	1.8718	0.4808	0.9793	0.5465
15	2.1933	0.8690	1.7701	1.8458
20	2.3418	2.3925	3.2364	3.7917
25	2.7880	3.1463	4.04742	-
k_{app}/ min^{-1}	0.1231	0.133	0.139	**0.146**

Table (3-17). The change of the (PDE %) with irradiation time at different initial pH of Alkali blue 4B dye by $ZnFe_2O_4$.

pH / Time (min)	PDE %			
	2.5	**4**	**5.5**	**7**
0	0	0	0	0
5	50.3846	24.1935	43.2314	12.7819
10	84.6153	38.1720	62.4454	42.1052
15	88.8461	58.0645	82.9694	84.2105
20	90.3846	90.8602	96.0698	97.7443
25	94.8461	95.6989	98.2532	**100**

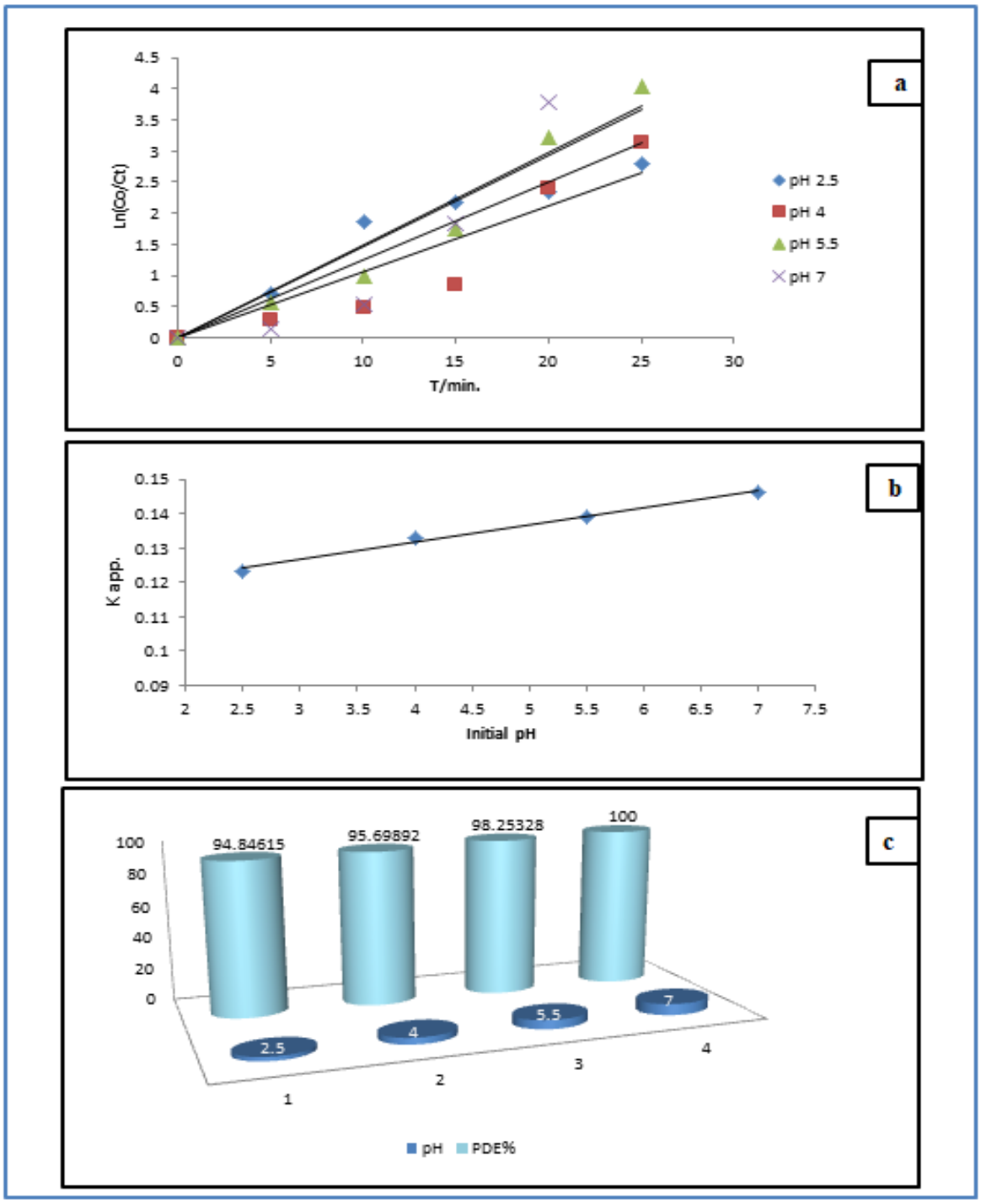

Figure (3-22). (a) The change of the Ln (C_o/Ct) with Irradiation time at a different pH solution of spinal $ZnFe_2O_4$, (b) Relationship between the (k app) apparent rate constant and the different pH solution of spinal $ZnFe_2O_4$, (c) Effect the different pH solution of spinal $ZnFe_2O_4$ on (PDE%) photodecolorization efficiency.

C. Effect of initial pH of Alkali blue 4B dye solution by composite Zn-$NiFe_2O_4$

Table (3-18). The change of the Ln (Co/Ct) with irradiation time at different initial pH of Alkali blue 4B dye by Zn-$NiFe_2O_4$.

pH / Time (min)	$Ln(C_o/C_t)$			
	2.5	**4**	**5.5**	**7**
0	0	0	0	0
5	0.2940	0.0855	0.3051	0.24487
10	0.5263	0.3356	0.67385	0.78304
15	1.0204	0.5615	1.00271	1.56952
20	1.5163	1.1143	1.83827	3.31872
25	2.96635	3.1472	3.65065	-
k_{app}/ min^{-1}	0.092	0.102	0.110	**0.132**

Table (3-19). The change of the (PDE %) with irradiation time at different initial pH of Alkali blue 4B dye by Zn-$NiFe_2O_4$.

pH / Time (min)	PDE %			
	2.5	**4**	**5.5**	**7**
0	0	0	0	0
5	25.4742	8.2031	26.2987	21.7194
10	40.9214	28.5156	49.0259	54.2986
15	63.9566	42.9687	63.3116	79.1855
20	78.0487	67.1875	84.0909	96.3800
25	94.8509	95.7031	97.4026	**100**

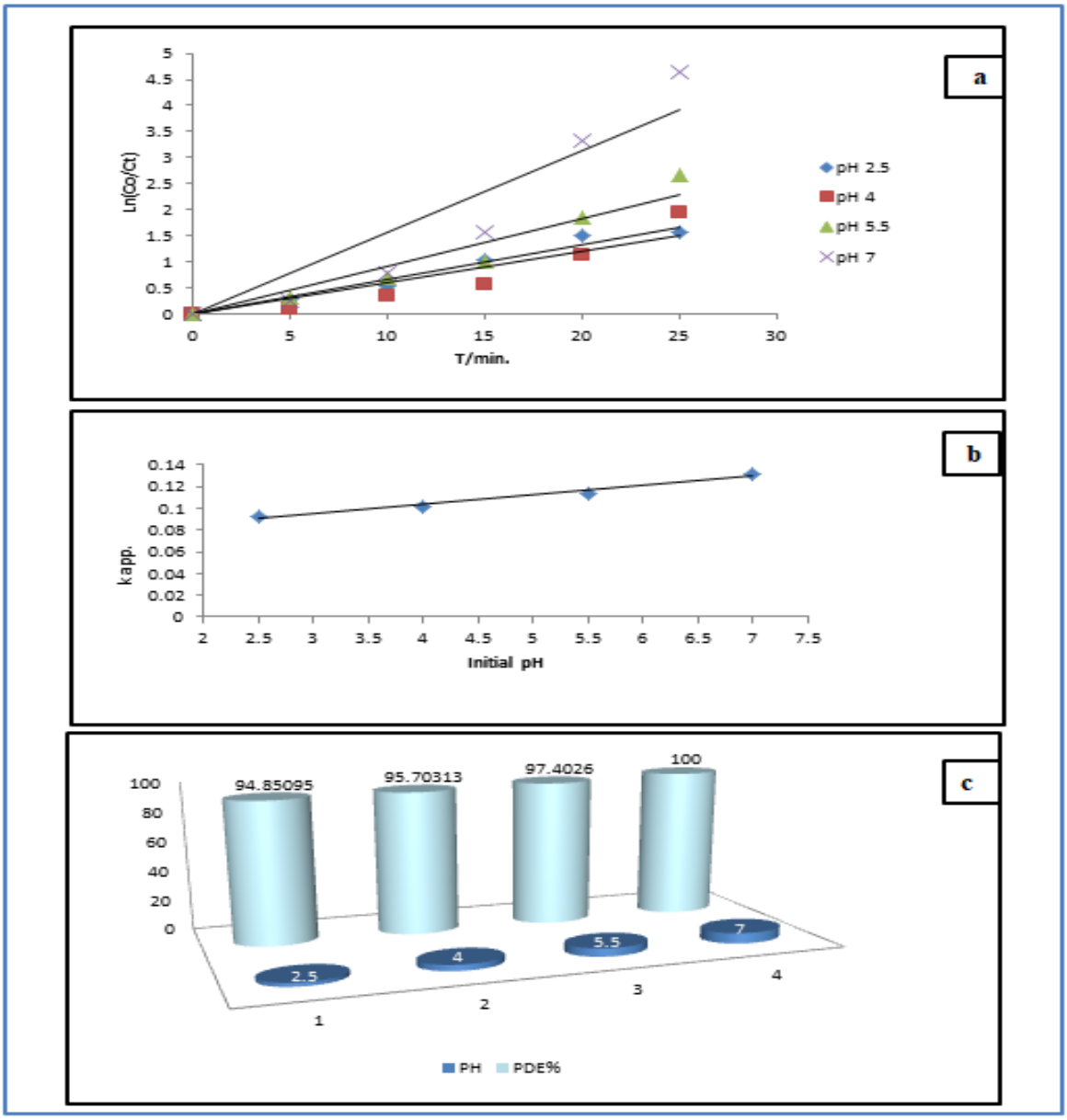

Figure (3-23). (a) The change of the Ln (C_o/Ct) with Irradiation time at a different pH solution of composite Zn-$NiFe_2O_4$, (b) Relationship between the (k app) apparent rate constant and the different pH solution of composite Zn-$NiFe_2O_4$, (c) Effect the different pH solution of composite Zn-$NiFe_2O_4$ on (PDE%) photodecolorization efficiency.

3.3 Hemolysis assay

Nanoparticle-induced hemolysis is one of the fundamental tests employed to study the biocompatibility of designed nanocarriers. The hemolysis induced for 60 healthy nonsmoker donors by using zinc ferrite ($ZnFe_2O_4$), nickel ferrite ($NiFe_2O_4$) nanoparticles, and (nickel-zinc ferrite, Ni- $ZnFe_2O_4$) nanocomposite at different concentrations (0.025, 0.025, 0.015 $g \cdot ml^{-1}$). The resulets in figure (3-27) and in tables (3-20), (3-21), (3-22) are showed the hemolysis persenteges (12.23%, 13.15%, 2.59%). Triton X-100 Positive Control was selected with a hemolysis of 100%, and Normal Saline Active Control was selected with a hemolysis of 1.3%. Although the percentage of hemolysis using samples prepared from zinc ferrite, nickel ferrite and their composite are relatively low, it cannot be considered safe as the permissible percentage of safe percentage is 2% according to ISO 10993-4:2018 for hemolysis by biomaterials in contact with blood[126]. This indicates that these materials are not suitable for using at the human body within these concentrations.

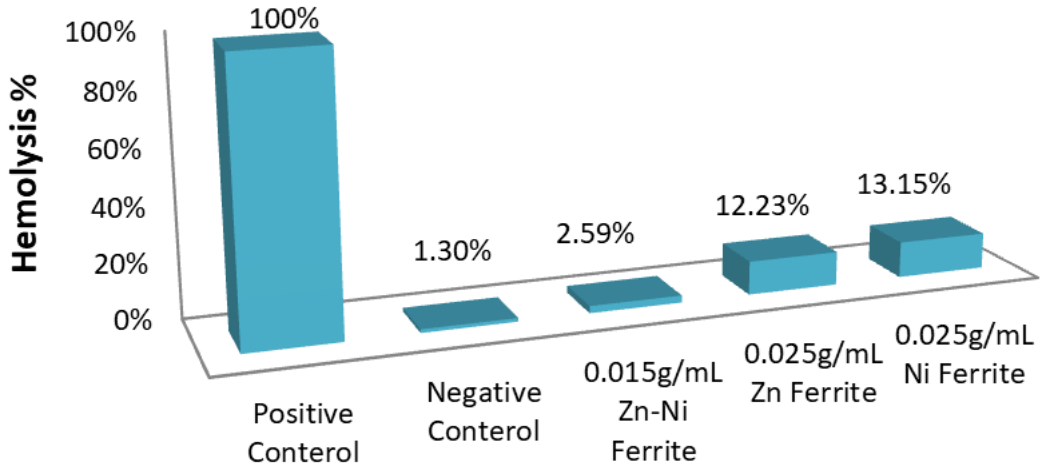

Figure (3-24). The percentage of hemolysis induced by zinc ferrite, Nickel ferrite and zinc-Nickel ferrit. Triton X-100 was used as a positive control and normal saline as a negative contro

Table (3-20). The percentage of hemolysis induced by zinc ferrite, and absorbance for blood with $ZnFe_2O_4$, with normal saline, 100% Hemolysis with positive control and with D.W.

Abs with $ZnFe_2O_4$	Abs with normal saline	Abs with D.W.	Hemolysis %
0.117	0.032	0.365	34.27419
0.119	0.051	0.524	16.79012
0.125	0.055	0.51	18.18182
0.131	0.066	0.556	15.29412
0.133	0.075	0.575	13.12217
0.138	0.092	0.528	11.79487
0.143	0.101	0.636	8.51927
0.143	0.116	0.639	5.443548
0.144	0.111	0.651	6.508876
0.147	0.091	0.669	10.72797
0.149	0.122	0.636	5.544148
0.169	0.125	0.856	6.404658
0.117	0.022	0.315	34.27419
0.119	0.055	0.724	16.79012
0.047	0.057	0.501	4.504505
0.056	0.061	0.454	1.057082
0.057	0.065	0.371	0.43956
0.075	0.082	0.566	1.836735
0.085	0.111	0.642	2
0.115	0.126	0.641	5.275229
0.117	0.121	0.681	2.990654
0.119	0.031	0.717	0.573614
0.126	0.022	0.636	2.777778
0.126	0.152	0.756	6.055363
0.134	0.042	0.465	2.33463
0.137	0.081	0.324	1.641587
0.047	0.045	0.451	4.504505
0.056	0.076	0.656	1.057082
0.077	0.045	0.787	13.51351
0.081	0.052	0.468	6.342495
0.097	0.091	0.636	9.230769
0.125	0.106	0.652	12.04082
0.13	0.071	0.611	11
0.133	0.041	0.539	9.40367
0.139	0.082	0.716	7.102804
0.142	0.125	0.856	4.971319
0.058	0.112	0.495	7.807808
0.072	0.071	0.524	4.439746
0.078	0.095	0.651	5.054945
0.095	0.076	0.446	5.918367
0.104	0.035	0.675	5.8

0.106	0.072	0.428	3.211009
0.122	0.161	0.736	3.925234
0.128	0.056	0.642	2.294455
0.13	0.111	0.451	3.518519
0.157	0.091	0.621	11.41869
0.175	0.102	0.536	10.31128
0.21	0.065	0.751	11.62791
0.086	0.032	0.856	16.21622
0.102	0.101	0.441	10.78224
0.133	0.115	0.224	17.14286
0.146	0.106	0.660	16.32653
0.16	0.085	0.532	17
0.167	0.062	0.712	17.20183
0.153	0.101	0.528	9.719626
0.16	0.103	0.717	8.413002
0.167	0.117	0.801	10.37037
0.174	0.091	0.398	14.35986
0.184	0.120	0.801	12.06226

Table (3-21). The percentage of hemolysis induced by zinc ferrite, and absorbance for blood with $NiFe_2O_4$, with normal saline, 100% Hemolysis with positive control and with D.W.

Abs with $NiFe_2O_4$	Abs with normal saline	Abs with D.W.	Hemolysis %
0.086	0.032	0.365	15.21622
0.102	0.051	0.524	11.78224
0.133	0.055	0.51	16.14286
0.146	0.066	0.556	13.32653
0.16	0.075	0.575	18.84263
0.167	0.092	0.528	12.20183
0.153	0.101	0.636	8.719626
0.16	0.116	0.639	7.413002
0.167	0.111	0.651	11.37037
0.174	0.091	0.669	15.35986
0.184	0.122	0.636	13.06226
0.13	0.125	0.856	11.87193
0.133	0.022	0.315	8.40367
0.139	0.055	0.724	9.102804
0.142	0.057	0.501	5.971319
0.146	0.061	0.454	6.481481
0.155	0.065	0.371	12.07266

0.174	0.082	0.566	11.11673
0.193	0.111	0.642	9.302326
0.077	0.126	0.641	11.51351
0.081	0.121	0.681	7.342495
0.097	0.031	0.717	9.230769
0.125	0.022	0.636	11.04082
0.095	0.152	0.756	5.918367
0.104	0.042	0.465	6.197252
0.106	0.081	0.324	3.211009
0.122	0.045	0.451	3.925234
0.128	0.076	0.656	2.294455
0.13	0.045	0.787	3.518519
0.157	0.052	0.468	11.41869
0.175	0.091	0.636	10.31128
0.21	0.106	0.652	11.62791
0.058	0.071	0.611	7.807808
0.072	0.041	0.539	4.439746
0.078	0.082	0.716	5.054945
0.115	0.125	0.856	5.275229
0.117	0.112	0.495	2.990654
0.119	0.071	0.524	0.573614
0.126	0.095	0.651	2.162778
0.126	0.076	0.446	6.055363
0.134	0.035	0.675	2.33463
0.137	0.072	0.428	1.641587
0.047	0.161	0.736	4.504505
0.056	0.056	0.642	1.057082
0.057	0.111	0.451	0.43956
0.075	0.091	0.621	1.836735
0.085	0.102	0.536	1.976918
0.119	0.065	0.751	16.79012
0.125	0.032	0.856	18.18182
0.131	0.101	0.441	15.29412
0.133	0.115	0.224	13.12217
0.138	0.106	0.660	11.79487
0.143	0.085	0.532	8.51927
0.143	0.062	0.712	5.443548
0.144	0.101	0.528	6.508876
0.147	0.103	0.717	10.72797
0.149	0.117	0.801	5.544148
0.169	0.091	0.398	6.404658
0.117	0.120	0.801	7.142187

Table (3-22). The percentage of hemolysis induced by zinc ferrite, and absorbance for blood with Zn-Ni Fe_2O_4, with normal saline, 100% Hemolysis with positive control and with D.W.

Abs with Zn-NiFe_2O_4	Abs with normal saline	Abs with D.W.	Hemolysis %
0.047	0.032	0.365	4.504505
0.056	0.051	0.524	1.057082
0.057	0.055	0.51	0.43956
0.075	0.066	0.556	1.836735
0.085	0.075	0.575	2
0.115	0.092	0.528	5.275229
0.117	0.101	0.636	2.990654
0.119	0.116	0.639	0.573614
0.126	0.111	0.651	2.777778
0.126	0.091	0.669	6.055363
0.134	0.122	0.636	2.33463
0.137	0.125	0.856	1.641587
0.081	0.022	0.315	6.342495
0.097	0.055	0.724	9.230769
0.125	0.057	0.501	12.04082
0.13	0.061	0.454	8.554416
0.133	0.065	0.371	11.40367
0.139	0.082	0.566	7.102804
0.142	0.111	0.642	4.971319
0.146	0.126	0.641	6.481481
0.155	0.121	0.681	11.07266
0.174	0.031	0.717	10.11673
0.193	0.022	0.636	9.302326
0.077	0.152	0.756	13.51351
0.21	0.042	0.465	10.62791
0.058	0.081	0.324	8.807808
0.072	0.045	0.451	5.439746
0.078	0.076	0.656	4.054945
0.095	0.045	0.787	5.918367
0.104	0.052	0.468	6.676541
0.106	0.091	0.636	9.211009
0.122	0.106	0.652	7.925234
0.128	0.071	0.611	2.294455
0.13	0.041	0.539	3.518519
0.157	0.082	0.716	12.41869
0.175	0.125	0.856	9.31128
0.174	0.112	0.495	1.35986
0.114	0.071	0.524	7.06226
0.111	0.095	0.651	8.071135
0.076	0.076	0.446	3.21622
0.091	0.035	0.675	5.78224

0.133	0.072	0.428	9.14286
0.126	0.161	0.736	4.32653
0.106	0.056	0.642	1.71213
0.117	0.111	0.451	7.20183
0.123	0.091	0.621	9.719626
0.136	0.102	0.536	8.413002
0.107	0.065	0.751	5.37037
0.123	0.032	0.856	6.055363
0.104	0.101	0.441	2.33463
0.137	0.115	0.224	1.641587
0.097	0.106	0.660	4.504505
0.046	0.085	0.532	1.057082
0.077	0.062	0.712	1.43956
0.055	0.101	0.528	1.836735
0.085	0.103	0.717	2.298751
0.105	0.117	0.801	5.275229
0.108	0.091	0.398	2.990654
0.110	0.120	0.801	1.573614

3.4 Conclusions

The main conclusions from this work can be summarized with:

1. Preparation of the inverse spinel $NiFe_2O_4$ and normal spinel $ZnFe_2O_4$ as nanoparticle like- broccoli and nanoparticle like cauliflower using precipitation route assisted with solvo-thermal route in the presence of ethanol.
2. Using non-polar surfactant (Hexamine) as capping agent in precipitation method, and used as template.
3. The Zn-$NiFe_2O_4$ nano-composite like- broccoli was successfully synthesized using ultrasonic technique in aqueous solutions.
4. Based on the FT-IR spectra, the positions of the octahedral (as a highest-frequency band ν1) and the positions of the tetrahedral site(as a lowest-frequency band ν2) were determined. The kinds of prepared spinel were also proved as inverse spinel $NiFe_2O_4$, normal spinel $ZnFe_2O_4$ and inverse spinel Zn-$NiFe_2O_4$ nano-composite.
5. The XRD analysis proved all the prepared spinel and their composite are nanomaterial. In addition, the spinal zinc ferrite suffer from a lower angles towards the spinal nickel ferrite sites, which means that formed a metal bond between Zn and Ni and Zn-$NiFe_2O_4$ produced.
6. SEM analysis detected the morphology of the studied photocatalysts and found all samples to be of spherical agglomerated. The particle sizes for all studied photocatalysts are larger than the crystal sizes. Hence, these samples are regarded as poly-crystals.
7. By plotting Tauc equation, the band gaps of Nickel ferrite, Zinc ferrite and their composites are found to be low and indirect band gaps, hence they can be concluded that all the prepared (spaniels and their composite) are photocatalysts.

8. The photoactivity of Nickel ferrite, Zinc ferrite and their composites was done with small doses 0.025g, 0.025 g and 0.015 g in 100 mL of alkali blue 4B dye solution at 25 ^{o}C with pH=7. The photoreaction is obeyed pseudo-first order kinetic with low activation energy and endothermic reaction.
9. Although the percentage of hemolysis values calculated using nickel ferrite, zinc ferrite, and its composite are low, and it is not recommended to use these concentrations.

3.6 Future Works

1. Altering the time, temperature and solvent when preparing the spinel using the autoclaving step.

2. Using various types of surfactants can be positive, negative and non-polar during preparing of spinal to controlling on the shape and size of its crystal.

3. Preperation of different metal ferrite nanostructures using other metals such as Co and Cu.

4. Investigating by use these catalysts in photo-degradation or removal (dark reaction) of different type of dyes.

5. Application these catalysts in a solar cell.

6. Application these catalysts as a sensor.

7. Using of different weights from prepared materials, and testing them in the percentage of hemolysis.

References

[1] J.E. Hulla, S.C. Sahu, A.W. Hayes, "Nanotechnology: History and future," *Hum.Exp.Toxico*l.34(2015)1318–1321. doi.org/10.1177/0960327115603588.

[2] I. Khan, K. Saeed, and I. Khan, "Nanoparticles: Properties, applications and toxicities," *Arab. J. Chem.*, vol. 12, no. 7, pp. 908–931, 2019, doi: 10.1016/j.arabjc.2017.05.011.

[3] A. Gnach, T. Lipinski, A. Bednarkiewicz, J. Rybka, and J. A. Capobianco, "Upconverting nanoparticles: Assessing the toxicity," *Chem. Soc. Rev.*, vol. 44, no. 6, pp. 1561–1584, 2015, doi: 10.1039/c4cs00177j.

[4] S. Bayda, M. Adeel, T. Tuccinardi, M. Cordani, and F. Rizzolio, "The history of nanoscience and nanotechnology: From chemical-physical applications to nanomedicine," *Molecules*, vol. 25, no. 1, pp. 1–15, 2020, doi: 10.3390/molecules25010112.

[5] N. Baig, I. Kammakakam, W. Falath, and I. Kammakakam, "Nanomaterials: A review of synthesis methods, properties, recent progress, and challenges," *Mater. Adv.*, vol. 2, no. 6, pp. 1821–1871, 2021, doi: 10.1039/d0ma00807a..

[6] P. Iqbal, J. A. Preece, and P. M. Mendes, "Nanotechnology: The 'Top-Down' and 'Bottom-Up' Approaches," Supramol. Chem., 2012, doi: 10.1002/9780470661345.smc195.

[7] G. Mogilevsky, O. Hartman, E.D. Emmons, A. Balboa, J.B. Decoste, B.J. Schindler, I. Iordanov, C.J. Karwacki., "Bottom-up synthesis of anatase nanoparticles with graphene domains," *ACS Appl. Mater. Interfaces*, vol. 6, no. 13, pp. 10638–10648, 2014, doi: 10.1021/am502322y.

[8] I. E. Wachs and K. Routray, "Catalysis science of bulk mixed oxides," *ACS Catal.*, vol. 2, no. 6, pp. 1235–1246, 2012, doi: 10.1021/cs2005482.

[9] Y. Xia, Y. Xiong, B. Lim, and S. E. Skrabalak, "Shape-controlled synthesis of metal nanocrystals: Simple chemistry meets complex physics?," *Angew. Chemie - Int. Ed.*, vol. 48, no. 1, pp. 60–103, 2009, doi: 10.1002/anie.200802248.

[10] T.C. Mokhena, M.J. John, M.A. Sibeko, V.C. Agbakoba, M.J. Mochane, A. Mtibe, T.H. Mokhothu, T.S. Motsoeneng, M.M. Phiri, M.J. Phiri, P.S. Hlangothi, T.G. Mofokeng, "Nanomaterials: Types, Synthesis and Characterization," pp. 115–141, 2020, doi: 10.1007/978-981-13-9333-4_5.

[11] V. Singh, P. Yadav, and V. Mishra, "Classification on Dimension Sd," pp. 83–97, 2021.

[12] T. Wang, J. Zhuang, J. Lynch, O. Chen, Z. Wang, X. Wang, D. LaMontagne, H. Wu, Z. Wang, Y.C. Cao, "Self-assembled colloidal superparticles from nanorods," *Science (80-.).*, vol. 338, no. 6105, pp. 358–363, 2012, doi: 10.1126/science.1224221.

[13] Raty.John , "Band gap engnerring in bulk and nanosemicoductrs " *Mterrial resrche socity*, pp. 233–238, 2012 Doi10.1557/opl2012.

[14] F. Shuaib, D. Kimbrough, M. Roofe, G. McGwin Jr, and P. Jolly, “Semiconductor Nanocrystals: Structure, Properties, and Band Gap Engineering,” *Bone*, vol. 23, no. 1, pp. 1–7, 2008, doi: 10.1021/ar9001069.Semiconductor.

[15] A. Anwar, M. A. Basith, and S. Choudhury, “From Bulk to Nano: A comparative investigation of Structural, Ferroelectric and Magnetic properties of Sm and Ti co-doped $BiFeO_3$ multiferroics” *Mater. Res. Bull.*, 2018, doi: 10.1016/j.materresbull.2018.11.003.

[16] K. Bian, Z. Wang, and T. Hanrath, “Comparing the Structural Stability of PbS Nanocrystals Assembled in fcc and bcc Superlattice Allotropes,” *American Chemical soceity*.2012. doi.org/10.1021/ja304259y/J. Am. Chem. Soc. 2012, 134, 10787−10790 .

[17] A. Banerjee, D. Bernoulli, H. Zhang, M.-F. Yuen, J. Liu, J. Dong, F. Ding, J. Lu, M.Dao,W.Zhang, Y. Lu, S. Suresh, “Ultralarge elastic deformation of nanoscale diamond”. *National Library of Medicine* 2018 Apr 20;360(6386):300-302. doi: 10.1126/science.aar4165.

[18] Y. Xia, Y. Xiong, B. Lim, S. E. Skrabalak, “Shape-controlled synthesis of metal nanocrystals: Simple chemistry meets complex physics? Angew”. *Chem. Int. Ed. Engl.* 48, 60–103 (2009).

[19] L. G. Wang, and A. Zunger,"Cluster-doping approach for wide-gap semiconductors: the case of p-type ZnO", *Physical review letters*, Vol. 90, no.25, 2003.

[20] L .Chen, J .Yang, S. Klaus, L. J. Lee, R. Woods-Robinson, J. Ma, and I. D. Sharp," p-Type transparent conducting oxide/n-type semiconductor heterojunctions for efficient and stable solar water oxidation", *Journal of the American Chemical Society*, Vol. 137,no.30,PP. 9595-9603,2015.

[21] M. A. Kanjwal, and W. W. F. Leung," Electro spun Nano fibers of p-Type CuO/ntype TZB-Gr Heterojunctions with Enhanced Photocatalytic Activity", *Materials Chemistry and Physics*, Vol. 232,pp. 475-484, 2019

[22] P.Y. Yu and M. Cardona, "Fundamentals of Semiconductors Physics and Materials Properties ",4th edition, Springer-Verlag Berlin Heidelberg, Germany, CH 1, 2010.

[23] Z. Tian, P. M. Kouotou and N. Bahlawane," Synthesis of the Catalytically Active Mn3O4 Spinel and Its Thermal Properties", *J. Phys. Chem. C*, vol. 117, pp. 6218 -6224, 2013.

[24] E.C. Ilinoiu, R. Pode, F. Manea, L.A. Colar, A. Jakab, C. Orha, C. Ratiu, C. Lazau, P. Sfarloaga, "Photocatalytic activity of a nitrogen-doped TiO_2 modified zeolite in the degradation of Reactive Yellow 125 azo dye", *J. Taiwan Inst. Chem. Eng*. 44 (2013) 270–278.

[25] R. Ahmad, Z. Ahmad, A.U. Khan, N.R. Mastoi, M. Aslam, J. Kim, "Photocatalytic systems as an advanced environmental remediation: recent developments, limitations and new avenues for applications", *J. Environ. Chem. Eng*. 4 (2016) 4143–4164.

[26] A.R. Rahmani, M.R. Samarghandi, D. Nematollahi, F. Zamani, "A comprehensive study of electrochemical disinfection of water using direct and indirect oxidation processes", *J. Environ. Chem. Eng.* 7 (2019) 102785.

[27] L. Youssef, S. Roualdès, J. Bassil, M. Zakhour, V. Rouessac, C. Lamy, M. Nakhl, "Effect of plasma power on the semiconducting behavior of low-frequency PECVD TiO2 and nitrogen-doped TiO_2 anodic thin coatings: photo-electrochemical studies in a single compartment cell for hydrogen generation by solar water splitting", *J. Appl. Electrochem*. 49 (2019) 135–150. https://doi.org/10.1007/s10800-018-1265-4.

[28] L. E. Smart and E. A. Moore, "Solid State Chemistry, An Introduction", 3rd ed., CRC Press, Boca Raton, p. 351,2016.

[29] K. Seeger,"Semiconductor Physics An Introduction ", 9th edition, Springer-Verlag Berlin Heidelberg, Germany, CH1, 2004.

[30] Wen-Jian Kuang, Harm Tolner and Qing Li, " Cathodeluminescence diagnostics of MgO, MgO:Si, MgO:Sc, and MgCaO ", *Journal of the SID* 20/1, pp. 63-69,2012.

[31] R.F. Pierret "Advanced semiconductor Fundemantals", 1st ed., vol. VI ,Modular series on solid state devices, CH5,2002.

[32] K. Ravichandran, N. Chidhambaram, S. Gobalakrishnan, "Copper and Graphene activated ZnO nanopowders for enhanced photocatalytic and antibacterial activities", *J. Phys. Chem. Solids* 93 (2016) 82–90.

[33] K. Maeda, "Rhodium-doped barium titanate perovskite as a stable p-type semiconductor photocatalyst for hydrogen evolution under visible light", *ACS Appl. Mater. Interfaces* 6 (2014) 2167–2173

[34] D. Dvoranová, V. Brezová, M. Mazúr, M.A. Malati, "Investigations of metal-doped titanium dioxide photocatalysts", *Appl. Catal. B* 37 (2002) 91–105.

[35] L. Pan, J.-J. Zou, X. Zhang, L. Wang, "Water-mediated promotion of dye sensitization of TiO_2 under visible light", *J. Am. Chem. Soc*. 133 (2011) 10000–10002.

[36] S. Thota, S.R. Tirukkovalluri, S. Bojja, "Effective catalytic performance of manganese and phosphorus co-doped titania nanocatalyst for Orange-II dye degradation under visible light irradiation", *J. Environ. Chem. Eng*. 2 (2014) 1506–1513.

[37] O. Vozniuk, T. Tabanelli, N.T. Id, J.M. Millet, S.A. Id, F. Di Renzo, F. Cavani, “Mixed-Oxide Catalysts with Spinel Structure for the Valorization of Biomass : The Chemical-Loop Reforming of Bioethanol,” pp. 1–16, 2018, doi:

10.3390/catal8080332.

[38] G. Pilania, V. Kocevski, J.A. Valdez, C.R. Kreller, B.P. Uberuaga, “Prediction of structure and cation ordering in an ordered normal-inverse double spinel”, *Commun. Mater.* (2020) 1–11. https://doi.org/10.1038/s43246-020-00082-2.

[39] A. Sutka, G. Mezinskis, M. Zamovskis, D. Jakovlevs, I. Pavlovska, “Monophasic ZnFe2O4 synthesis from a xerogel layer by auto combustion”, *Ceram. Int*. 39 (2013) 8499–8502.

[40] Yudong Li., Zhenyu Yu., Fanli M., “Spinel-Type Materials Used for Gas Sensing :A Review", *Sensors* 2020, 20, 5413.

[41] U. A. Saed, M. Hussein, and A. Nahrain, “Adsorption of Methylene Blue Dye From Aqueous Solution Using Can Papyrus,” J. Babylon Univeristy Eng. Sci., vol. 22, no. 1, pp. 218–229, 2014.

[42] J.L. Gong, B. Wang, G.M. Zeng, C.P. Yang, C.G. Niu, Q.Y. Niu, W.J. Zhou, Y. Liang, “Removal of cationic dyes from aqueous solution using magnetic multi-wall carbon nanotube nanocomposite as adsorbent,” *J. Hazard. Mater.*, vol. 164, no. 2–3, pp. 1517–1522, 2009, doi: 10.1016/j.jhazmat.2008.09.072.

[43] S. Benkhaya, S. M’ rabet, and A. El Harfi, “A review on classifications, recent synthesis and applications of textile dyes,” *Inorg. Chem. Commun.*, vol. 115, no. January, p. 107891, 2020, doi: 10.1016/j.inoche.2020.107891.

[44] F. Lu and D. Astruc, “Nanocatalysts and other nanomaterials for water remediation from organic pollutants,” *Coord. Chem. Rev.*, vol. 408, p. 213180, 2020, doi: 10.1016/j.ccr.2020.213180.

[45] S. Jeyaram, “Intermolecular charge transfer in donor–acceptor substituted triarylmethane dye for NLO and optical limiting applications,” *J. Mater. Sci. Mater. Electron.*, vol. 32, no. 7, pp. 9368–9376, 2021, doi: 10.1007/s10854-021-05600-7.

[46] S.C.W. Sakti, R.N. Laily, S. Aliyah, N. Indrasari, M.Z. Fahmi, H.V. Lee, Y. Akemoto, S. Tanaka, “Re-collectable and recyclable epichlorohydrin-crosslinked humic acid with spinel cobalt ferrite core for simple magnetic removal of cationic triarylmethane dyes in polluted water,” *J. Environ. Chem. Eng.*, vol. 8, no. 4, p. 104004, 2020, doi: 10.1016/j.jece.2020.104004.

[47] C. Sessa, R. Weiss, R. Niessner, N. P. Ivleva, and H. Stege, “Towards a Surface Enhanced Raman Scattering (SERS) spectra database for synthetic organic colourants in cultural heritage. The effect of using different metal substrates on the spectra,” *Microchem. J.*, vol. 138, pp. 209–225, 2018, doi: 10.1016/j.microc.2018.01.009.

[48] S. Dutta, B. Gupta, S. K. Srivastava, and A. K. Gupta, “Recent advances on the removal of dyes from wastewater using various adsorbents: A critical review,” *Mater. Adv.*, vol. 2, no. 14, pp. 4497–4531, 2021, doi: 10.1039/d1ma00354b.

[49] S.B. Somvanshi, P.B. Kharat, M. V. Khedkar, K.M. Jadhav, “Hydrophobic to hydrophilic surface transformation of nano-scale zinc ferrite via oleic acid coating: Magnetic hyperthermia study towards biomedical applications,”, *Ceram. Int*. 46 (2020) 7642–7653.doi.org/10.1016/j.ceramint.2019.11.265.

[50] K.K. Kefeni, T.A.M. Msagati, T.T. Nkambule, B.B. Mamba, “Spinel ferrite nanoparticles and nanocomposites for biomedical applications and their toxicity,” *Mater. Sci. Eng.* C. 107 (2020) .doi.org/10.1016/j.msec.2019.110314.

[51] S.H. Khoreem, A. H. AL-Hammadi, “ Influence of Zn^{2+} Ions Doping on the Antibacterial Activity of Barium- Nickel Ferrite Nanoparticles110314. doi.org/10.1016/j.msec.2019.110314., *Al-Razi Univ J Med Sci* 2022; 6 (2):11-21

[52] M. M. Faghih and M. K. Sharp, "Modeling and prediction of flow-induced hemolysis: a review", Springer Berlin Heidelberg,vol. 18, no. 4. 2019. doi: 10.1007/s10237-019-01137-1.

[53] S. Naz, A. Gul, and M. Zia, "Toxicity of copper oxide nanoparticles: a review study," *IET nanobiotechnology*, vol. 14, no. 1, pp. 1-13, 2020.

[54] N. Singh, S. K. Sahoo, and R. Kumar, “Hemolysis tendency of anticancer nanoparticles changes with type of blood group antigen: An insight into blood nanoparticle interactions,” *Mater. Sci. Eng. C*, vol. 109, no. July 2019, p. 110645, 2020, doi: 10.1016/j.msec.2020.110645.

[55] Q. Ran Ran, Qian Y. Xiang, Y. Liu, L. Xiang, F.Li, X.Deng, Y.Xiao, “Eryptosis Indices as a Novel Predictive Parameter for Biocompatibility of Fe_3O_4 Magnetic Nanoparticles on Erythrocytes,” *Nat. Publ. Gr*., no. November, pp. 1–15, 2015, doi: 10.1038/srep16209.

[56] A. A. Ali, D. Abd-alkareem, I. G. Zainal, and S. J. Ali, “In vitro biochemical evaluation the effect of (Cobalt and Nickel-Zinc) ferrite Nanoparticles on beta -thalassemia major erythrocytes In vitro biochemical evaluation the effect of (Cobalt and Nickel-Zinc) ferrite Nanoparticles on beta -thalassemia major erythrocytes,” Eur Asian Journal of Bio Sciences November, 2020.

[57] N. L. Martínez-rodríguez, S. Tavárez, and Z. I. González-sánchez, “Toxicology in Vitro In vitro toxicity assessment of zinc and nickel ferrite nanoparticles in human erythrocytes and peripheral blood mononuclear cell,” *Toxicol. Vitr.*, vol. 57, no. October 2018, pp. 54–61, 2019, doi: 10.1016/j.tiv.2019.02.011.

[58] Shang, L., Nienhaus, K., Nienhaus, G.U., “Engineered nanoparticles interacting with cells: size matters”. *J. Nanobiotechnol* 12, 2014. 1–11. https://doi.org/10.1186/1477-3155- 12-5.

[59] Feng, Q., Liu, Y., Huang, J., Chen, K., Huang, J., Xiao, K., Uptake, "distribution, clearance, and toxicity of iron oxide nanoparticles with different sizes and coatings, ". *Sci. Rep*. 8, 2018.1–13. https://doi.org/10.1038/s41598-018-19628-z.

[60] Wang, J., Zhang, L., Peng, F., Shi, X., Leong, D.T., "Targeting endothelial cell junctions with negatively charged gold nanoparticles, ". *Chem. Mater*. 2018.30, 3759–3767. https://doi.org/10.1021/acs.chemmater.8b00840.

[61] S. B. Patil, H. S. B. Naik, G. Nagaraju, R. Viswanath, S. K. Rashmi, and M. Vijay, "Graphical abstract," *Mater. Chem. Phys.*, 2018, doi: 10.1016/j.matchemphys.2018.03.038.

[62] M. M. Naik, H. S. B. Naik, G. Nagaraju, M. Vinuth, H. R. Naika, and K. Vinu, "Green synthesis of zinc ferrite nanoparticles in Limonia acidissima juice : Characterization and their application as photocatalytic and antibacterial activities," *Microchem. J.*, vol. 146, no. February, pp. 1227–1235, 2019, doi: 10.1016/j.microc.2019.02.059.

[63] Q. Yu and Y. Su, "RSC Advances Synthesis and characterization of low density porous nickel zinc ferrites," pp. 13173–13181, 2019, doi: 10.1039/c9ra01076a.

[64] M. Bagher and P. Salarizadeh, "ScienceDirect Binary nickel ferrite oxide ($NiFe_2O_4$) nanoparticles coated on reduced graphene oxide as stable and high-performance asymmetric supercapacitor electrode material," *Int. J. Hydrogen Energy*, vol. 45, no. 51, pp. 27482–27491, 2020, doi: 10.1016/j.ijhydene.2020.07.063.

[65] A. Ali and M. Iqbal, "Synthesis and characterization of $NiFe_2O_4$ ferrite: Sol–gel and hydrothermal synthesis routes effect on structural, magnetic and dielectric properties," *Mater. Chem. Phys.*, p. 123888, 2020, doi: 10.1016/j.matchemphys.2020.123888.

[66] S. O. Aisida, A. Ali, O. E. Oyewande, I. Ahmad, A. Ul-hamid, and T. Zhao, "Biogenic synthesis enhanced structural , morphological , magnetic and optical properties of zinc ferrite nanoparticles for moderate hyperthermia applications," 2021.

[67] W. A. Khoso, N. Haleem, M. A. Baig, and Y. Jamal, "Synthesis , characterization and heavy metal removal efficiency of nickel ferrite nanoparticles (NFN ' s)," *Sci. Rep.*, pp. 1–10, 2021, doi: 10.1038/s41598-021-83363-1.

[68] A. Rabbani, R. Haghniaz, T. Khan, R. Khan, and A. Khalid, "Development of bactericidal spinel ferrite nanoparticles with e ff ective biocompatibility for," pp. 1773–1782, 2021, doi: 10.1039/d0ra08417d.

[69] V. Y. Buz, I. I. Shamrai, M. Y. Ryabova, G. V Kireeva, and A. I. Goryachko,

"Properties of Nickel Zinc Ferrite Nanopowders Prepared by Different Methods Properties of Nickel Zinc Ferrite Nanopowders Prepared by Different Methods," no. April, 2021, doi: 10.1134/S0020168521010027.

[70] S. Jassim, A. Abbas, , M. AL-Shakban, and L. M. Ahmed, "Chemical Vapour Deposition of CdS Thin Films at Low Temperatures from Cadmium Ethyl Xanthate", *Egyptian Journal of Chemistry*, 64(5), 2533 - 2538, (2021). DOI: 10.21608/EJCHEM.2021.60695.3451.

[71] L.M.Ahmed, I. Ivanova, F.H.Hussein, and D.W. Bahnemann, "Role of platinum deposited on TiO_2 in photocatalytic methanol oxidation and dehydrogenation reactions", *International Journal of Photoenergy*, 1-10 (2014). doi.org/10.1155/2014/503516.

[72] Jawad, T.M., and Ahmed, L. M., "Direct Ultrasonic Synthesis of WO_3/TiO_2 Nanocomposites and Applying them in the Photodecolorization ofEosin Yellow Dye", *Periódico Tchê Química*, 17(34), 621-633, (2020).

[73] Hayawi, M. K., Kareem, M. M., and Ahmed, L. M., "Synthesis of Spinel Mn_3O_4 and Spinel Mn_3O_4/ZrO_2 Nanocomposites and Using Them in Photo-Catalytic Decolorization of Fe(II)-(4,5- Diazafluoren-9-One 11) Complex". *Periódico Tchê Química*, 17(34), 689- 699, (2020).

[74] Hussain, Z. A., Fakhri, F. H., Alesary, H. F., and Ahmed, L. M., "ZnO Based Material as Photocatalyst for Treating the Textile Anthraquinone Derivative Dye (Dispersive Blue 26 Dye): Removal and Photocatalytic Treatment", *J. Phys. Conf. Ser*., 1664(1),1-15 (2020), doi: 10.1088/1742-6596/1664/1/012064.

[75] Hussein, Z. A., Abbas, S. K., and Ahmed, L. M., "UV-A activated ZrO_2 via photodecolorization of methyl green dye", *IOP Conf. Ser. Mater. Sci. Eng*., vol. 454(1), 012132, (2018), doi: 10.1088/1757-899X/454/1/012132.

[76] S. Ahmed, "Photo electrochemical study of ferrioxalate actinometry at a glassy carbon electrode," *J. Photochem. Photobiol. A Chem*., vol. 161, no. 2–3, pp. 151–154, 2004.

[77] A. W. Adamson, A. Vogler, H. Kunkely, and R. Wachter, "Photocalorimetry. Enthalpies of photolysis of trans-azobenzene, ferrioxalate and cobaltioxalate ions, chromium hexacarbonyl, and dirhenium decarbonyl," *J. Am. Chem. Soc*., vol. 100, no. 4, pp. 1298–1300, 1978.

[78] A. Raidou, F. Benmalek, T. Sall, M. Aggour, A. Qachaou, L. Laanab, M. Fahoume., "Characterization of ZnO thin films grown by SILAR method," *Open Access Libr. J*., vol. 1, no. 3, pp. 1–9, 2014.

[79] S. I. Zuafuani and L. M. Ahmed, "Photocatalytic decolourization of direct orange Dye by zinc oxide under UV irradiation," *Int. J. Chem. Sci*, vol. 13, no. 1, pp. 187–196, 2015.

[80] P. Atkins and J. Paula, Atkins' Physical Chemistry, 8th ed., W. H. Freeman and

Company, New York, CH3, p 96, 2006.

[81] T.M. Alfareed, Y. Slimani, M.A. Almessiere, M. Nawaz, F.A. Khan, A. Baykal, E.A. Al-Suhaimi, "Biocompatibility and colorectal anti-cancer activity study of nanosized BaTiO3 coated spinel ferrites," *Sci. Rep.*, vol. 12, no. 1, pp. 1–18, 2022, doi: 10.1038/s41598-022-18306-5.

[82] Parveen, S., Premkumar, T., Poornima, S., Govindarajan, S., Catalytic activity of nanocrystalline ZnM_2O_4 (M= Fe,Co) prepared via simple and facile synthesis of thermal decomposition of mixed metal complexes of Schiff bases generated from a-ketobutyric acid and diaminoguanidine, *Journal of Saudi Chemical Society*, 23, 691–701(2019).

[83] Naseri, M. G., Saion, E. B, Ahangar, H. A., Shaari,A. H., and Hashim, M., Simple Synthesis and Characterization of Cobalt Ferrite Nanoparticles by a Thermal Treatment Method, Journal of Nanomaterials, (2010), Article ID 907686, 8 pages doi:10.1155/2010/907686.

[84] Habibi, M. H., and Fakhri, F., Low temperature preparation, characterization, magnetic measurements, thermal, optical, morphological and photo-catalytic properties of nano-size single phase nickel ferrite $NiFe_2O_4$, *J. Mater. Sci. Mater. Electron.*, 28(18),13455–13463, (2017). doi: 10.1007/s10854-017-7184-z.

[85] Pascuta, P., Vladescu, A., Borodi, G., Culea, E., Tetean, R., Structural and magnetic properties of zinc ferrite incorporated in amorphous matrix, Ceramics International, 37, 3343–3349,(2011). doi:10.1016/j.ceramint.2011.05.134.

[86] Husain, S., Yusup, M, Haryanti, N H., Suryajaya, Saukani, M., Rodiansono, Arjo, S., Riyanto, A., Characteristics of zinc ferrite nanoparticles ($ZnFe_2O_4$) *from natural iron ore, IOP Conf. Series: Earth and Environmental Science*, 758, 012001, 1-6,(2021).

[87] Rachna, N. B. Singh, and A. Agarwal, "Preparation, Characterization, Properties and Applications of nano Zinc Ferrite", *Mater. Today Proc.*, 5(3), 9148–9155, (2018), doi: 10.1016/j.matpr.2017.10.035.

[88] S. Qamar, M. N. Akhtar, K. M. Batoo, and E. H. Raslan, "Structural and magnetic features of Ce doped Co-Cu-Zn spinel nanoferrites prepared using sol gel self-ignition method," *Ceram. Int.*, vol. 46, no. 10, pp. 14481–14487, 2020, doi: 10.1016/j.ceramint.2020.02.246.

[89] A. Galal, O. Sadek, M. Soliman, S. Ebrahim, and M. Anas, "Synthesis of nanosized nickel zinc ferrite using electric arc furnace dust and ferrous pickle liquor," *Sci. Rep.*, vol. 11, no. 1, pp. 1–11, 2021, doi: 10.1038/s41598-021-99697-9.

[90] Ezzayani, K., Khelifa, A., Saint-Aman. E., Loiseau, F. and Nasri, H., Complex of hexamethylenetetramine with Magnesium Tetraphenylporphyrin: Synthesis, Structure, Spectroscopic Characterizations and Electrochemical Properties, Journal of Molecular Structure, 1-12, (2017), doi: 10.1016/j.molstruc.2017.02.054.

[91] Naseri, M. G., Saion, E. B., Ahangar, H. A., Hashim, M., and Shaari, A. H., Simple preparation and characterization of nickel ferrite nanocrystals by a thermal treatment method, *Powder Technol.*, 212(1), 80–88, (2011), doi: 10.1016/j.powtec.2011.04.033.

[92] Aliahmad, M., Noori, M., Kargan, N. H., and Sargazi, M., Synthesis of nickel ferrite nanoparticles by co-precipitation chemical method, *Int. J. Phys. Sci*., 8(18), 854–858, (2013), doi: 10.5897/ijps11.517.

[93] Ahmad, N., Alam, M., Ansari, A. A., Alrayes, B. F., Ahmed, M. and Alotaibi, M. A., Nickel Ferrite Nanomaterials: Synthesis, Characterization and Properties, *Nanoscience and Nanotechnology Letters* , 9, 1688–1695, (2017).

[94] Rachna, N. B. Singh, and A. Agarwal, Preparation, Characterization, Properties and Applications of nano Zinc Ferrite, Mater. Today Proc., 5(3), 9148–9155, (2018), doi: 10.1016/j.matpr.2017.10.035.

[95] Sambathkumar,C., Arasi, S. E., Natarajan, B., Arivarasan, A., Devendran, P., Examination of Structral Morphological and Magnetic Behaviour of ZnFe2O4 Nanoparticle Synthesised by Co-Pricipitation Method, International Journal of Engineering and Advanced Technology, 9, 1085-1088(2010).

[96] A.C. Prabakar, G. Killivalavan, D. Sivakumar, K. Chandra Babu Naidu, B. Sathyaseelan, K. Senthilnathan, I. Baskaran, E. Manikandan, M. Balaraju, “Exploring structural, morphological, and magnetic properties of zinc nickel ferrites systems nanocomposites,” *Biointerface Res. Appl. Chem.*, vol. 11, no. 1, pp. 7785–7793, 2021, doi: 10.33263/BRIAC111.77857793.

[97] M. Rahimi, P. Kameli, M. Ranjbar, H. Hajihashemi, and H. Salamati, “The effect of zinc doping on the structural and magnetic properties of Ni1-xZnxFe2O4,” *J. Mater. Sci.*, vol. 48, no. 7, pp. 2969–2976, 2013, doi: 10.1007/s10853-012-7074-y.

[98] Ghosh, D. C. and Biswas, R., "Theoretical Calculation of Absolute Radii of Atoms and Ions. Part 2. The Ionic Radii", *Int. J. Mol. Sci.*, 4, 379-407, (2003).

[99] Naseri, M. G., Saion, E. B., and Kamali, A., "An Overview on Nanocrystalline $ZnFe_2O_4$, $MnFe_2O_4$, and $CoFe_2O_4$ Synthesized by a Thermal Treatment Method" , *ISRN Nanotechnol.*, 1–11, (2012), doi: 10.5402/2012/604241.

[100] L. Andjelković, M. Šuljagić, M. Lakić, D. Jeremić, P. Vulić, and A. S. Nikolić, “A study of the structural and morphological properties of Ni–ferrite, Zn–ferrite and Ni–Zn–ferrites functionalized with starch,” *Ceram. Int.*, vol. 44, no. 12, pp. 14163–14168, 2018, doi: 10.1016/j.ceramint.2018.05.018.

[101] Karaagac,O., Atmaca,S., and Kockar, H., A Facile Method to Synthesize Nickel Ferrite Nanoparticles: Parameter Effect, *J. Supercond. Nov. Magn.*, 30(8), 2359–2369, (2017), doi: 10.1007/s10948-016-3796-4.

[102] Talebi, R., Preparation of nickel ferrite nanoparticles via a new route and study of their photocatalytic properties, *J. Mater. Sci. Mater. Electron*., 28(5), 4058–

4063, (2017), doi: 10.1007/s10854-016-6020-1.

[103] Salvador, M., Gutiérrez, G., Noriega, S., Moyano, A., Blanco-López, M. and Matos, M., Microemulsion Synthesis of Superparamagnetic Nanoparticles for Bioapplications , *Int. J. Mol. Sci.*, 22(427), 1-17,(2021).

[104] Ali, S, Ali, M, and Ahmed, L.M Hybrid Phosphotungstic acid-Dopamine (PTA-DA) Likeflower Nanostructure Synthesis as a Furosemide Drug Delivery System and Kinetic Study of Drug Releasing. Egyptian Journal of Chemistry, 64(10), 5547-5553 (2021).DOI. 10.21608/EJCHEM.2021.75210.3692.

[105] Obaid, A. J. and Ahmed, L. M., One-Step Hydrothermal Synthesis of α- MoO3 Nano-belts with Ultrasonic Assist for incorporating TiO2 as a Nanocomposite, Egypt. J. Chem., 64(10), 5725 -5734 (2021). DOI. 10.21608/EJCHEM.2021.72582.3615

[106] I.H. Hasan, M.N. Hamidon, A. Ismail, I. Ismail, N.A. Mohd Azhari, M.A. Mohd Kusaimi, S. Azhari, "Nickel zinc ferrite thick film with linseed oil as organic vehicle for microwave device applications," *Mater. Chem. Phys.*, vol. 236, no. June, p. 121790, 2019, doi: 10.1016/j.matchemphys.2019.121790.

[107] Koli,P. B., Kapadnis,K. H. and Deshpande,U. G., "Nanocrystalline-modified nickel ferrite films: an effective sensor for industrial and environmental gas pollutant detection", *J. Nanostructure Chem.*, 9(2), 95–110, (2019), doi: 10.1007/s 40097-019-0300-2.

[108] Alijani,H. Q., Iravani,S., Pourseyedi,S., Torkzadeh-Mahani,M., Barani,M. and Khatami, M. "Biosynthesis of spinel nickel ferrite nanowhiskers and their biomedical applications", *Sci. Rep.*, 11(1), 1–7, (2021), doi: 10.1038/s41598-021-96918-z.

[109] Kumar,G. S. Y., Naik, H. S. B., Roy, A. S., Harish, K. N., and Viswanath, R., "Synthesis, optical and electrical properties of ZnFe2O4 nanocomposites", Nanomater. Nanotechnol., 2(1), 1–6, (2012), doi: 10.5772/56169.

[110] Manikandan, A., Vijaya, J. J., Sundararajan, M., Meganathan, C., Kennedy, L. J., and Bououdina, M., Optical and magnetic properties of Mg-doped ZnFe2O4 nanoparticles prepared by rapid microwave combustion method, Superlattices Microstruct., 64, 118–131, (2013), doi: 10.1016/j.spmi.2013.09.021.

[111] I. G. Zainal, A. M. Al-Shammari, and W. Kachi, "Characterization of the modified nickel-zinc ferrite nanoparticles coated with APTES by salinization reaction," *AIP Conf. Proc.*, vol. 1968, 2018, doi: 10.1063/1.5039195.

[112] F. H. Fakhri and L. M. Ahmed, "Incorporation Cds with Zns as Composite and Using in Photo-Decolorization of Congo Red Dye," Indones. J. Chem., vol. 19, no. 4, pp. 936–943, 2019.

[113] S. T. Fardood, R. Forootan, F. Moradnia, Z. Afshari, and A. Ramazani, "Green synthesis, characterization, and photocatalytic activity of cobalt chromite spinel nanoparticles," Mater. Res. Express, vol. 7, no. 1, p. 15086, 2020.

[114] Sharifi,S., Yazdani,A., and Rahimi,K., “Incremental substitution of Ni with Mn in $NiFe_2O_4$ to largely enhance its supercapacitance properties,” *Sci. Rep.*, 10(1), 1–15, (2020), doi: 10.1038/s41598-020-67802-z.

[115] Meinert, M. and Reiss, G.,“Electronic structure and optical band gap determination of $NiFe_2O_4$”, *J. Phys. Condens. Matter*, 26(11), 2–5, 2014, doi: 10.1088/0953-8984/26/11/115503.

[116] Rachna, N. B. Singh, and A. Agarwal, “Preparation, Characterization, Properties and Applications of nano Zinc Ferrite,” Mater. Today Proc., 5(3), 9148–9155, (2018), doi: 10.1016/j.matpr.2017.10.035.

[117] G. P. Joshi, N. S. Saxena, R. Mangal, A. Mishra, and T. P. Sharma, “Band gap determination of Ni-Zn ferrites,” Bull. Mater. Sci., vol. 26, no. 4, pp. 387–389, 2003, doi: 10.1007/BF02711181.

[118] G. A. Bain and J. F. Berry, “Diamagnetic Corrections and Pascal ’ s Constants,” vol. 85, no. 4, pp. 1–5, 2008.

[119] A. E. L. Maazouzi, R. Masrour, and A. Jabar, “Magnetic Properties of Inverse Spinel : (Fe 3 +) A (Fe 3 + Fe 2 +) B O 2,” vol. 2, 2020.

[120] H. Chun, W. Yizhong, and T. Hongxiao, "Destruction of phenol aqueous solution by photocatalysis or direct photolysis", Journal of Chemosphere, vol. 41, pp. 1205– 1209, 2000.

[121] A. Ameer, A. Zaid, L. M. Ahmed, and R. K. Mohammad, “Synthesis of Inverse Spinel Nickel Ferrite Like- Broccoli Nanoparticle and Thermodynamic Study of Photo-decolorization of Alkali Blue 4B dye,” vol. 12, no. 3, pp. 697–710, 2022, doi: 10.22052/JNS.2022.03.022.

[122] Z. A . Hussein, S. K. Abbas, and L. M. Ahmed," UV-A activated ZrO2 via photodecolorization of methyl green dye", In IOP Conference Series: Materials Science and Engineering ,Vol. 454, No. 1, pp.1-11, 2018.

[123]. Findik S. Decolorization of Direct Black 22 by Photo Fenton like Method Using UV Light and Zeolite Modified Zinc Ferrite: Kinetics and Thermodynamics. Acta Chimica Slovenica. 2022;69(3):552-563.

[124]. Prabha I, Lathasree S. Photocatalytic Degradation of Reactive Red 198 Dye Using Zinc Oxide and Titanium Dioxide Nanocatalysts. Asian J Chem. 2014;26(9):2797- 2801.

[125] E. Marchenko, G. Baigonakova, K. Dubovikov, A. Vorozhtsov, O. Kokorev, and Y. Yasenchuk, “In Vitro Bio-Testing Comparative Analysis of NiTi Porous Alloys Modified by Heat Treatment,” 2022.

الخلاصة

يتضمن العمل اربعة أجزاء رئيسية. **الجزء الأول** يوضح تحضير سبنلين: $NiFe_2O_4$ و $ZnFe_2O_4$ بوجود خافض الشد السطحي الغير ايوني (hexamine) كعامل تغطية باستخدام طريقة الترسيب المشترك. دعمت هذه الطريقة باستخدام طريقة الاذابة الحرارية باستخدام الايثانول عند درجة حرارة ١٨٠ درجة مئوية ولمـــدة ٩٠ دقيقة. حضــر المتراكــب $Zn\text{-}NiFe_2O_4$ بتعشيق السبنل الاول والسبنل الثاني باستخدام تقنية الموجات فوق الصوتية كطريقة بسيطة وصديقة للبيئة.

الجزء الثاني تضمن هذا الجزء قياس خواص جميع العوامل المساعدة الضوئية المحضرة باستخدام تقنية FTIR, XRD, (SEM, EDX) حيث اوضحت قياسات FTIR مواقع ثماني السطوح ورباعي السطوح للفلزات والحديد للنماذج المحضرة $ZnFe_2O_4$، و $NiFe_2O_4$، و المتراكب $Zn\text{-}NiFe_2O_4$ ووجد سبنل اعتيادي، وسبنل عكسي، وسبنل عكسي على التوالي. بناءً على تحليل XRD وجد بان مركبات الإسبنيل $NiFe_2O_4$ والسبنل $ZnFe_2O_4$ والمتراكب $Zn\text{-}NiFe_2O_4$ تمتلك أحجام نانوية ذات قياس ٢٠.١٣ نانومتر و ١٦.٩٨ نانومتر و ٢٨.٨٢ نانومتر على التوالي.

أعطى تحليل SEM فكرة عن شكل سطح المحفزات الضوئية المدروسة. وظهر ان شكل الإسبنيل $NiFe_2O_4$ يشبه البروكلي كذلك المتراكب $Zn\text{-}NiFe_2O_4$ اما السبنيل $ZnFe_2O_4$ فانه يشبه القرنبيط . تم العثور على أحجام الجسيمات التي تم قياسها والتي تم تحديدها من تحليل SEM للسبنل الاول ٣٠.٦٧ نانومتر والسبنل الثاني ٢٧.٧٨ نانومتر والمتراكب ٤٠.١٩ نانومتر وبذلك تعتبر جميع العينات المدروسة هي بلورات نانوية. من خلال اطياف EDX ، ظهر جميع العناصر Ni و Zn و Fe و O التي تتكون منها المحفزات الضوئية موجودة ولا يوجد شوائب معها. تم استخدام معادلة Tauc لإيجاد كل أنواع فجوات النطاق للمحفزات الضوئية المدروسة. ظهرت فجوات النطاق غير مباشرة لجميع العينات، وكانت قيم فجوات الطاقة eV ٢.٠٥ وeV ٢.١٥ و مدى طاقة الفجوة بمعدل eV (١.٥٦- ١.٩) .للسبنل $NiFe_2O_4$ والسبنل $ZnFe_2O_4$ والمتراكب $Zn\text{-}NiFe_2O_4$ على التوالي.

الجزء الثالث، ركز على قدرة العوامل المساعدة الضوئية المحضرة على عملية الازالة اللونية لصبغة الازرق القلوي من خلال الاهتمام بدراسة تأثير العوامل المختلفة على ازالة الصبغة بوجود عينات العوامل الضوئية المساعدة. تضمنت هذه العوامل وزن العامل المساعد، ودرجة الحرارة، والدالة الحامضية الابتدائية. اظهرت النتائج ان اعلى ازالة لونية للصبغة عند 0.025 g/100mL, 0.025 g/100mL و 0.015 g/100mL 0.015 g/100mLلكل من العوامل المساعدة الضوئية المحضرة $NiFe_2O_4$ و $ZnFe_2O_4$ والمتراكب $Zn\text{-}NiFe_2O_4$ على التوالي.

طبقت مدى من درجات الحرارة (١٥و٢٠و٢٥و٣٥) درجة مئوية حيث اثر ارتفاع درجة الحرارة على كفاءة الازالة اللونية للصبغة للسبنل الاول و السبنل الثاني والمتراكب ،هذا يثبت ان التفاعل ماص للحرارة وغير تلقائي. وجد ان قيمة طاقة التنشيط للسبنل $NiFe_2O_4$ اقل مــن طاقة التنشيط للمتراكب $Zn\text{-}NiFe_2O_4$ والسبنل $ZnFe_2O_4$ والتــي كانت تساوي / (١٠.٧٨٧و ٢٣.٦٩٦ و ٤٧.٦٨٩) $\mathbf{kJ\ mol^{-1}}$ على التوالي. كما وجد ان افضل داله حامضية لإزالة الصبغة لجميع العوامل المساعدة الضوئية عند ٧.

الجزء الرابع، تضمن تطبيق العوامل المساعدة الضوئية في اختبار انحلال الدم وذلك من خلال اخذ ٦٠ عينة من اشخاص اصحاء وغير مدخنين باستخدام تراكيز مختلفة من سبنل $NiFe_2O_4$ و سبنل $ZnFe_2O_4$ و المتراكب $Zn\text{-}NiFe_2O_4$ ووجدت تساوي الى g/mL ٠.٠٢٥ وg/mL ٠.٠٢٥و g/mL ٠.٠١٥على التوالي.

جامعة كربلاء
كلية العلوم
قسم الكيمياء

التخليق وفعالية التحطيم الضوئي لمتراكب نانوي نيكل- زنك فريت واختباره في انحلال الدم

رسالة مقدمة الى مجلس كلية العلوم / جامعة كربلاء وهي جزء من متطلبات نيل درجة الماجستير في علوم الكيمياء

من قبل

علي امير عبدزيد الخفاجي

بإشراف

أ. د لمى مجيد احمد

أ.م. د رجاء حضر محمد

٢٠٢٣ م

١٤٤٤ هـ